The Amsterdam Modeling Suite

Baerends, Evert Jan; Aguirre, Nestor F.; Austin, Nick D.; Autschbach, Jochen; Bickelhaupt, F. Matthias; Bulo, Rosa; Cappelli, Chiara; van Duin, Adri C.T.; Thijssen, Jos M.; More Authors

DOI
10.1063/5.0258496

Publication date
2025

Document Version
Final published version

Published in
Journal of Chemical Physics

Citation (APA)
Baerends, E. J., Aguirre, N. F., Austin, N. D., Autschbach, J., Bickelhaupt, F. M., Bulo, R., Cappelli, C., van Duin, A. C. T., Thijssen, J. M., & More Authors (2025). The Amsterdam Modeling Suite. *Journal of Chemical Physics*, *162*(16), Article 162501. https://doi.org/10.1063/5.0258496

The Journal of Chemical Physics

RESEARCH ARTICLE | APRIL 22 2025

The Amsterdam Modeling Suite

Evert Jan Baerends ✉ ; Nestor F. Aguirre ; Nick D. Austin; Jochen Autschbach ;
F. Matthias Bickelhaupt ; Rosa Bulo; Chiara Cappelli ; Adri C. T. van Duin ; Franco Egidi ;
Célia Fonseca Guerra ; Arno Förster ; Mirko Franchini; Theodorus P. M. Goumans ; Thomas Heine ;
Matti Hellström ; Christoph R. Jacob ; Lasse Jensen ; Mykhaylo Krykunov; Erik van Lenthe;
Artur Michalak ; Mariusz M. Mitoraj; Johannes Neugebauer ; Valentin Paul Nicu ; Pier Philipsen ;
Harry Ramanantoanina ; Robert Rüger ; Georg Schreckenbach ; Mauro Stener ; Marcel Swart ;
Jos M. Thijssen ; Tomáš Trnka ; Lucas Visscher ; Alexei Yakovlev ; Stan van Gisbergen ✉

J. Chem. Phys. 162, 162501 (2025)
https://doi.org/10.1063/5.0258496

The Journal of Chemical Physics SOFTWARE pubs.aip.org/aip/jcp

The Amsterdam Modeling Suite

Cite as: J. Chem. Phys. 162, 162501 (2025); doi: 10.1063/5.0258496
Submitted: 16 January 2025 • Accepted: 28 March 2025 •
Published Online: 22 April 2025

Evert Jan Baerends,[1,a)] Nestor F. Aguirre,[2] Nick D. Austin,[2] Jochen Autschbach,[3] F. Matthias Bickelhaupt,[1,4,5] Rosa Bulo,[2] Chiara Cappelli,[6,7] Adri C. T. van Duin,[8] Franco Egidi,[2] Célia Fonseca Guerra,[1] Arno Förster,[1] Mirko Franchini,[2] Theodorus P. M. Goumans,[2] Thomas Heine,[9] Matti Hellström,[2] Christoph R. Jacob,[10] Lasse Jensen,[11] Mykhaylo Krykunov,[12] Erik van Lenthe,[2] Artur Michalak,[13] Mariusz M. Mitoraj,[13] Johannes Neugebauer,[14] Valentin Paul Nicu,[15] Pier Philipsen,[2] Harry Ramanantoanina,[16] Robert Rüger,[2] Georg Schreckenbach,[17] Mauro Stener,[18] Marcel Swart,[19,20] Jos M. Thijssen,[21] Tomáš Trnka,[2,22] Lucas Visscher,[1] Alexei Yakovlev,[2] and Stan van Gisbergen[2,a)]

AFFILIATIONS

[1]Vrije Universiteit Amsterdam, De Boelelaan 1105, 1081 HV Amsterdam, The Netherlands
[2]Software for Chemistry & Materials BV, De Boelelaan 1109, 1081HV Amsterdam, The Netherlands
[3]Department of Chemistry, University at Buffalo State University of New York, Buffalo, New York 14260-3000, USA
[4]Institute for Molecules and Materials, Radboud University Nijmegen, Heyendaalseweg 135, 6525 AJ Nijmegen, The Netherlands
[5]Department of Chemical Sciences, University of Johannesburg, Auckland Park, Johannesburg 2006, South Africa
[6]Scuola Normale Superiore, Piazza dei Cavalieri 7, 56126 Pisa, Italy
[7]IMT School for Advanced Studies Lucca, Piazza San Francesco 19, I-55100 Lucca, Italy
[8]Department of Mechanical Engineering, The Pennsylvania State University, University Park, Pennsylvania 16802, USA
[9]Faculty of Chemistry and Food Chemistry, TU Dresden, Bergstraße 66c, 01069 Dresden, Germany
[10]Institute of Physical and Theoretical Chemistry, Technische Universität Braunschweig, Gaußstraße 17, 38106 Braunschweig, Germany
[11]Department of Chemistry, The Pennsylvania State University, 104 Benkovic Building, University Park, Pennsylvania 16802, USA
[12]Insilico Medicine AI Limited, Level 6, Unit 08, Block A, IRENA HQ Building, Masdar City, P.O. Box 145748, Abu Dhabi, United Arab Emirates
[13]Jagiellonian University, Faculty of Chemistry, Gronostajowa 2, 30-387 Kraków, Poland
[14]Universität Münster, Organisch-Chemisches Institut and Center for Multiscale Theory and Computation, Corrensstraße 36, 48149 Münster, Germany
[15]ProVitam Foundation, Caisului Street 16, Cluj-Napoca, Romania
[16]Department Chemie, Johannes Gutenberg-Universität, Fritz-Strassmann Weg 2, 55128 Mainz, Germany
[17]Department of Chemistry, University of Manitoba, Winnipeg, Manitoba R3T 2N2, Canada
[18]Dipartimento di Scienze Chimiche e Farmaceutiche, Università degli studi di Trieste, Via Giorgieri 1, 34127 Trieste, Italy
[19]ICREA, Pg. Lluís Companys 23, 08010 Barcelona, Spain
[20]IQCC and Department Química, Universitat de Girona, Campus Montilivi, 17003 Girona, Spain
[21]Kavli Institute of Nanoscience, Delft University of Technology, 2628 CJ Delft, The Netherlands
[22]National Centre for Biomolecular Research, Faculty of Science, Masaryk University, Kamenice 5, 625 00 Brno, Czech Republic

[a)]**Authors to whom correspondence should be addressed:** e.j.baerends@vu.nl and vangisbergen@scm.com

ABSTRACT

In this paper, we present the Amsterdam Modeling Suite (AMS), a comprehensive software platform designed to support advanced molecular and materials simulations across a wide range of chemical and physical systems. AMS integrates cutting-edge quantum chemical methods, including Density Functional Theory (DFT) and time-dependent DFT, with molecular mechanics, fluid thermodynamics, machine learning techniques, and more, to enable multi-scale modeling of complex chemical systems. Its design philosophy allows for seamless coupling between components, facilitating simulations that range from small molecules to complex biomolecular and solid-state systems, making it a versatile tool for tackling interdisciplinary challenges, both in industry and in academia. The suite also emphasizes user accessibility, with an intuitive graphical interface, extensive scripting capabilities, and compatibility with high-performance computing environments.

 https://doi.org/10.1063/5.0258496

I. INTRODUCTION

Atoms, molecules, and solids constitute the building blocks of matter as we experience it in daily life as well as in the scientific research in chemistry and physics (at thermal energies). The properties of matter can be described at a fundamental level by quantum mechanical treatment of the motions of electrons and nuclei. Quantum chemistry has initially focused on the computation of molecular electronic structure (approximate wavefunctions) and on the theories that may serve to make such calculations feasible to ever higher accuracy, and/or to help us understand the results, i.e., the description of the electronic structure in suitable concepts and pictures.

Although the electronic structure problem may not be called solved in the sense that one can do arbitrarily accurate calculations on arbitrarily large molecules, much progress has been made. For small- to medium-sized molecules, by now, very accurate results can, indeed, be obtained. As for larger molecules, there is still much development toward highly precise techniques that can be applied to increasingly larger systems. Density functional theory (DFT) and its approximations have established themselves as the tools of choice for large systems where quantum mechanical treatment is called for, because they can deliver useful results in the sense that the accuracy is sufficient for qualitative understanding and even quantitative information: e.g., geometries, frequencies, barrier heights, and all kinds of spectroscopic data from electronic excitation energies and nuclear magnetic resonance spectra.

The field of molecular modeling has further expanded beyond the realm of quantum mechanics, with the development of classical methods that are able to handle significantly larger systems and timescales and make predictions about both molecular and bulk material properties. Clearly, the choice of method to simulate a chemical system depends strongly on its size and type, as well as on the specific properties one seeks to predict. The Amsterdam Modeling Suite (AMS) collects a wide array of tools that can be used to model, analyze, and make predictions about a wide array of systems using a plethora of both quantum and classical methods, much like a Swiss-army knife of chemical simulations that offers the right tool for the right job. Although, at present, the range of applications is quite vast, AMS began with the development of its molecular DFT code, the Amsterdam Density Functional (ADF) program.

What is now called the ADF code[1,2] has been the first code, after attempts with the scattered-wave method, to make accurate calculations possible using density functional theory. The design principles of this code—density fitting, density function(al)s for exchange and correlation energies, 3D numerical integration, and the use of Slater type orbitals as basis functions—were at the time rather different from the prevailing *ab initio* methods and afforded for "large systems" (e.g., organometallic complexes and medium-sized clusters), at least an order of magnitude gain in efficiency. Several of the techniques are, at present, incorporated in virtually every DFT code, but since the vast majority of these codes are offsprings of the traditional *ab initio* codes, they are technically of course akin to their parent. Therefore, ADF, whose design principles are highlighted in Sec. III A, still differs in some essential aspects from the majority of present day DFT codes. The electronic structure methods (Sec. III B) that can be treated with ADF are density functional approximations (DFAs), including hybrids, double hybrids, and range-separation; see Sec. III B 1. Other methods and models based on many-body perturbation theory (MBPT)[3] such as second-order Møller–Plesset perturbation theory (MP2),[4] the random phase approximation (RPA)[5–8] (Sec. III B 2), and *GW* (*G*: single-particle Green's function, *W*: screened Coulomb interaction)-Bethe–Salpeter equation (BSE) (Sec. III B 3)[3,9–12] are available.

Some features of ADF technology make it possible to efficiently treat heavy elements that call for the inclusion of relativistic effects, subject to some theoretical development (notably a two-component formalism with the zero-order regular approximation, ZORA);[13–16] see Sec. III E.

Now that DFT calculations have reached maturity in the sense that they provide the users with sufficiently accurate electronic structure information for many purposes, the emphasis has shifted to property calculations. We will review a number of those properties, mostly various types of response properties, that can be calculated with ADF; see Sec. III F. Excitation energies (Sec. III F 1), several types of vibrational spectroscopy (IR, Raman, and resonance Raman) (Sec. III F 3), and their chiral counterparts (ECD, VCD, and ROA) (Sec. III F 5) are available. In addition, Nuclear Magnetic Resonance (NMR) and Electron Spin Resonance (ESR), in particular with heavy elements, are an important capability of ADF (Sec. III F 7).

Over the years, many further developments have produced a range of tools that have enlarged the chemical space and array of properties beyond those that could be simulated using ADF alone.

First, exactly the same technology that has been used for molecular DFT calculations was extended to periodic calculations. This has been implemented in the BAND code;[17,18] see Sec. IV.

Even faster electronic structure calculations can be performed by using semiempirical methods where some degree of outside information is employed, either empirical or from highly accurate benchmark calculations. We mention density functional tight-binding (DFTB) and MOPAC; see Sec. V.

Computational chemistry and materials science have progressed far beyond the electronic structure modeling and, by now, include many tools based on classical physical chemistry, often with a role for electronic structure calculations to supply a fundamental input in the form of parameters. The latter are described in Secs. VII–IX. In view of the proliferation of functionalities of this kind, the setup of the Amsterdam Modeling Suite (AMS) of programs has been organized in a transparent manner that recognizes this development, as explained in Sec. II.

II. AMS DRIVER

The most fundamental input of the AMS driver is the structure of the chemical system under study. The job of the AMS driver is then to handle all changes in the simulated system's geometry, e.g., during geometry optimization or molecular dynamics calculation, using the hereafter named engines such as ADF or DFTB for the calculation of energies and forces. Geometry optimization and transition state search use delocalized coordinates[19,20] and achieve excellent performance also for weakly bound systems by distinguishing weak from strong coordinates.[21] The AMS driver is, in general, responsible for the description and exploration of the potential energy surface (PES) of the system, defined using whatever method (classical, quantum, or hybrid) chosen by the user (see Fig. 1), a strategy it shares with the Quantum-regions Interconnected by Local Descriptions (QUILD) program.[21,22] (Acronyms used in Fig. 1 and elsewhere are collected in the Nomenclature.) The different tasks that a user can ask AMS to perform include single point energy calculations, geometry optimizations, vibrational analysis, molecular mechanics simulations, PES scan along specific coordinates, transition state search, grand-canonical Monte Carlo (GCMC) simulations, and others. Once a specific task has been requested, the user must also specify the particular engine to be used for the calculation. The engine will receive the structure from the AMS driver, perform its calculation, and return the computed energies, gradients, or other properties to the driver itself, which will perform additional analysis and then either terminate the calculation or update the system's structure, depending on the requested task (e.g., single point vs geometry optimization). The system is, in fact, flexible enough that it allows running external programs as an engine. In this way, users can combine the functionality in the AMS driver (tasks and PES point properties) with the energies and gradients of any molecular modeling program they have access to. For instance, a molecular dynamics simulation, while most commonly performed using a classical force field, can also be performed with any of the other methods that implement the calculation of forces, e.g., Density Functional Tight Binding (DFTB) if one wishes to perform a quantum simulation. To further expand on the capabilities of the engines, many other libraries, programs, and methods have been integrated within AMS. Examples include the plugin for molecular dynamics (PLUMED),[23] which can be used for enhanced sampling and free energy methods, or the Conformer–Rotamer Ensemble Sampling (CREST) approach,[24] which is a very specific implementation of metadynamics that is useful for the exploration of the conformer space. The power of AMS rests in its generality and the rich variety of the available engines, which are described in some detail in Secs. III–VIII, starting with the QM ones and then moving to the classical engines.

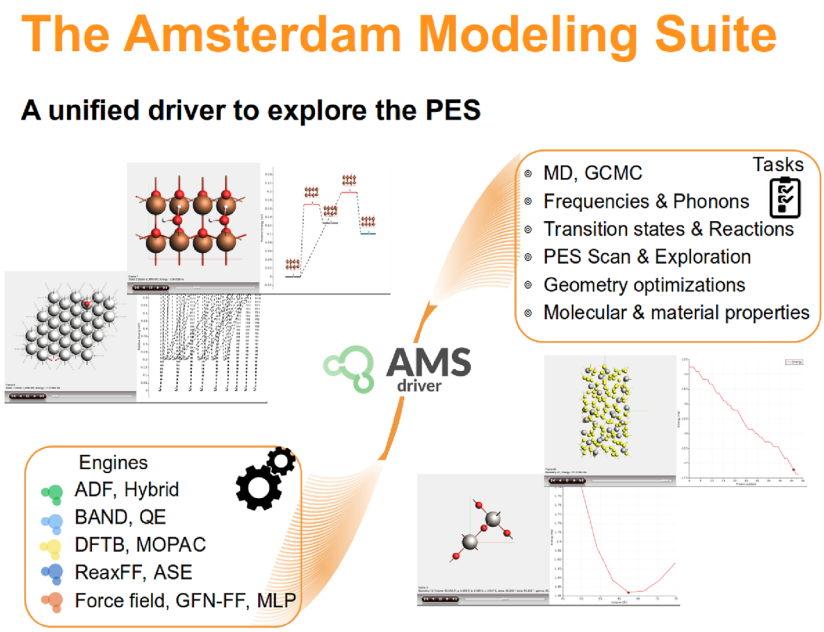

FIG. 1. The AMS driver reads the structure of the chemical system and invokes the relevant engine (such as ADF or DFTB or ReaxFF or an external engine) to compute a multitude of molecular properties. Acronyms listed at the end, in Nomenclature.

III. QM ENGINES: ADF

At the time of its inception—the early 1970s—the ADF code[1,2] was based on design principles that set it apart from all other electronic structure codes. At the time, a major stumbling block for *ab initio* calculations was the computation and processing of numerous (in principle N^4) two-electron repulsion integrals (ERIs). This problem has since been considerably mitigated by efficient prescreening techniques and other algorithmic improvements, but the evaluation of the many ERIs is still a computational challenge. The ADF code tried to do away with all ERI calculation. The design philosophy has been a balancing of the various approximations in order that not an inordinate amount of time is being spent on one step (e.g., high numerical precision in the Fock matrix elements by the processing of numerous very precise two-electron integrals), while other aspects (limited basis set and poor performance of the functional, e.g., Hartree–Fock exchange for bond energies) severely limit the accuracy. So, limited numerical precision of the Fock matrix elements in a direct 3D numerical integration procedure would be acceptable if, for example, the deviation of the basis set from the complete basis set limit (CBL) would restrict the accuracy of the energy (and orbital energies) anyway. The precision of the numerical integration should be sufficient to make other limiting factors for the accuracy of the calculation dominant. Then, density fitting to obtain the Coulomb potential in the integration points solves the ERI problem in combination with the use of density functionals for the exchange–correlation energy. Some of the considerations upon which the ADF approach was based have become less important with the advent of very much faster computers than were earlier available. In addition, other efficiency measures, such as linear scaling techniques, tend to shift the main computational burden to other places and, of course, have enhanced the computational speed of present day codes (and ADF as well). A feature such as the density fitting (Secs. III A 4 and III A 5) has, by now, for computational efficiency reasons, become a cornerstone of many codes (often under the name resolution-of-the-identity). Indeed, the density fitting has enabled efficient approximate calculation of ERIs, which has now supported the development of modern electron correlation methods [hybrids and RPA (Sec. III B 2), GW (Sec. III B 3), GW-BSE (Sec. III E 2), and non-equilibrium Green's functions (NEGF) (Sec. IV)]. As a result of the aforementioned methodological and technical advances, the chemical space that can be treated by ADF has increased steadily over the years. Actual limits are hard to specify since they depend strongly, of course, on the available computational resources and further on the type of system (heavy metal containing systems, for instance, $[Mo_{84}O_{188}S_{48}(AcO)_{24}]^{40-}$ (Ref. 25) or just organic systems (second/third row main group elements). In the latter case, open or extended systems benefit more from distance cutoffs. Calculations with 20 000 basis functions or more are feasible.

In Sec. III A, we first review the basic features of ADF.

A. Design principles

1. Numerical integration

An important pillar of ADF is the 3D numerical integration of the matrix elements of the one-electron Hamiltonian (Kohn–Sham in the DFT case). Defining this Hamiltonian as

$$\hat{h}^s(\boldsymbol{r}) = -\frac{1}{2}\nabla_{\boldsymbol{r}}^2 + v_{\mathrm{nuc}}(\boldsymbol{r}) + v_H(\boldsymbol{r}) + v_{\mathrm{xc}}(\boldsymbol{r}), \tag{1}$$

we have the numerical integration approximation as follows:

$$\begin{aligned} H^s_{\mu\nu} &= \int \chi_\mu(\boldsymbol{r})\hat{h}^s(\boldsymbol{r})\chi_\nu(\boldsymbol{r})d\boldsymbol{r} \\ &\approx \sum_k^P \chi_\mu(\boldsymbol{r}_k)[\hat{t}(\boldsymbol{r}_k) + v_{\mathrm{nuc}}(\boldsymbol{r}_k) + v_H(\boldsymbol{r}_k) + v_{\mathrm{xc}}(\boldsymbol{r}_k)]\chi_\nu(\boldsymbol{r}_k)w_k \\ \text{with } \hat{t} &= -\frac{1}{2}\nabla_{\boldsymbol{r}}^2, \quad v_H(\boldsymbol{r}_k) = \int \frac{\rho(\boldsymbol{r})}{|\boldsymbol{r}-\boldsymbol{r}_k|}d\boldsymbol{r} \text{ and } v_{\mathrm{xc}}(\boldsymbol{r}_k) = \frac{\delta E_{\mathrm{xc}}[\rho]}{\delta\rho(\boldsymbol{r}_k)}. \end{aligned} \tag{2}$$

Here, the sets $\{\boldsymbol{r}_k\}$ and $\{w_k\}$ are the integration points and weights according to the chosen quadrature scheme, with P being the total number of points.

A straightforward way to convert a typical Gaussian based code to a DFT code would be to just only calculate the matrix elements of the exchange–correlation potential v_{xc} through numerical quadrature. Then, the matrix elements of the Coulomb potential are assembled by processing a multitude of analytically evaluated two-electron integrals that each need to be computed to a sufficient numerical precision (at least 10^{-11} for their absolute values) in order not to lose too much precision in the final matrix elements. The calculation and processing of the two-electron integrals (electron repulsion integrals, ERIs) is thus one of the most computation intensive parts of many codes. ADF differs in that the total Fock or KS matrix elements are directly generated with the 3D numerical integration [as in Eq. (2)]. The precision of the matrix elements can be considerably smaller than the individual two-electron integrals in a standard code. The incompleteness of the basis set already limits the precision of the total energy or orbital energy with respect to the limit value for the chosen model. In many cases, there is no need to push the numerical integration far beyond that precision. As an added advantage, the direct numerical integration of the Fock matrix elements allows more suitable choices of basis set than Gaussians, and indeed, the ADF code uses Slater type orbitals, see Sec. III A 2, and BAND uses numerical atomic orbitals (NAOs) (supplemented with STOs or GTOs if desired); see Sec. IV.

It is to be noted that density functional calculations require numerical integration anyway, since the approximate exchange–correlation functionals are given as integrals over exchange–correlation energy densities that are, in the approximations used until now, functions of the density, its gradients, or even higher derivatives. These integrals are always done numerically, for which it is necessary to evaluate basis function values, and possibly also derivatives, at the integration points. These data can also be used without additional cost for the KS matrix elements of Eq. (2). It is to be recognized that the setting up of the KS matrix thus becomes an order $O(N^3)$ step in the calculation [in fact $O(N^2P)$ if N is the number of basis functions]. This can easily be linearized using elementary distance cutoff procedures.[2]

While this setup of DFT calculations formally has an $O(N^3)$ scaling, simply adding the v_{xc} matrix elements and the $E_{\mathrm{xc}}[\rho]$ energy to a traditional *ab initio* program leads back to the well-known $O(N^4)$ cost (without integral screening techniques used for larger systems) due to the two-electron integrals needed for the Coulomb potential matrix elements. Thus, the DFT addition would make it more time consuming than a straightforward HF calculation. At the

time when DFT became popular (the 1990s), this was not considered an important disadvantage, since the comparison was made with correlated calculations, which were much more computationally intensive than HF calculations anyway. However, the reputed $O(N^3)$ scaling was eventually achieved by the combination of numerical integration and density fitting (Sec. III A 4). We first address the numerical integration.

There is a variety of 3D numerical integration schemes available. The electronic structure codes and methods by Ellis,[26,27] which are at the root of the ADF program system, used a Monte Carlo type of integration method (the Diophantine method), which employed randomly generated points around each nucleus in θ and ϕ directions, with a decay in the r direction analogous to the Fermi distribution, with a characteristic inflection point at a distance R_0 from the nucleus corresponding to a reasonable atomic radius measure (for instance, Pauling radius or the van der Waals radius). This leads to interpenetrating atomic clouds of points. Although adequate for many purposes, this scheme converged relatively slowly with the number of points. Achieving arbitrarily high precision was difficult. This plays a role, for instance, in relativistic calculations, which require integration of high-l basis functions (and fitting functions, see Sec. III A 4) with strongly oscillating angular behavior and steep radial behavior close to the nucleus (mass–velocity, spin–orbit, and electric field gradient integrals).

Therefore, a different numerical integration scheme was further developed,[28,29] which used product Gaussian quadrature rules in fixed spatial regions. The advantage is that, according to the Gaussian integration rules (n points for exact integration of polynomials to order $2n-1$), the integration can be pushed to arbitrarily high precision.[28,29] It has to be taken into account that each nucleus presents a singular point in many integrands, and it is imperative to use quadrature rules that can handle this singularity. To address this problem, we place a sphere with fixed radius R_A around each nucleus and integrate in spherical coordinates. The r integration does not have, owing to the r^2 factor from the Jacobian, any problem at the $r = 0$ boundary of the $[0, R]$ domain for all relevant molecular integrals. This leaves an interstitial region between the atomic spheres and an outer region. The interstitial region has been partitioned into so-called Voronoi polyhedra and further partitioned into pyramids, which are truncated by the surface of the atomic sphere. This Voronoi integration, including how one can achieve convergence to high precision in each subregion, is described in detail in Ref. 29. Although it is no longer the default method in ADF (see the next paragraph), it is still available and a good choice for single point calculations. It is, for example, highly suitable to calculate the so-called Voronoi deformation density (VDD) charges[30] accurately.

The Voronoi method has a disadvantage when numerical derivatives with respect to nuclear displacements, as required for instance in geometry optimizations, are carried out. It may happen that in a geometry step the change in nuclear configuration causes a different partitioning of space into Voronoi polyhedra, for instance when the geometry step leads from a high-symmetry configuration to one with lower point group symmetry.[31] In that case, the small energy change does not benefit from the almost constant error when the Voronoi cells do not change but only has the precision of the overall integration grid. In view of the many geometry steps that may be necessary, it is not advantageous to use extra large grids. As detailed in Ref. 31, it is then more efficient to use the fuzzy cell method developed by Becke[32] because it behaves smoothly under geometry changes. The best strategy has been found to be a combination of the two methods: (a) atomic sphere regions are defined, as in the Voronoi scheme, with rapidly converging product Gauss integration in spherical coordinates in that crucial region, and (b) the Becke fuzzy cell integration is applied in the interstitial region. That still affords precision for integrals with singular behavior at the nucleus (like r^{-3} in spin–orbit and electric field gradient integrals) and leads to smooth energy behavior under small geometry changes. This is currently the default option in ADF.

2. Slater type orbitals

The numerical integration of the Hamiltonian matrix elements leaves great freedom in the choice of basis functions; the only requirement is that the functions can be evaluated at the integration points. ADF stands apart from most other similar programs due to its use of Slater-type orbitals (STO) as basis sets for the wave function expansion,

$$\chi(\vec{r}) = Z_{lm}(\theta, \varphi) r^{n-1} e^{-\alpha r}, \tag{3}$$

where $\vec{r} = (r, \theta, \varphi)$ is the position of the electron in terms of spherical coordinates, Z_{lm} denotes a real spherical harmonic (a combination of Y_{lm} and Y_{l-m}), which determines the angular momentum of the basis function, r^{n-1} is a radial factor that depends on the principal quantum number n, and α is a parameter that defines how fast the function decays far from the nucleus. Slater-type orbitals emerge naturally from atomic theory itself, and they represent the exact solution for a one-electron atom or ion. As such, they offer two advantages compared to other types of basis sets, such as Gaussians or plane waves, namely an intrinsically correct asymptotic decay and the presence of a cusp at the position of the atomic nucleus for s orbitals, features that other types of basis set require a larger number of basis functions to reproduce, up to three times as many.[33,34] In the case of Gaussian orbitals, these specific features of the exact wavefunction are usually approximated by employing contracted basis functions, i.e., fixed linear combinations of pure Gaussian functions. In the case of STOs, this additional step is not needed, making certain implementations simpler to handle.

STOs have not become popular. The reason is that three-center and four-center electron repulsion integrals (ERIs) are notoriously difficult with STOs. This is not a problem in ADF since the Hamiltonian matrix elements are not assembled by processing ERIs over the primitive basis functions [due to the numerical integration [Eq. (2)] and density fitting for the Coulomb potential and exact exchange, see Secs. III A 4 and III A 5, respectively].

The freedom of basis set choice offered by the numerical integration has been exploited by using numerical atomic orbitals (NAOs) in the BAND code for periodic structure calculations (see Sec. IV). NAOs are exact solutions of an atomic calculation, the radial part being given on a set of discrete r points. NAOs and STOs may also be used in conjunction, and there is no impediment against using Gaussians as well. Since a (contracted) Gaussian can be cast in the form of a NAO, a Gaussian basis can be handled by the program BAND (see Ref. 35 and Sec. IV).

3. Frozen core

The basis set determines the size of the KS Hamiltonian matrix, i.e., the dimension of the diagonalization problem. This dimension

is reduced by using STOs. It can be further reduced by applying the frozen core approximation. This approximation utilizes the fact that the core orbitals and their contribution to the potential can be precomputed on the basis of atomic calculations. For the valence orbitals, one may then use a general contraction scheme, where each valence basis function is augmented by a linear combination of core basis functions in such a way that the contracted valence basis functions are all orthogonal to the precomputed set of atomic core orbitals. This approach reduces the dimension of the problem to just the number of valence basis functions, while keeping full orthogonality to the frozen core orbitals. In particular, for systems with many heavy atoms (clusters), this results in a large saving of computation time.

The scheme can be summarized as follows: Let us denote the set of precomputed core orbitals on the atoms of the system (core AOs) as $\{\phi_j^c\}$. They are typically expressed in some large sets of primitive basis functions. A set of matching core STOs $\{\chi_j^c\}$ is introduced, i.e., for each core orbital, one STO of the same type (nlm) is added with an optimized exponent so as to maximize the overlap between the core STO and the core AO (a slightly more accurate result can be obtained when the exponent of the core STO is optimized to match only the "core tail" of the valence orbital). Denoting the set of valence basis functions as $\{\chi^v\}$, a set of core-orthogonalized valence basis functions $\{\tilde{\chi}^v\}$ can be produced by combining each valence basis function with a linear combination of core basis functions, $\tilde{\chi}_\mu^v = \chi_\mu^v + \sum_i A_{\mu i}\chi_i^c$. The coefficients $A_{\mu i}$ in these contracted valence basis functions can easily be determined from the orthogonality conditions $\langle\tilde{\chi}_\mu^v|\phi_j^c\rangle = 0$.[1] The secular problem is then set up in the basis $\{\tilde{\chi}^v\}$ so that orthogonality on all the cores in the system is automatically assured. All the STO overlap matrix elements are calculated analytically, also in the secular equation.

The frozen core approximation is automatic in a normal calculation based on basic atomic fragments, whose data (core orbitals and core and valence basis functions) are available in a database to be used in calculations on systems that incorporate the specific atomic fragment. This choice significantly reduces the dimension of the secular problem and is appropriate because deep core orbitals are not significantly affected by a change in chemical environment.

4. Density fitting: Coulomb potential

At the time of its inception,[1] one of the primary objectives of the ADF implementation has been to obviate the "curse" of the N^4 scaling of the ERI calculation and processing. As for the evaluation of the Coulomb potential, the solution has been found in the introduction of an auxiliary basis set (ABS) of atom centered functions (also STOs) in which the density can be expanded,

$$\rho(\boldsymbol{r}) = \sum_A \sum_{B\le A} \rho_{AB};\ \rho_{AB} = \sum_{\mu\in A,\nu\in B} P_{\mu\nu}\chi_\mu(\boldsymbol{r})\chi_\nu(\boldsymbol{r}),$$
$$\rho_{AB} \approx \tilde{\rho}_{AB} = \sum_{i\in A,B} a_i f_i. \tag{4}$$

Note that the fitting here is being done per atom pair (for diatomic densities ρ_{AB}) and is, therefore, an $O(N^2)$ step. Since the number of fit functions per atom pair is always limited, the solution of the least squares problem per atom pair takes little time. With due neglect of atom pairs with large internuclear distances, it is straightforward to make it $O(N)$ scaling. Some further advantages of atom-pair fitting have been listed in Ref. 2. The density fitting with an ABS is no longer the default scheme for the Coulomb potential but is being used for other purposes in the program, so we discuss it at this point.

The fit coefficients $\{a_i\}$ are determined by minimizing an error or deviation D of a fit density $\tilde{\rho}$ (one of the $\tilde{\rho}_{AB}$ in our case) from the exact density ρ, where D is defined as

$$D = \int (\rho(\boldsymbol{r}_1) - \tilde{\rho}(\boldsymbol{r}_1))d(\boldsymbol{r}_1,\boldsymbol{r}_2)(\rho(\boldsymbol{r}_2) - \tilde{\rho}(\boldsymbol{r}_2))d\boldsymbol{r}_1 d\boldsymbol{r}_2 \tag{5}$$

[possibly with Lagrange multipliers to ensure that $\tilde{\rho}(\boldsymbol{r})$ and $\rho(\boldsymbol{r})$ describe the same total charge, or higher moments of the density[1]]. The weight function $d(\boldsymbol{r}_1,\boldsymbol{r}_2)$ was initially chosen as just $\delta(\boldsymbol{r}_1,\boldsymbol{r}_2)$, reducing the evaluation of D to just a least squares fitting problem requiring only simple overlap integrals, which are evaluated analytically in ADF. Once the fitting coefficients for all atom pairs have been assembled in the set $\{a_i\}$, the Coulomb potential in the integration points is obtained from nuclear-attraction type integrals,

$$V_{\text{Coul}}(\boldsymbol{r}_1) = \sum_i a_i \int \frac{f_i(\boldsymbol{r}_2)}{r_{12}} d\boldsymbol{r}_2. \tag{6}$$

If N_f is the number of fit functions, which scales with the system size, this is a PN_f, i.e., $O(N^2)$, step. With two $O(N^2)$ steps, the scaling of the Coulomb potential is much reduced compared to the traditional $O(N^4)$ scaling. Assembling the Fock matrix by numerical integration is then an $O(N^3)$ step, and since diagonalizing the Fock matrix also scales as $O(N^3)$, this particular DFT implementation has overall $O(N^3)$ scaling.

The ABS fitting scheme requires a judicious choice of fitting functions. Standard sets are available in ADF, and they are tuned to the basis set quality chosen from the available basis set library. As documented in Ref. 36, these fit sets leave an error in bond energies and orbital energies that can be considered negligible, being at least two orders of magnitude smaller than the error due to the orbital basis set incompleteness, even for the QZ4P basis sets (quadruple zeta STO basis plus four polarization functions), where the basis incompleteness error is very small.

However, in the ABS scheme, the fit set cannot be extended systematically beyond the standard available sets, and such an extension may lead to overcompleteness problems. Therefore, for the Coulomb potential problem, an alternative density fitting scheme, called Zlm fit, has been developed.[31,37] It is based on a partitioning of the total density into (nonspherical) atomic parts; see below. An important advantage is that it does not require the input of a separate set of auxiliary basis functions. It can also be made nearly linear scaling and can easily be made more accurate without the risk of overcompleteness problems (which may arise with ABS schemes) by increasing the maximum l value of the spherical harmonic (Z_{lm}) expansion of the atomic density.

For the Z_{lm}-fit, the total electron density is split into atomic densities using partitioning functions p_A,

$$\rho(\boldsymbol{r}) = \left(\sum_{A=1}^{N_{atom}} p_A(\boldsymbol{r})\right)\rho(\boldsymbol{r}) = \sum_{A=1}^{N_{atom}} \rho_A(\boldsymbol{r}),$$
$$\text{where } \sum_{A=1}^{N_{atom}} p_A(\boldsymbol{r}) = 1 \text{ and } \rho_A(\boldsymbol{r}) = p_A(\boldsymbol{r})\rho(\boldsymbol{r}). \tag{7}$$

The functions $p_A(\boldsymbol{r})$ can be defined with the help of unnormalized atomic weight functions $\mathcal{P}_A(\boldsymbol{r})$,

$$p_A(\boldsymbol{r}) = \frac{\mathcal{P}_A(\boldsymbol{r})}{\sum_{A=1}^{N_{atom}} \mathcal{P}_A(\boldsymbol{r})}. \tag{8}$$

The first such partitioning was done by Hirshfeld, who used for $\mathcal{P}_A(\boldsymbol{r})$ spherical atomic densities.[38] This has led to the widely used Hirshfeld atomic charges as the integrals of the corresponding $\rho_A^{\text{Hirsh}}(\boldsymbol{r})$: $Q_A^{\text{Hirsh}} = Z_A - \int \rho_A^{\text{Hirsh}}(\boldsymbol{r}) d\boldsymbol{r}$. Many other partition functions have been used, for the same purpose as the present one, e.g., Refs. 32 and 39. However, a simple weight function,

$$\mathcal{P}_A = \eta_A \frac{e^{-2\|\boldsymbol{r}-\mathbf{R}_A\|/a_0}}{\|\boldsymbol{r}-\mathbf{R}_A\|^3}, \tag{9}$$

with advantages detailed in Refs. 31 and 37, proved adequate. The multiplier η_A is chosen, from experience, as $\eta_H = 0.3$ for hydrogen and $\eta_H = 1$ for all other atoms. The atomic densities can now be fitted by a spherical harmonic expansion to some maximum l value,

$$\rho_A(\boldsymbol{r}) \approx \tilde{\rho}_A(r,\theta,\phi) = \sum_{l=0}^{l_{\max}} \sum_{m=-l}^{l} R_{lm}^A(r) Z_{lm}(\theta,\phi), \tag{10}$$

where r, θ, and ϕ are polar coordinates with respect to the nuclear position $\mathbf{R}_A$ as origin. In view of the orthogonality of Z_{lm}, $R_{lm}^A(r)$ are determined by projection,

$$R_{lm}^A(r) = \iint Z_{lm}(\theta,\phi)\rho_A(r,\theta,\phi) d\theta d\phi. \tag{11}$$

The θ, ϕ integration can be done with an octahedral Lebedev grid of high enough angular momentum.[40] This affords a determination of function values $R_{lm}^A(r_p)$ in a set of suitably chosen radial points $\{r_p\}$. Since the r-values of the points of the numerical integration grid, on which the density and its derivatives as well as the Coulomb potential have to be determined, will not coincide with the predetermined r_p points, an interpolation is done with the help of cubic splines on the intervals between two r_p points. This representation of the density allows a rapid evaluation of the Coulomb potential such that near-linear scaling can be achieved.[37] An important advantage of the Zlm fit is the ease with which high accuracy can be achieved, as well as the fact that it poses no limitations on the angular momentum, contrary to the implementation of the ABS fitting scheme, which is restricted to $l_{max} = 4$.

The numerical integration and density fitting techniques together have the added advantage that they afford the use of different, possibly more suitable, basis functions than the ubiquitous Gaussian functions; see Sec. III A 2. Sambe and Felton[41] considered the implementation of DFT calculations in a standard Gaussian based code, where they adopted the ABS density fitting in order to avoid the $O(N^4)$ scaling of the Coulomb matrix evaluation. They did not apply atom-pair fitting but used global fitting of the total density with all fitting functions. This makes this step $O(N^3)$ scaling. In a next step, Dunlap *et al.*[42] changed the weight function $d(\boldsymbol{r}_1, \boldsymbol{r}_2)$ to $1/r_{12}$, which has since been generally followed if $1/r_{12}$ integrals can be easily computed, which is the case for Gaussian basis functions. Some considerations on the errors introduced by the fitting are given in Sec. III A 6. For a considerable time, the global fitting has been used in Gaussian based codes, but more recently, the advantages of an atomic pair based fitting have been widely recognized.[43–50]

5. Density fitting: Exchange and post-SCF correlation methods

For some electronic structure methods, such as hybrid DFT methods (and pure Hartree–Fock) and correlation methods such as MP2, RPA, and (BSE@)*GW*, which we review in Secs. III B 2 and III B 3, the calculation of ERIs is still required. These are not computationally prohibitive anymore and can handle special types of basis functions such as STOs and numerical atomic orbitals (NAOs) when the atom pair based fitting methods are applied. These methods for ERI calculation [now generally referred to as pair atomic density fitting (PADF), pair atomic resolution of the identity (PARI), local RI (LRI), or concentric atomic density fitting] have been available for exchange in ADF for almost two decades[51] and are constantly being improved. A recent publication[35] describes the technical aspects of the current implementation. Due to its efficiency,[35,47,52] PADF has been implemented not only with STOs but also with GTOs[47,49,50] and NAOs,[48] also in periodic boundary conditions.[53–55]

The advantages of PADF are best illustrated for the exchange matrix calculation, but similar considerations hold for (most) post-SCF correlation methods (see Sec. III B 2). The computational bottlenecks in HF or hybrid calculations are the evaluation of the exchange matrix K,

$$K_{\mu\nu} = \sum_{\kappa\lambda} P_{\kappa\lambda} v_{\mu\kappa\nu\lambda}, \tag{12}$$

where $v_{\mu\kappa\nu\lambda}$ is a four-center ERI and P is the one-particle reduced density matrix. To circumvent the explicit calculation of four-center ERIs, it is common practice to express the four-center ERIs in terms of two-center ERIs by writing

$$v_{\mu\kappa\nu\lambda} = \sum_{ij} c_{\mu\kappa,i} v_{ij} c_{\nu\lambda,j}, \tag{13}$$

where the coefficients c define a map from the two-center to the four-center ERIs. This map still scales as N^4.[56] In PADF methods, this scaling is reduced by approximating the product of two primary basis functions by pairwise sums only,

$$\begin{aligned}\rho_{\mu\nu}(\boldsymbol{r}) \equiv \chi_\mu(\boldsymbol{r})\chi_\nu(\boldsymbol{r}) &\approx \rho_{\mu\nu}^{\text{PADF}}(\boldsymbol{r}) \\ &= \sum_{j\in B} c_{\mu\nu,j} f_j(\boldsymbol{r}) + \sum_{i\in A} c_{\nu\mu,i} f_i(\boldsymbol{r}), \quad \mu \in A,\ \nu \in B.\end{aligned} \tag{14}$$

Here, the indices μ and ν are restricted to the atoms A and B and analogous for the auxiliary basis functions f.[45] Minimizing the Coulomb self-repulsion of the quantity $\rho_{\mu\nu}(\boldsymbol{r}) - \rho_{\mu\nu}^{PADF}(\boldsymbol{r})$ (corresponding to a weight function $d(\boldsymbol{r}_1, \boldsymbol{r}_2) = 1/r_{12}$) leads to the following expression:

$$\begin{aligned} c_{\mu\nu j} = \sum_{j'} v_{\mu\nu,j'} \left[v^{BB}\right]^{-1}_{j'j} + \sum_i v_{\mu\nu,i} \left[v^{AB}\right]^{-1}_{ij}, \\ i,\mu \in A, \quad j,j',\nu \in B, \end{aligned} \tag{15}$$

and analogously for $c_{\nu\mu i}$. v^{AB} denotes the Coulomb potential between the electrons on atoms A and B and $v_{\mu\nu,i}$ is a two-center ERI involving two AOs and a fit function. Due to this pairwise nature of the fit,

the number of non-zero elements in c scales asymptotically as N^2, and this is further reduced to N by introducing distance-dependent cutoffs.[57] Therefore, inserting (15) into (13) gives an expression for v, which scales as N^2. For the calculation of the exchange matrix, this is further reduced to linear by introducing system-specific cutoffs for v.

Expansion (14) is non-robust in the terminology of Ref. 58. This means that the total electron repulsion energy is not positive semi-definite,[58,59] which, in principle, could lead to a collapse of the SCF solution to an unphysically low energy. While this issue is hardly a concern in practice, PADF can also lead to an artificial increase in the magnitude of correlation energies (they become too negative).[35]

To prevent this issue, ADF uses specifically optimized auxiliary fit sets[48,57] of two different types. First, hand-optimized fit sets consisting of STOs of different qualities can be used,[57] which are referred to as `Normal`, `Good`, and `VeryGood`. The `Normal` and `Good` auxiliary fit sets are sufficiently accurate for basis sets up to TZ quality, while `VeryGood` quality is often advisable for QZ basis sets. An overview of these ABS types is provided in Ref. 57. Second, it is also possible to generate the ABS on-the-fly directly from the primary basis.[35] The algorithm for the fit set generation is described in Ref. 35 and closely related to the one by Ihrig *et al.*[48,60] The quality of the fit can be controlled by a single parameter ϵ_{bas}, where a smaller ϵ_{bas} indicates a larger fit set. Spadetto *et al.* have recently demonstrated[35] that RPA and MP2 results from canonical implementations can be reproduced systematically with the increasing size of the local RI basis.

To ensure numerical robustness also with smaller ABS, ADF uses a special projector method (technically related to Löwdin orthonormalization) for the exchange-matrix.[35] This procedure is, to the best of our knowledge, unique to AMS. PADF is also implemented for periodic boundary conditions in the BAND code (see Sec. IV).

6. Density fitting: Error estimates

Density fitting procedures introduce errors in the converged density and energy, in both the ABS and Zlm schemes. Since the Coulomb potential is approximated, the Self-Consistent-Field (SCF) solutions, i.e., the set of self-consistent Molecular Orbitals (MOs) and their energy eigenvalues, may be slightly different than the ones that would have been obtained through an analytical integral calculation, yielding an error in the charge density and hence in the energy. Since the energy is at a minimum under density variation, the error is expected to be small. (When density fitting or resolution of the identity is used for the individual ERIs, further considerations on the accuracy and variational stability of the energy calculation come into play;[35,58,59] see Sec. III A 5.)

An error analysis is done in the following way. By partitioning the exact density (using the MO coefficients and basis functions) into a fit density and a correction, we have

$$\rho(r) = \sum_{\mu,\nu} P_{\mu\nu}\chi_\mu(r)\chi_\nu(r) \equiv \rho_{\text{fit}}(r) + \Delta\rho(r). \tag{16}$$

The Coulomb potential is approximated as

$$V_{\text{fit}}(r) = \int \frac{\rho_{\text{fit}}(r')}{|r-r'|}\,\mathrm{d}\,r. \tag{17}$$

The Coulomb energy can then be expressed as

$$\begin{aligned} 2E_{\text{Coul}} &= \int \frac{\rho(r)\rho(r')}{|r-r'|}\,\mathrm{d}\,r\,\mathrm{d}\,r' \\ &= \int \rho(r)V_{\text{fit}}(r)\,\mathrm{d}\,r + \int \frac{\rho(r)\Delta\rho(r')}{|r-r'|}\,\mathrm{d}\,r\,\mathrm{d}\,r' \\ &= \int V_{\text{fit}}(r)(\rho(r)+\Delta\rho(r))\,\mathrm{d}\,r + \int \frac{\Delta\rho(r)\Delta\rho(r')}{|r-r'|}\,\mathrm{d}\,r\,\mathrm{d}\,r'. \end{aligned} \tag{18}$$

The energy is evaluated in ADF with the first term on the last line of Eq. (18), so it includes the first order term $\int V_{\text{fit}}(r)\Delta\rho(r)\mathrm{d}r$. This is printed and provides, by comparison with the approximate Coulomb energy $\int V_{\text{fit}}(r)\rho(r)\mathrm{d}r$, an estimate of the accuracy. The second order term $\int\Delta\rho(r)\Delta\rho(r')/|r-r'|\mathrm{d}r\mathrm{d}r'$ is not evaluated in ADF, because of the cumbersome integrals over STOs that would be required. The first order term should be small enough that the second order term can be trusted to be negligible. The integral of the square of $\Delta\rho(r)$ (the deviation D of Eq. (5) with $d(\boldsymbol{r}_1,\boldsymbol{r}_2) = \delta(\boldsymbol{r}_1,\boldsymbol{r}_2)$) is also calculated and gives an estimate of the magnitude of the neglected second order term.

In Gaussian codes, in principle, the exact E_{Coul} can be calculated. If, for computational efficiency reasons, density fitting is used, as is increasingly practiced, it is possible to determine the fit coefficients by minimizing D with $d(\boldsymbol{r}_1,\boldsymbol{r}_2) = 1/|\boldsymbol{r}_1-\boldsymbol{r}_2|$. It has been pointed out by Dunlap *et al.*[42] that this amounts to minimizing the second order error *in the Coulomb energy*. The fit, therefore, delivers the closest possible approximation of the exact Coulomb energy by the first order corrected Coulomb energy [the first term of Eq. (18)]. Incorporating the first order correction in the energy [using the first term of the last line of (18)] has been called *robust fitting* by Dunlap.[61] The energy calculation in ADF can be called robust. Dunlap *et al.*[42] have called minimizing D of (5) with $d(\boldsymbol{r}_1,\boldsymbol{r}_2) = 1/|\boldsymbol{r}_1-\boldsymbol{r}_2|$, i.e., minimizing the second order error, *variational fitting*. However, the Coulomb energy is not variational in the sense that the exact Coulomb energy would be a lower bound to the used approximation [the first term of the last line of (18)]. The approximation is lower than the exact Coulomb energy (the neglected second order term is positive definite). So, the Coulomb energy calculation in ADF cannot be called variational and would also not be so when $1/|\boldsymbol{r}_1-\boldsymbol{r}_2|$ is used for $d(\boldsymbol{r}_1,\boldsymbol{r}_2)$. Nonvariational fitting can also be made stable and accurate by judicious choice of the fit function sets, as are available in ADF; see, e.g., Ref. 36. The density fitting with $d(\boldsymbol{r}_1,\boldsymbol{r}_2) = 1/|\boldsymbol{r}_1-\boldsymbol{r}_2|$ emphasizes accuracy of the inner parts of the density, which are most important for the Coulomb energy. Fitting the density directly with $d(\boldsymbol{r}_1,\boldsymbol{r}_2) = \delta(\boldsymbol{r}_1,\boldsymbol{r}_2)$ in D in (5) is expected to be superior for the outer regions of the density. This is important when, for instance, the electrostatic interaction between the charge distributions (nuclei and electron density) of two molecules or fragments needs to be calculated (see Sec. III C 1).

B. Kohn–Sham DFT and wavefunction based correlation methods

1. Density functional approximations

ADF implements a wide array of different density functionals to choose from, too many to list here. These include local functionals

(LDA), generalized gradient approximations (GGA), and meta-GGA functionals, which make use of the second derivative of the density or the kinetic energy density, as well as hybrid functionals, which additionally incorporate a fraction of Hartree–Fock exchange. The efficient implementation of the exact-exchange matrix has been described in Sec. III A 5. In addition to the functionals that are native to ADF, it is also possible to invoke external libraries, which expand the range of usable functionals. These include XCFun[62] and LibXC,[63] whose functionals can be used in the same way as those native to ADF, albeit with some specific limitations described in the program's manual. A wide array of dispersion corrections are also available and can be combined with the aforementioned functionals, including the popular corrections by Grimme.[64,65]

2. Beyond hybrid-functionals

Beyond (meta-)GGAs and hybrid functionals, ADF features a wide range of fifth rung functionals, which incorporate electron correlation effects through virtual KS orbitals. All these methods are based on efficient RPA and MP2 implementations.[35,57] With these functionals, relativistic effects can be treated at the scalar and spin–orbit level, but, currently, analytical gradients are not yet supported.

ADF features many double-hybrid (DH) functionals[66] for ground-state energy calculations,[67] which use MP2 as its main ingredient. The MP2 correlation energy is the sum of a "direct" and second-order exchange (SOX) term, and the evaluation of the former is computationally less demanding.[57,68,69] Using global density fitting, the direct term has N^4 scaling,[60] but using the PADF expansion (15), cubic scaling is achieved.[57] In practice, the cubic step has a small prefactor and the quadratic step dominates the computational timings.[57]

While early DH functionals used both the direct and SOX terms, the computational simplicity of the direct term encouraged the development of DHs, which neglect other terms.[70–72] These functionals, referred to as DOD-DHs, reach the same level of accuracy as DHs, which include both MP2 components.[73,74] The direct MP2 step of DOD-DH calculations is much faster than that of the underlying hybrid calculation.

The SOX term of MP2 scales as N^5 using global density fitting. It can be evaluated in N^3 using PADF,[57] but due to a large prefactor, this is not competitive in practice. Therefore, this contribution is evaluated using a global fit in N^5, which still allows for applications to systems with 100–200 atoms.[35]

ADF also features exchange–correlation functionals based on the adiabatic connection fluctuation–dissipation theorem (ACFDT).[75,76] Within the ACFDT, the correlation energy is extracted from the density–density response function. It is obtained from P_0 via a Dyson equation whose kernel can be expanded in powers of the Coulomb interaction.[77–80]

The lowest-order approximation to this kernel (the Hartree kernel) yields the RPA,[5–7] which can alternatively also be derived from Hedin's *GW* approximation[9] in MBPT. In contrast to MP2,[81] the RPA is often very accurate by itself,[82–85] for instance, for the calculation of barrier heights[86–89] or non-covalent interactions.[81,90–92] Technically, the RPA is closely related to the direct MP2 term and comes with roughly the same computational cost. The PADF-based implementation in ADF makes single-point calculations on systems with about 1000 atoms and more than 20 000 basis functions (in TZ basis sets) feasible on a single compute node.[35] Along the lines of Ref. 93, RPA correlation energies have also recently been implemented in periodic boundary conditions in the BAND code (Sec. IV).

Going beyond the RPA, one obtains the approximate exchange kernel (AXK)[89] method or RPA+second-order screened exchange (SOSEX).[94–96] ADF implements a static version of the AXK method[97] as well as RPA+SOSEX.[97] ADF also implements the very recent class of σ-functionals developed by Görling and co-workers, in which the exact exchange–correlation functional is modeled as a power series of the eigenvalues of the product of the KS response function and the Hartree kernel.[80,98–101] While σ-functionals retain the computational efficiency of RPA, they give improved energetics for a large variety of reaction types as well as properties, including the ones for which RPA is already very accurate by itself.[99,100,102–104]

3. The GW method

Hedin's *GW* approximation (GWA, *G*: single-particle Green's function, *W*: screened electron–electron interaction)[9,11,105] to the electronic self-energy[3] gives access to accurate charged excitations,[106–109] which can be probed in (inverse) photoemission experiments, and spectral functions. In combination with the Bethe–Salpeter equation (BSE@*GW*),[110] the GWA also gives access to optical excitations (see Sec. III F 2).[10,12] The *GW* method has been implemented into ADF relatively recently.[111–114] Spin–orbit effects can also be treated at the BSE@*GW* level using ADF's two-component framework.[115] The molecular *GW* code can also be used with the NAO-based BAND engine (see Sec. IV), which also allows for the use of GTO basis sets.[116] Approximations to the self-energy beyond the GWA, so-called vertex corrections, are also available in ADF and are under active development.[116–119]

Solving the *GW* equations is computationally demanding,[111] and therefore, the default *GW* implementation in ADF emphasizes speed and low scaling with system size.[111] It is based on the (imaginary) space-time method[120–125] and uses non-uniform imaginary time and frequency grids tailored to each specific molecule.[112,126] In contrast to other implementations,[60,127,128] ADF solves the *GW* equations in the AO basis, where it utilizes the PADF expansion (15) to implement the time-determining steps of a *GW* calculation with quadratic scaling with system size. ADF then extracts the charged excitations by the analytical continuation of the self-energy.[120,129]

Most *GW* calculations are performed in a one-shot approach, referred to as G_0W_0,[130,131] or in its eigenvalue-only self-consistent extension (ev*GW*). These variants come with the advantage that only the diagonal elements of the self-energy need to be evaluated. In a method called quasiparticle self-consistent *GW* (qs*GW*),[132–134] the *GW* wave-functions are also updated self-consistently [while renormalization of the quasiparticle (QP) peaks in *G* and satellites are neglected]. The latter method is independent of the underlying exchange–correlation functional and typically among the most accurate *GW* variants[114,117,135] but requires the evaluation of the off-diagonal elements of the self-energy. In canonical implementations, this is computationally very demanding. In contrast to other low-scaling *GW* implementations,[123,124] ADF always calculates the full self-energy matrix, resulting in a highly efficient qs*GW* implementation.[113]

Following the implementation described in Ref. 60, it is also possible to perform a *GW* calculation completely on the imaginary frequency axis in the MO basis. Despite a higher scaling of N^4 with system size, this implementation is advantageous for smaller molecules due to a smaller prefactor. Due to its approximate treatment of the frequency dependence of the self-energy, the analytical continuation method is only reliable in the vicinity of the HOMO–LUMO gap and not applicable, for instance, to core states.[136] Those are, however, of interest to describe x-ray photoelectron spectroscopy (XPS).[136–139] Following the implementation in MolGW,[140] ADF, therefore, also features an analytical frequency integration-based implementation of the GWA, which treats the frequency-dependence of the self-energy exactly[128,140–142] and also allows for the inclusion of vertex corrections to *W* via the solution of a BSE. Combining these corrections with a corresponding correction to the *GW* self-energy itself allows us to go beyond *GW* systematically and leads to improved QP energy predictions in many scenarios.[118,119,143–145] This implementation scales as N^6 with system size.

C. Fragments, population, and energy analysis

1. Fragments

ADF employs a fragment oriented approach: any poly-atomic system is conceptually built up from smaller fragments, and the molecular one-electron orbitals are calculated as linear combinations of fragment orbitals. The final analysis is in terms of fragments (e.g., population analysis of fragment orbitals, energy of bond formation between the fragments; see, for example, Fig. 2). The simplest type of fragments consists of single isolated atoms, and this is the default choice for molecular calculations. However, fragments can also be larger moieties chosen by the user and may be based on chemically relevant parts of a system, such as functional groups, ligands, or even full molecules in case of supramolecular systems composed of mutually interacting but distinct parts. When one computes a system in terms of its constituent fragments, these fragments must have been computed beforehand and their properties must be passed on to the principal calculation. This is done by attaching fragment files, which contain the necessary information. A fragment file is simply the standard result file of an ADF calculation on that fragment. The orbitals of the full system are then expressed in terms of the fragment orbitals (FOs), i.e., the MOs converged during the fragment calculations. When the full set of FOs is used (occupied and virtual alike), this does not lead to any loss of accuracy compared to selecting the full initial primitive basis set and, from the purely mathematical standpoint, only amounts to taking an appropriate linear combination. The FOs can also be symmetrized whenever needed and then classified according to the specific irreducible representations of the symmetry point group of the molecule, resulting in symmetry-adapted linear combinations of fragment orbitals (SFOs). The main advantage of the fragment approach is to provide a clearer picture of the nature of the final converged MO in terms of more chemically relevant quantities, making it easier to analyze the chemistry and bonding of the system in terms of interactions between the FOs. This is already the case when the fragments are basic atoms, coefficients of full AOs in the MOs, and their populations being much more meaningful than these quantities for the primitive basis functions.

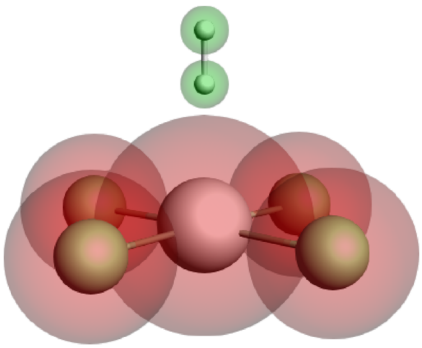

FIG. 2. The $[PtCl_4H_2]^{2-}$ complex split into two fragments using the AMS graphical user interface. Performing an ADF calculation on this system allows one to rationalize the molecular orbitals of the complex in terms of fragment orbitals belonging to the $PtCl_4^{2-}$ and H_2 moieties.

The fragment approach offers the technical advantage that the (small) bonding energy is calculated by integrating the *energy density difference* between the molecule and its constituents; this amounts to evaluating the energies of overall system and isolated fragments over the same integration grid, yielding enhanced numerical precision.

2. Bonding, energy decomposition analysis, and activation strain model

ADF offers a bonding energy decomposition analysis (EDA) according to the well-known Morokuma-type analysis of electron donor–acceptor interactions.[146–148] The charge-transfer/polarization term in this analysis is further decomposed into contributions per irreducible representation of the symmetry group of the overall system developed by Ziegler using an extension of Slater's transition state method to bond energy changes (ETS method[149,150]). It has been extended to open-shell systems (electron-pair bonding) in Ref. 151. This analysis is always performed by default and is a standard feature of ADF that is enabled by its fragment approach. The full description can be found in Ref. 152, including an explanation of the various terms as printed in the ADF output. The ADF program also affords an explicit study of separate polarization and charge transfer energy contributions by excluding user specified sets of fragment virtual orbitals in independent overall molecule calculations; see, for example, Ref. 153. The Constrained Space Orbital Variation (CSOV) method of Bagus *et al.*[154] is very similar.

The total bonding energy is broken down as follows:

$$\Delta E = \Delta E_{\text{prep}} + \Delta E_{\text{int}} = \Delta E_{\text{strain}} + \Delta E_{\text{exc}} + \Delta E_{\text{int}}. \quad (19)$$

The preparation energy ΔE_{prep} is the amount of energy, compared to the equilibrium configuration in the ground state, that is required to create the fragments in their geometric and electronic configurations that are used as the building blocks in the actual ADF calculation. The preparation often involves the strain energy ΔE_{strain} associated with a change of geometry, since the fragments as they exist in the overall molecule will often be distorted compared to their equilibrium ground states due to the interactions between fragments. Sometimes, we also have a change of electronic configuration associated with an excitation energy ΔE_{exc}, for instance, an excitation

that creates a suitable "valence state" for electron donor–acceptor interaction, or an ionization and electron attachment if interactions between ionic fragments are to be studied. A good example of the use of the strain energy is in the analysis of the transition state energy (barrier height) in chemical reactions: in the transition state, the geometries of the reactants are often significantly distorted compared to the free reactants. This part of the activation energy features prominently as the *activation strain* contribution to the total activation energy in the activation strain model (ASM) of chemical reactivity in the work of Bickelhaupt and co-workers.[155–157] Thus, the energy $\Delta E(\zeta)$ relative to the original, separate reactants A + B is decomposed along the reaction coordinate ζ into the strain energy $\Delta E_{\text{strain}}(\zeta)$ that is associated with the geometrical deformation of the individual reactants as the process takes place, plus the actual interaction energy $\Delta E_{\text{int}}(\zeta)$ between the deformed reactants,

$$\Delta E(\zeta) = \Delta E_{\text{strain}}(\zeta) + \Delta E_{\text{int}}(\zeta). \tag{20}$$

It is useful to project the reaction coordinate onto (the change in) a geometry parameter, which is critical in defining the progress of the chemical transformation instead of using the intrinsic reaction coordinate (IRC).[158] The height of the reaction barrier and its position along the reaction coordinate (early or late TS) can be understood in terms of the balance between the strain and interaction curves, $\Delta E_{\text{strain}}(\zeta)$ and $\Delta E_{\text{int}}(\zeta)$. The former depends on the rigidity of the reactants and the characteristic distortivity of a particular reaction mechanism, whereas the latter depends on the bonding capability of the reactants. A plot of $\Delta E(\zeta)$, $\Delta E_{\text{strain}}(\zeta)$, and $\Delta E_{\text{int}}(\zeta)$ is referred to as an activation strain diagram (ASD); see, for example, Fig. 3. Activation-strain analyses along the reaction coordinate can be automated using the PyFrag tool, which is part of the AMS suite.[159,160] The activation-strain analyses can also be carried out just at one point, for example, at the transition state, at which $\Delta E(\zeta_{TS}) = \Delta E^{\ddagger}$, which now consists of the activation strain $\Delta E^{\ddagger}_{\text{strain}}$ and the TS interaction $\Delta E^{\ddagger}_{\text{int}}$.

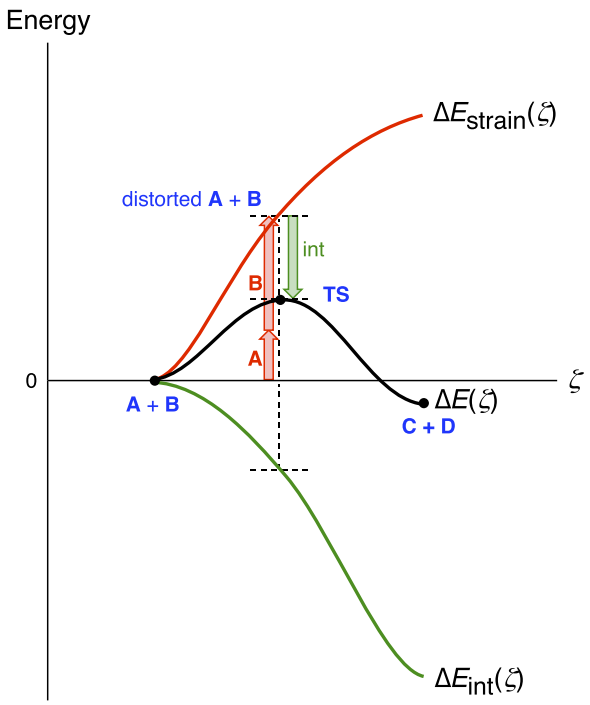

FIG. 3. Generic activation strain diagram (ASD) showing how the height and position of the TS for the conversion of A + B to C + D emerge from the interplay between strain and interaction curves.

The preparation energy ΔE_{prep} is obtained in the calculation of the fragment in the geometry of the overall calculation; this energy term is not printed in the energy decomposition analysis of the ADF calculation on the overall molecule. The terms in the printed analysis refer to the decomposition of the interaction energy between the prepared fragments,

$$\Delta E_{\text{int}} = \Delta E^{0} + \Delta E_{\text{oi}} = \Delta V_{\text{el}} + \Delta E_{\text{Pauli}} + \Delta E_{\text{oi}}. \tag{21}$$

ΔE^{0} refers to the energy of the intermediate wavefunction $\Psi^{0} = N\mathcal{A}[\Psi^{A}\Psi^{B}]$, which is the antisymmetrized and normalized product of the wavefunctions of fragments A and B placed at the positions they will have in the overall molecule. Usually, a contribution ΔV_{el} is distinguished, which refers to the purely electrostatic interaction between the electron density and the nuclei of fragment A with those of B, a situation that corresponds to the Hartree product or Hartree wave function $|\Psi^{H}\rangle = |\Psi^{A}\Psi^{B}\rangle$. This electrostatic interaction is often attractive due to the penetration of the electron densities, which lowers their repulsion.[152] The remainder of ΔE^{0} is called the Pauli repulsion because it results from the antisymmetry of the Ψ^{0} wavefunction, required by the Pauli principle. This is primarily a kinetic energy effect; see the breakdown of this term in Coulombic and kinetic energy contributions in Ref. 152. The Pauli repulsion leads to an overall repulsive character of ΔE^{0}, except when there is a very large electrostatic attraction as is the case for charged fragments. The orbital interaction energy ΔE_{oi} represents the typical occupied–virtual orbital interactions between the fragments, or the electron-pair bond formation between singly occupied orbitals.[151,152] This energy decomposition analysis (EDA) is automatic in ADF calculations and many examples and discussions of EDA exist in the literature.[150,153,157,161–167] Importantly, the magnitude and trends in the various EDA terms are determined by the underlying Kohn–Sham MO interaction mechanism, based on the aforementioned fragment approach, which provides a causal link between bonding (or reactivity) trends and the canonical orbital electronic structure of the fragments (or reactants). The ADF implementation also allows a further step to be taken, beyond the symmetry partitioning of the ΔE_{oi} term, to a partitioning of this term into contributions of orbital pairs in the natural orbitals for chemical valence (NOCV) theory of Mitoraj and Michalak,[168–171] which also provides insights into the nature of chemical bonds in the absence of symmetry. Note, however, that NOCVs are not canonical MOs.

ADF also implements other popular analysis features, such as the Voronoi Deformation Density (VDD) method for computing atomic charges Q_{A} of atoms A and changes in these charges ΔQ_{A} upon bond formation, decomposed into contributions from Pauli repulsive and stabilizing orbital interactions in the various symmetries or irreps belonging to the point group of the overall molecule (e.g., σ, π, and δ).[30,172] In the VDD method, the atomic charge Q_{A} is computed as the (numerical) integral of the deformation density

associated with the formation of the molecule from its atoms in the volume of the Voronoi cell of atom A,

$$Q_A = \int_{\text{V. cell A}} \rho(\mathbf{r}) - \sum_B \rho_B(\mathbf{r}) d\mathbf{r}. \quad (22)$$

The Voronoi cell of atom A is defined as the compartment of space bounded by the bond midplanes on and perpendicular to all bond axes between nucleus A and its neighboring nuclei (cf. the Wigner–Seitz cells in crystals). Here, $\rho(\mathbf{r})$ is the electron density of the molecule and $\sum_B \rho_B(\mathbf{r})$ is the superposition of atomic densities $\rho_B(\mathbf{r})$ of a fictitious promolecule without chemical interactions that corresponds to the situation in which all atoms are neutral. An asset of the VDD charge Q_A is the clarity of its physical meaning. Instead of measuring the amount of charge associated with a particular atom A, Q_A directly monitors how much charge flows, due to chemical interactions, out of $(Q_A > 0)$ or into $(Q_A < 0)$ the Voronoi cell of atom A, that is, out of or into the region of space that is closer to nucleus A than to any other nucleus. The chemical bond between two molecular fragments can be analyzed by examining how the VDD atomic charges of the fragments change due to the chemical interactions.[30,172] Note that the above equation leads to small artifacts that prohibit an accurate description of the subtle changes in atomic charges that occur in the case of weak chemical interactions, such as hydrogen bonds. This is due to the so-called front-atom problem that, in fact, all atomic-charge methods suffer from. This problem arises from the fact that, upon bond formation between originally separate atoms or poly-atomic fragments, the atomic cell (or any other way of assigning charge to a nucleus) changes for the front atoms that face the other fragment. To resolve this problem and, thus, enable a correct treatment of even subtle changes in the electron density, the change in VDD atomic charges ΔQ_A is defined as

$$\Delta Q_A = \int_{\text{V. cell A}} \rho(\mathbf{r}) - \sum_F \rho_F(\mathbf{r}) d\mathbf{r}. \quad (23)$$

Herein, ΔQ_A is directly related to the deformation density $\rho(\mathbf{r}) - \sum_F \rho_F(\mathbf{r})$ associated with forming the overall molecular complex with density $\rho(\mathbf{r})$ from the joining *molecular fragments* F with densities $\rho_F(\mathbf{r})$. This guarantees that in both, the non-interacting fragments F and the overall molecular complex, the exact same Voronoi cell is used for each atom A. Again, ΔQ_A has a simple and transparent interpretation: it directly monitors how much charge flows out of $(\Delta Q_A > 0)$ or into $(\Delta Q_A < 0)$ the Voronoi cell of atom A as a result of the chemical interactions between the fragments F in the overall molecular complex. An important feature of the ΔQ_A charges is that they can be decomposed into the contribution $\Delta Q_{A,Pauli}$ stemming from the Pauli repulsion step, from Ψ^H to Ψ^0, and the contribution $\Delta Q_{A,oi}$ associated with the orbital interaction step, from Ψ^0 to Ψ^{SCF} (see above). Either of these two atomic-charge terms can be decomposed into contributions to the deformation densities from the orbitals of the various irreducible representations Γ, see below,

$$\Delta Q_A = \Delta Q_{A,Pauli} + \Delta Q_{A,oi} = \sum_\Gamma \left(\Delta Q^\Gamma_{A,Pauli} + \Delta Q^\Gamma_{A,oi}\right). \quad (24)$$

In this way, a detailed picture arises from the effect of various (Pauli) repulsive and stabilizing orbital interactions, which perfectly matches with and augments the energy decomposition analysis (EDA).

Another analysis technique is the Quantum Theory of Atoms in Molecules (QTAIM).[173] This method is based on a spatial partition of the electronic density based on the atomic components of the system. Its implementation is fully integrated within ADF and the GUI through the `AMSview` module, allowing a user to perform a topological analysis and produce a list of the molecule's electron density critical points and bond paths that can be visualized. At the critical points themselves, other properties are also calculated, including the derivatives of the electron density, ellipticity, Jenkins' metallicity index,[174] the reduced density gradient, DFT energy density variation rates,[175] and Abramov's local energy components.[176] In addition to this, many general descriptors that have found use in the chemical literature can be computed.[177] These include electronegativities, hardnesses, hyperhardnesses, electrophilicity indices,[178] dissociation energies,[179] and electrodonating and electroaccepting powers.[180]

It should be noted that the above lists are not exhaustive since over the past decades, a plethora of analysis tools have been implemented and fully integrated within AMS, although it is not possible to list and explain them all here, but the manual offers a much more extensive overview of the available methods.

D. Charge transport

ADF can be used to calculate parameters needed in approximate methods that model charge transport properties in the hopping regime, such as charge transfer integrals. These parameters can also be calculated with the semiempirical DFTB method (see Sec. V A), but these are expected to be less accurate than those obtained using ADF. In theoretical models of charge transport in organic materials,[181–183] the whole system is divided into fragments, in which an electron or a hole is localized on a fragment and can hop from one fragment to another. As such, due to the fragment-based implementation of both ADF and DFTB, these properties are easily obtained. In the tight-binding approximation that is used in these models, the electron or hole is approximated with a single orbital, and it is assumed that only the nearest neighboring fragments can couple. The models require accurate values of electronic couplings for charge transfer (also referred to as charge transfer integrals or hopping matrix elements) and site energies (energy of a charge when it is localized at a particular molecule) as a function of the geometric conformation of adjacent molecules. Charge transfer integrals for hole transport can be calculated from the energetic splitting of the two highest-occupied molecular orbitals (HOMO and HOMO-1) in a system consisting of two adjacent molecules, also called "energy splitting in dimer" (ESID) method. For electron transport, these can be calculated from the two lowest-unoccupied orbitals (LUMO and LUMO+1) in this ESID method. ADF and DFTB can also calculate transfer integrals based on the direct method by using a fragment approach.[182,183] The charge transfer integrals obtained in this way may differ significantly from values estimated from the energy splitting between the highest occupied molecular orbitals in a dimer. The difference is due to the nonzero spatial overlap between the molecular orbitals on adjacent molecules. In addition, the direct method is applicable in cases where an orbital on one molecule couples with two or more orbitals on another molecule, and the matrix elements of the molecular Hamiltonian in the basis of fragment orbitals are

used to calculate site energies and charge transfer integrals. Similarly, the overlap integrals between fragment orbitals are calculated. No explicit electrons are removed or added in this case. For electron mobility calculations, the fragment LUMOs are considered. For hole mobility calculations, the fragment HOMOs are considered instead.[182,183] All these functionalities are integrated into ADF and can also be invoked through the GUI.

E. Relativistic effects

Relativistic effects can be crucial in the modeling of certain chemical systems and phenomena. Usually, such effects are separated into two kinds of contributions, i.e., scalar and spin–orbit,[184,185] with the latter collecting all couplings between the electron spin and the electric potential generated by the other charges in the system. In ADF, the approximation of including coupling with only the electric field of the nuclear charges is never practiced. The screening of the nuclear charge by the field of the electronic charge distribution [both (frozen) core and valence charge distribution] is taken into account. Scalar relativistic effects can be crucial when dealing with systems composed of heavy atoms, while spin–orbit couplings are necessary to simulate phenomena such as phosphorescence, inter-system crossing, and fine structure splittings. ADF includes scalar relativistic effects using the Zero Order Regular Approximation (ZORA)[13–15,186] method by default, although other options are also available. The especially adapted basis sets that must be used whenever a relativistic calculation is performed are provided with the code. Relativistic effects are also crucial when simulating the properties of core electrons as in the case of x-ray spectroscopy (such as K- and L-edge x-ray absorption) but also for magnetic spectroscopies such as NMR and ESR. See Sec. III F 7 for more information. Geometry optimizations and Hessian calculations with the ZORA method are also supported.[16] Scalar relativistic calculations with the ZORA method are with ADF as easy and efficient as nonrelativistic calculations. The ZORA implementation has thus removed any barrier toward inclusion of (scalar) relativistic effects.

In addition to the ZORA method, ADF implements the Exact Two-Component (X2C) method and the regular-approach variant (RA-X2C),[185,187,188] which are recommended whenever one requires a very accurate modeling of core electrons of very heavy atoms. Note that while X2C can, in principle, lead to the same results as the four-component Dirac equation, approximations are always introduced, as is the case in ADF. In the X2C and RA-X2C methods implemented in ADF, first, the matrix representation of the four-component Dirac equation for a model potential (MAPA) of the molecule is calculated for the given ADF basis set, using the modified Dirac equation by Dyall[187] for X2C, or using the regular approach[185] to the modified Dirac equation for RA-X2C. The modified Dirac equations differ in the way the pseudo-large component 2-spinor ϕ^L is defined, having to provide the small component ψ^S of the Dirac wave function either via the relation $\psi^S = (2c)^{-1}\boldsymbol{\sigma}\cdot\mathbf{p}\phi^L$ for X2C, or via the RA relation $\psi^S = (2c - V/c)^{-1}\boldsymbol{\sigma}\cdot\mathbf{p}\phi^L$ for RA-X2C. While X2C and RA-X2C converge to the same value at the basis set limit, the latter form has the advantage that ϕ^L does more closely resemble the true large component solution ψ^L of the Dirac equation. With either of these definitions, the modified Dirac equation assumes the form

$$\begin{pmatrix} V & T^1 \\ T^1 & T^2 \end{pmatrix}\begin{pmatrix} \psi^L \\ \phi^L \end{pmatrix} = E\begin{pmatrix} 1 & 0 \\ 0 & S^2 \end{pmatrix}\begin{pmatrix} \psi^L \\ \phi^L \end{pmatrix}, \tag{25}$$

albeit with different definitions of the individual operators,

	X2C	RA-X2C
T^1	$\frac{p^2}{2}$	$\boldsymbol{\sigma}\cdot\mathbf{p}\frac{c^2}{2c^2-V}\boldsymbol{\sigma}\cdot\mathbf{p}$
T^2	$\boldsymbol{\sigma}\cdot\mathbf{p}\frac{V-2c^2}{4c^2}\boldsymbol{\sigma}\cdot\mathbf{p}$	$\boldsymbol{\sigma}\cdot\mathbf{p}\frac{c^2}{V-2c^2}\boldsymbol{\sigma}\cdot\mathbf{p}$
S^2	$\frac{p^2}{4c^2}$	$\boldsymbol{\sigma}\cdot\mathbf{p}\frac{c^2}{(2c^2-V)^2}\boldsymbol{\sigma}\cdot\mathbf{p}$

All operators are readily evaluated using numerical integration and some appear also in the ZORA formalism. After the matrix representations are formed and eigensolutions are determined, the positive energy (electronic) four-component Dirac solutions are transformed exactly to two-components. This transformation provides an effective one-electron two-component kinetic energy operator, which is then assumed to be constant in the ensuing ADF SCF calculation on the molecule, similar to what is done in the ZORA approach.

After having constructed the appropriate relativistic Hamiltonian, the choice between the scalar and spin–orbit versions of each method must then be made, depending on the properties that one wishes to simulate. It should be noted that in the case of spin–orbit calculations, the usual point-group symmetry that characterizes the molecule no longer applies and is, instead, replaced with the relativistic double-group symmetry. For closed-shell systems, two electrons can occupy the same energy level, although contrary to the normal (without spin–orbit couplings) case, these two electrons are not directly associated with spin-α and spin-β, but rather with the more general Kramers' symmetry. Finally, the program can also handle non-collinear electronic densities in the XC functional, i.e., systems in which the XC functional depends on the spin magnetization density vector field that can point toward different directions throughout the system. The user may choose whether to use only a collinear part of spin magnetization density vector field in the XC functional (such that the XC functional only depends on one component of the spin magnetization density vector field) or to remove this restriction and perform a fully non-collinear calculation.

We also note that ADF can describe finite nuclear volume (FNV) effects via the spherical Gaussian distributions of the nuclear charges.[189,190] FNV effects are not intrinsically relativistic, but they tend to be noticeable predominantly in relativistic calculations because of the large relativistic effects on the deep-core "tails" of s and $p_{1/2}$ atomic orbitals. The NMR J-coupling module in ADF implements a spherical Gaussian model also for the nuclear magnetization.[190] Examples are discussed later.

F. Response properties: Spectroscopy in ADF/AMS

Spectroscopy comes in many different forms. There is an enormous variety and richness of information about chemical systems that can be extracted via different types of spectroscopic techniques. As the complexity of the systems under investigation

TABLE I. Spectroscopy in AMS, according to the method and subprogram used. Note that ADF is only used for molecule (0D) systems.

Spectroscopy	Periodicity	Engine	Method
IR	1D, 2D, 3D	ADF, DFTB, MOPAC	Harmonic approximation
Phonons	1D, 2D, 3D	All except ADF	Harmonic approximation
VCD	0D	ADF, BAND, DFTB	Harmonic approximation
Raman	0D	ADF	Harmonic approximation
ROA	0D	ADF	Harmonic approximation
RR, SERS	0D	ADF	Harmonic approximation, complex polarizability
UV/Vis	0D	ADF	(s)TDDFT/TDA TDDFT + TB BSE@*GW*
ECD	0D	ADF	(s)TDDFT/TDA TDDFT + TB
NMR	0D	ADF	Response theory
OR	0D	ADF	Response theory
EELS, susceptibility	1D, 2D, 3D	BAND	TD-CDFT

increases, however, a direct interpretation of experimental spectroscopic parameters can be elusive, rendering computational simulation an invaluable tool of prediction and analysis. Furthermore, spectroscopic signals are often physically related to important non-spectroscopic phenomena. For example, the energy transfer rate between a donor system and an acceptor system can, in some cases, be related to the convolution of the one-photon emission and absorption spectrum of the donor and acceptor, respectively. Therefore, the ability to simulate spectroscopic signals accurately and efficiently is a crucial feature of a quantum chemical simulation package. Consequently, significant effort has been made into implementing and validating simulation methods for a vast array of spectroscopic parameters within AMS, which offers an ample choice of methods within its many engines to simulate the spectra of molecular systems both *in vacuo* and embedded in a complex environment, as well as bulk materials (see Table I for an overview). Spectroscopic techniques can be classified in different ways; here, we present them according to the type of degrees of freedom investigated by the different techniques. (For a related discussion, see also Ref. 191.)

1. Electronic excitation energies: TDDFT

For electronic excitation energies, ADF implements Time-Dependent DFT (TDDFT), which is based on the first-order time-dependent perturbation expansion of the electronic density.[192]

TDDFT calculations with ADF can be based on a variety of exchange–correlation functionals along with the corresponding Kohn–Sham potentials and response kernels. For hybrid functionals, the appropriate percentage of the Hartree–Fock kernel is used. The DFA part of the kernel is typically approximated with the adiabatic LDA kernel. For range-separated density functional approximations (DFAs), the kernel consists of the range separated ALDA plus the kernel of range-separated Hartree–Fock. Extensive tests in the literature[193–195] of the performance of the various functionals in TDDFT calculations show on the whole decent performance, although the variations among functionals can be bewildering. The quality of any given functional may vary from molecule to molecule; there is not a clear and consistent winner. The Kohn–Sham potentials that are derived from the DFA functionals all suffer from the particular deficiencies of too shallow behavior over the molecular region (hence the strongly upshifted orbital energies)[196] and the lack of the proper $-1/r$ asymptotic behavior. In particular for properties that depend strongly on the outer region of the molecule [Rydberg excitations or high excitation energies, (hyper)polarizabilities], it is important to use an XC potential with correct asymptotic behavior. The statistical average of orbital potentials (SAOP) method,[197–199] which approximates the exact Kohn–Sham potential, combines the advantages of correcting the too shallow nature of standard (LDA, GGA, and hybrid) potentials in the interior molecular region and introducing a proper $-1/r$ asymptotic behavior. In particular for small molecules, with often valence and Rydberg excited states intermixed, excitation spectra as well as other response properties (dipole and quadrupole polarizabilities, Cauchy coefficients, and hyperpolarizabilities) are much improved.[199,200] With Hartree–Fock and hybrid functionals, the virtual orbitals suffer from a very unrealistic diffuse character. This is remedied by the SAOP potential, which leads to many excitations having an unambiguous single orbital-to-orbital transition character.[200]

Spin–orbit coupling can be included in the TDDFT calculation of excitation energies for closed-shell molecules and is currently being extended to open-shell systems. Two methods can be used in ADF. The first one includes spin–orbit coupling as a perturbation to a scalar relativistic calculation of excitation energies, in which spin–orbit coupling matrix elements (SOCMEs) between different electronic states are calculated.[201] The second one includes spin–orbit coupling self-consistently in the ground state calculation.[202] If spin–orbit coupling is large, the second one is more accurate but is also more time-consuming. The results of these spin–orbit coupled TDDFT calculations include the calculation of the zero-field splitting (ZFS) of triplet excited states and the calculation of radiative rate constants, which could be used to calculate radiative phosphorescence lifetimes, relevant, for example, in the modeling of organic light-emitting diodes (OLEDs).[203] For open-shell systems, it is possible to take into account the effects of spin–orbit coupling

using proper spin states [restricted open-shell Kohn–Sham (ROKS) calculations] and adding the spin–orbit coupling perturbatively.[204]

Depending on the available computational resources, the solution of the full TDDFT equations can be too cumbersome for large molecular systems. Therefore, several approaches that have been devised to find approximate solutions at a much more favorable computational cost are available in ADF. The simplest of these is the Tamm–Dancoff approximation (TDA), which neglects the contributions of de-excitations and, therefore, halves the size of the response matrix.[205] The so-called simplified TDDFT (sTDDFT) and simplified TDA (sTDA) approaches are also implemented in ADF.[206,207] In these methods, the time-dependent DFT equations are simplified by the evaluation of the two-electron integrals as short-range damped Coulomb interactions between (transition) charge density monopoles and a truncation of the single excitation expansion space. The calculation of these terms is often the bottleneck of the calculation; therefore, these methods offer significant computational savings, expanding the range of systems that can be modeled. sTDDFT and sTDA are best suited if a (meta-) hybrid or a range-separated-hybrid functional is employed in the SCF for the ground states. These methods will speed up the calculation drastically in comparison with the standard time needed for TDA or TDDFT calculations of excitation energies for hybrids. A closely related method that can be used to approximate the solution to the TDDFT equations, and whose goal is also to avoid the computation of the expensive two center integrals, is given by the TDDFT plus tight-binding method[208] (TDDFT+TB; see Sec. V A for the TB method). The basic idea of TDDFT+TB is to use the molecular orbitals from a DFT ground state calculation as an input to an excited state calculation with TDDFTB coupling matrices. The coupling matrix used for the response calculation is constructed from the DFT orbitals; therefore, it does not rely on any specific DFTB parameterization; rather, it only needs chemical hardness (for singlet excitations) and the magnetic Hubbard parameters (triplet excitations). These are physical properties of the atoms that have been calculated and tabulated for the entire Periodic Table. If many excitations are required, this method will speed up the calculation drastically in comparison with the effort needed for the TDDFT calculations of excitation energies. This method is best suited if a (meta-)GGA or LDA is used in the SCF. All these approximations use molecular orbitals from a DFT ground-state calculation and rely on an atomic monopole approximation for the transition density in order to avoid the calculation of certain expensive integrals. The major difference between sTDDFT/sTDA and TDDFT+TB is that the latter is a pure density functional approach, while sTDA and sTDDFT use hybrid functionals in the calculation of both the ground state and the excited state. TDDFT+TB can be used for excited-state geometry optimization jobs.[209] The aforementioned techniques evaluate a system's excitation energies from the poles of the system's response function, but excitation energies can also be calculated from the frequency-dependent complex polarizability, a technique that is exploited by the PolTDDFT method,[210] a fast alternative to solve the TDDFT equations in the space of the density fitting auxiliary basis set, available for both pure and hybrid functionals.[211] This method achieves high efficiency by simplifying the double sum over occupied–virtual pairs in the definition of the complex dynamical polarizability, allowing an easy calculation of such matrix as a linear combination of constant matrices with photon energy dependent coefficients, allowing one to calculate both absorption and electronic circular dichroism spectra.[210,212] The results of a PolTDDFT calculation can be further analyzed using a variety of techniques, including a fragment projection analysis approach,[213] by looking at the transition contribution maps,[214] or individual component maps of the oscillatory or rotatory strength.[215,216]

Electronic absorption techniques are not limited to the UV–Vis energy range but can be extended to the x-ray part of the spectrum. Techniques such as x-ray photoelectron spectroscopy (XPS) and x-ray absorption spectroscopy (XAS), often also abbreviated using the acronyms x-ray absorption near edge structure (XANES) and near edge x-ray absorption fine structure (NEXAFS) for core–valence excitations, are all widely used to extract information on the core electrons of chemical systems, among other things.[217–224] Finally, ADF also implements the calculation of x-ray emission spectra (XES) with a frozen orbital, one-electron approach, which uses orbital energy differences between occupied orbitals to model the x-ray emission energies.[218,225] These types of spectra can be efficiently computed using ADF. Note that for x-ray spectroscopies, origin-independent quadrupole intensities are available.[226] Moreover, ADF implements a wider selection of electronic spectroscopic techniques involving circular dichroism (CD), which can be used to investigate the enantiomeric spectroscopic properties of chiral systems; see Sec. III F 5.

2. Electronic excitation energies: BSE@GW

The *GW*-Bethe–Salpeter equation (BSE@*GW*) method[10,12,227] is becoming an increasingly popular alternative to TDDFT.[228] A BSE@*GW* calculation starts with a ground state DFT calculation, is followed by a *GW* calculation (see Sec. III B 3), and solves a Casida-type equation[229] to obtain optical excitations.[12] BSE@*GW* is typically a more accurate method than TDDFT[108,114,135,230] and is well-suited for the description of charge-transfer excitations.[231–234] BSE@*GW* in ADF is also available with spin–orbit coupling[115] and compatible with polarizable continuum (COSMO) or discrete polarizable models described in Sec. VI. The implementation follows Refs. 235–237.

Traditionally, the computational bottleneck in a BSE@*GW* calculation is the *GW* step. However, this step is implemented very efficiently in ADF (see Sec. III B 3). Additional computational complexity arises from the calculation of the matrix elements of the kernel of the Casida equations, which scales as N^2 with system size using PADF (see Sec. III A 5).[114] Even when the *GW* step is done self-consistently with qs*GW*, a BSE@*GW* calculation with ADF is typically only about a factor of two more expensive than a TDDFT calculation using a hybrid functional. The efficiency and scalability of the BSE@(qs)*GW* implementation in ADF have recently been demonstrated by calculating the 12 lowest excitations of the six chromophores of the photosystem II (PSII) reaction center (RC) shown in Fig. 4 with nearly 2000 correlated electrons in a TZ3P basis[112] on a single compute node.[114]

A BSE@*GW* calculation is only as reliable as the underlying *GW* calculation. Its accuracy will depend on the selection of the exchange–correlation functional and the level of self-consistency in the *GW* calculation.[135,230,238] While BSE@G_0W_0 and BSE@ev*GW* reduce the dependence on the DFT starting point, only BSE@qs*GW* makes the results completely independent of the choice of an

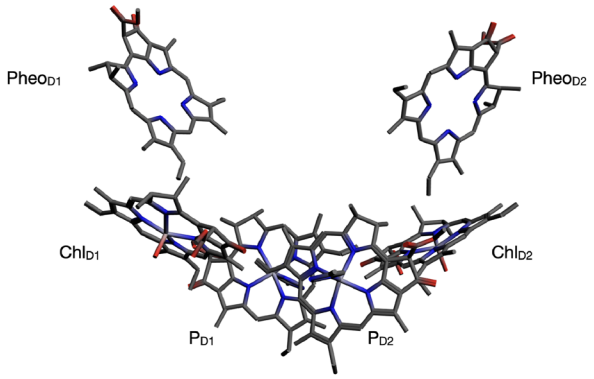

FIG. 4. Chromophores of the photosystem II reaction center. Figure from A. Förster and L. Visscher, J. Chem. Theory Comput. **18**, 6779 (2022). licensed under a Creative Commons (CC-BY) license.

exchange–correlation functional.[114] However, a BSE@G_0W_0 calculation where the G_0W_0 step is performed based on a range-separated hybrid functional (for instance, CAM-B3LYP[239] or LRC-ωPBE[240]) is an excellent alternative to a BSE@qsGW calculation[108,241] and only marginally more expensive than a TDDFT calculation with a hybrid functional.

3. Vibrations: IR, Raman, resonance Raman, and vibronic structure

a. IR spectroscopy. Vibrational spectroscopy yields information about the nuclear motion, be it molecular vibrations or phonons in solids. Vibrational spectra that can be simulated using AMS include infrared absorption (IR) spectra, Raman spectra, as well as their chiral equivalents; see Sec. III F 5. Depending on property and method, these spectra are computed either analytically or numerically via the finite-difference differentiation of the relevant molecular property, e.g., the molecular dipole moment for IR spectroscopy or the real electronic polarizability in the case of spontaneous Raman. In addition, mode-selective techniques such as mode-tracking[242] or IR intensity-tracking[243] have been adopted in the AMS package. The Mobile Block Hessian (MBH)[244,245] method is useful when calculating vibrational frequencies of a small part of a very large system (molecule or cluster). Using MBH, it is possible to treat parts of the system as rigid blocks.

An alternative method of simulating an IR spectrum is through the autocorrelation function of the dipole moment obtained from a molecular dynamics calculation.

Both options are available in AMS.

b. Raman. Raman spectroscopy is, instead, related to the molecular electronic polarizability, evaluated as a response function of the quantum-mechanical density and can, therefore, only be calculated using a QM engine. While a Raman spectrum is in many ways related to the IR spectrum, it offers several advantages over the latter, such as the possibility of recording spectra for systems in aqueous solution, and is otherwise complementary to it, given that for symmetric systems the selection rules for either spectroscopy are mutually exclusive.[246,247]

c. Resonance Raman. Often spectroscopic techniques cannot be entirely classified as purely electronic or vibrational but rather as a combination of the two.[247] It is the case of resonance Raman spectroscopy (RR), which measures the non-linear scattering of a system under a laser light that is in resonance with a particular (typically electronic) molecular transition of the system. The RR spectrum often differs from the traditional Raman spectrum since it does not follow the same selection rules, as the imaginary part of the polarizability contributes to the intensity. The resonance condition can lead to significant enhancement of the spectroscopic signal, wherein lies the main advantage of the technique. Formally, the difference is that because of the resonance condition, a RR spectrum is related to the full complex polarizability of a system, rather than the real polarizability of the Raman spectrum. ADF implements the calculation of RR (and hyper-Raman) spectra by evaluating the geometric derivatives of the full complex dynamic polarizability[248–252] as well as a simplified method based on the so-called vertical-gradient Franck–Condon approximation.[251,253]

d. SERS. While useful in and of itself, RR spectroscopy has found tremendous success when combined with techniques that adsorb the target molecule onto a metal nanoparticle, which can produce surface plasmons when they come into resonance with the probing radiation, a technique known as surface-enhanced Raman spectroscopy (SERS).[254,255] The simulation of a SERS spectrum can be achieved in ADF thanks to its modeling of metal nanoparticles through the DIM method,[256–258] which has been coupled with the calculation of complex polarizabilities.[259–261] The FQ method has also been extended to model surface-enhanced response.[262,263]

e. Vibronic coupling. The vibronic structure of absorption or emission spectra at different levels of approximation can also be simulated, allowing one to fully simulate the spectral shape. The Franck–Condon factors (FCF) can be calculated, based on some simplifying assumptions. In particular, the harmonic approximation is employed for the vibrational wavefunction centered at the equilibrium geometry of the ground state and for the vibrational wavefunction centered on the excited state structure. The method used is based on a pre-screening of the FCFs that are expected to be relevant, allowing for a fast and efficient simulation of vibronic absorption or emission spectra.[264,265] A more approximate method that does not rely on the full evaluation of the excited state Hessian is also available, based on a vertical structure tracking algorithm, and works by tracking those modes that are expected to have the largest impact on the vibronic-structure of the spectrum.[266,267]

4. (Hyper)polarizabilities

ADF can also be used to calculate a variety of response properties, including static and dynamic first and second electric polarizabilities, as well as the combined electric and magnetic response polarizability. From the first hyperpolarizability, it is possible to calculate higher-order spectroscopic properties, such as two-photon absorption spectra (TPA).[268] Polarizabilities and hyperpolarizabilities are some of the oldest features that were implemented within the ADF code,[199,269,270] and since then, the range of properties that can be computed has been further expanded. In fact, in addition to these methods, the `AORESPONSE` module in ADF also implements the calculations of polarizabilities $\alpha(\omega)$ as well as first and

second hyperpolarizabilities, including finite-lifetime damping (which can be re-cast as a perturbation with a complex frequency $\tilde{\omega} = \omega + i\Gamma$) to obtain the real and imaginary components of the response tensors.[268,271–272] For hyperpolarizabilities, it is also possible to obtain localized orbital contributions of the tensor elements.[273,274] There is additionally a complex-frequency linear response module that can be used in conjunction with spin–orbit (SO) coupling (i.e., in two-component relativistic calculations).[275] This code can be used, for example, as an alternative to the SO-TDDFT excitation module to obtain broadened absorption and emission intensities from $\mathrm{Im}[\alpha]$, which has advantages in spectral regions with a lot of electronic states.

5. Chiral spectroscopies: ORD, ROA, VCD, and ECD

Response involving certain combinations of electric and magnetic fields gives rise to the most important parameters that govern the natural optical activity of chiral molecules.[276,277] The TDDFT-based formalism has been explored in Refs. 278–280. The dynamic mixed electric–magnetic (e–m) linear response tensor yields the optical rotation of a system. As a function of the frequency ω or wavelength λ of the perturbing field, this property is referred to as optical rotatory dispersion (ORD). ADF can perform standard frequency-dependent response calculations to obtain the ORD off-resonance,[280] which is paired with the corresponding functionality in the TDDFT excitation module to generate the electronic circular dichroism (ECD).[279] ORD and ECD form a pair of Kramers–Kronig (KK) transforms, representing the real part (differential refraction of left- vs right-hand circularly polarized light) and the imaginary part (differential absorption/emission of left- vs right-hand circularly polarized light), respectively, of the complex e–m linear response. ADF contains a separate module dedicated to calculating the mixed e–m response with finite lifetime damping,[281] which simultaneously generates the real and imaginary parts.[282] A formalism for the mixed e–m response using frequency-dependent gauge-including atomic orbitals (GIAOs) to avoid a spurious origin-dependence of the results was also implemented in ADF;[283–285] in this context, it is very important to consider the response of the density fitting coefficients as well in order to achieve full origin invariance. The ECD and ORD can alternatively be calculated with the dipole-velocity gauge, which also ensures origin invariance. We note that the dynamic magnetizability and related properties calculated with GIAOs or in the velocity gauge are also available in ADF.[286]

A number of initial applications of the ECD functionality focused on the origin of the optical activity of chiral metal complexes.[287–289] It was shown, for example, how a combination of angular and axial distortions of the coordinating ligand atoms relative to an idealized octahedral arrangement causes the signs and energetic ordering of the ECD bands in the ligand-field and ligand-to-metal charge transfer regions. Initial calculations with the ORD module focused on the huge optical rotations of [n]helicenes (n = 5–7), among other organic systems.[280] See also Refs. 290 and 291.

The availability of complex finite-lifetime dampened electric and mixed electric–magnetic linear response tensors has enabled the calculation not only of resonance Raman spectra (*vide supra*) but also the Raman optical activity (ROA) under off-resonance and resonance conditions. This has led to the first TDDFT study of resonance-ROA,[260] which confirmed a previous two-state analysis by Nafie showing that the spectrum should become monosignate under resonance.[292] More recent theoretical studies have given a somewhat more nuanced picture, however.[293,294]

The chiroptical counterpart of the electronic emission spectrum is referred to as circularly polarized luminescence (CPL).[295] Of particular interest in this context is the spin-forbidden luminescence with long lifetimes and high dissymmetry factors that can be achieved with chiral metal complexes. A recent article[296] featured two-component relativistic calculations with the SO-TDDFT excitation module of ADF and showed that spin-forbidden ECD and CPL spectra can be generated efficiently and accurately in this manner.

a. Vibrational circular dichroism. Vibrational Circular Dichroism (VCD) is the differential absorption of left and right circularly polarized light during a fundamental vibrational transition. The VCD intensities are proportional to the dot product between the vibrational electric and magnetic dipole transition moments (EDTMs and MDTMs). Using the first order corrections to the Born–Oppenheimer wave function and the harmonic approximation, the Stephens' equations[297] for VCD are obtained. They require the computation of atomic axial tensors (AATs), atomic polar tensors (APTs), and harmonic force fields (HFFs). These quantities are computed by evaluating analytical derivative expressions.[298–302] Namely, the HFFs[301] are found by computing the second derivative of the ground state energy with respect to nuclear displacement vectors, while the APTs[301] and AATs[302] are found by solving the coupled perturbed Kohn–Sham equations for nuclear displacement and magnetic perturbations, respectively. In addition, London atomic orbitals[300,303–305] (i.e., GIAO) are utilized when computing the AATs, to ensure the origin independence of the resulting VCD intensities.

Tests[302,306–314] conducted on numerous chiral compounds have shown that the BP86 XC-functional in combination with the TZP basis set consistently yields good agreement between the experimental and computed VCD spectra at a reasonable computational cost. This allows one to accurately assign the absolute configuration (AC) of solvated chiral compounds by simply comparing their experimental and simulated VCD spectra. While very successful, this AC assignment protocol is a black-box procedure that does not offer much (if any) physical insight. This is because the interpretation of the sign and magnitude of the VCD bands is not straightforward and cannot be inferred by only visualizing the normal mode motion and the associated nuclear displacement vectors. To gain physical insight, the relative orientations and magnitudes of the EDTMs and MDTMs must be carefully analyzed—a complicated task given their large number and the inherent origin-dependence and imaginary nature of the MDTMs.[315,316] To aid such an investigation, the AMSspectra graphical user interface is augmented with the VCDtools analysis program.[317,318] Using VCDtools, the nuclear displacement vectors and atomic EDTMs (or MDTMs) can be visualized simultaneously, either as arrows or by scaling the radius of each atom based on the magnitude of its chosen atomic vector. This facilitates the identification of the VCD-active and VCD-inactive sites of a molecule, thereby enabling a general coupled-oscillator (GCO) decomposition[313,319,320] of the VCD intensity. The GCO-VCD analysis offers a straightforward and intuitive interpretation of the VCD phenomenon, conceptualizing it as the interaction

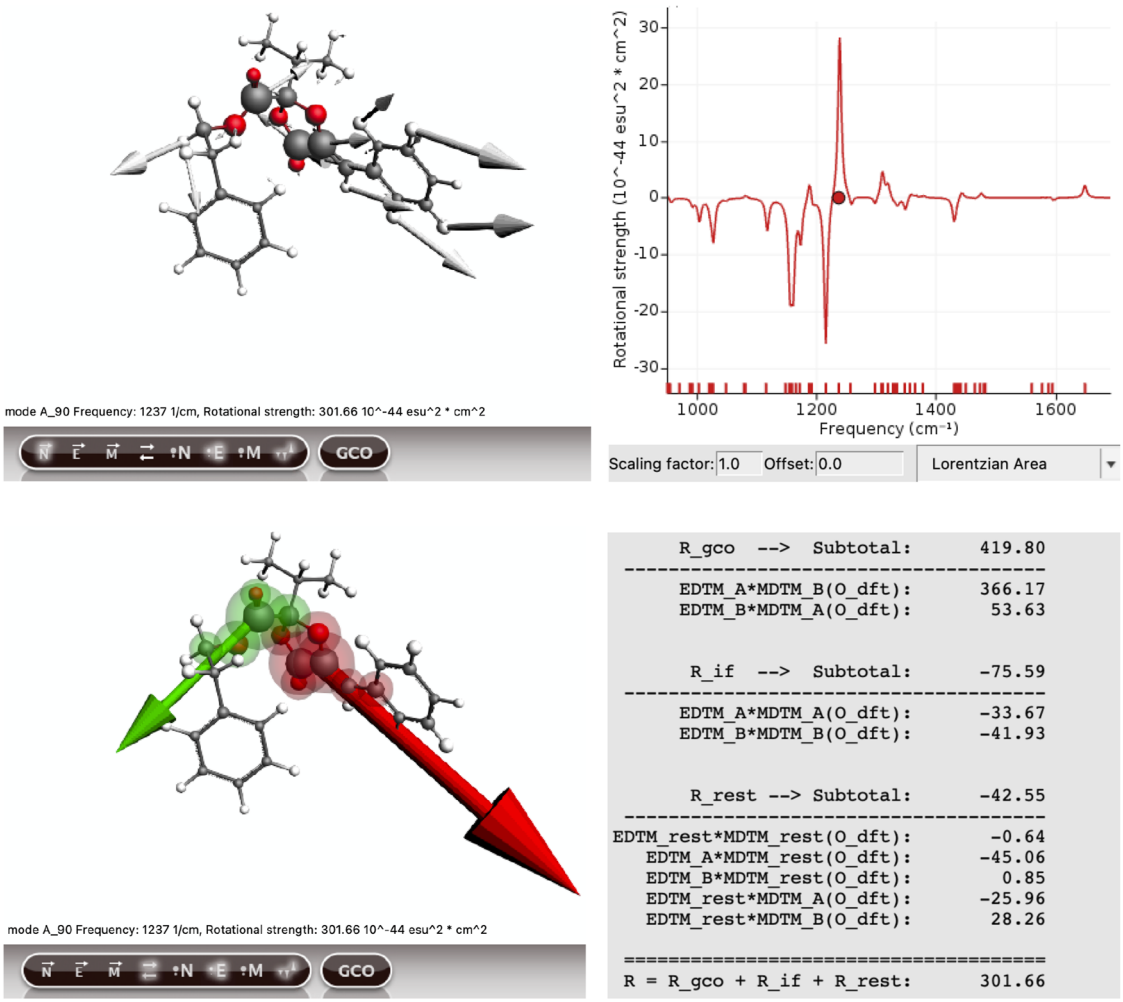

FIG. 5. AMSspectra/VCDtools GUI. Upper panel: The computed VCD spectrum is shown on the right side. The red dot at 1237 cm^{-1} highlights the VCD band chosen for analysis. The left panel shows the molecular structure of the considered guignardianone conformer. The nuclear displacement vectors of the selected mode are represented by arrows, while the radius of the atoms has been scaled based on the magnitude of their atomic EDTMs. Lower panel: GCO analysis of the selected mode. On the left side, the atoms with large EDTMs have been assigned to the two GCO fragments (highlighted in red and green) and the EDTMs associated with these two fragments are shown as the red and green vectors. The right panel shows the decomposition of the VCD intensity into the dominant GCO component (associated with the interaction of the GCO fragments) and the small contributions determined by the individual (non-interacting) fragments.

of two electric dipoles through space. Figure 5 illustrates the analysis of a band in the VCD spectrum of guignardianone using VCDtools.

An even more useful tool is the GA-HC analysis.[312,314] To replicate the VCD experimental spectra of flexible molecules, which often exhibit numerous conformers at room temperature, Boltzmann averaging of the spectra computed for low-energy conformers is essential. The resulting simulated spectra are, therefore, highly dependent on the DFT Boltzmann factors, which are known to have large uncertainties. Using the GA-HC option, the identification of conformers present in the experimental sample is done automatically. By combining a genetic algorithm (GA) with hierarchical clustering (HC) analysis, the GA-HC protocol effectively circumvents the need to rely on the inaccurate Boltzmann populations predicted with DFT. Besides enhancing the effectiveness of the VCD technique, this procedure is also able to identify the situations when reliable predictions may not be feasible. Furthermore, the GA-HC protocol can also be used to analyze ECD and ROA spectra (see Fig. 6).

6. Magnetic field-induced optical activity

Optical rotation via the interaction of light with non-chiral compounds can be induced with a static magnetic field that is applied in the direction of the light propagation—this effect was originally discovered by Faraday and is now known as magneto-optical rotation (MOR). MOR is the real (dispersive) part of a complex electric–electric–magnetic quadratic response function; the imaginary part (the KK-transform of the real part) is the magnetic field-induced circular dichroism (MCD). Both can be calculated

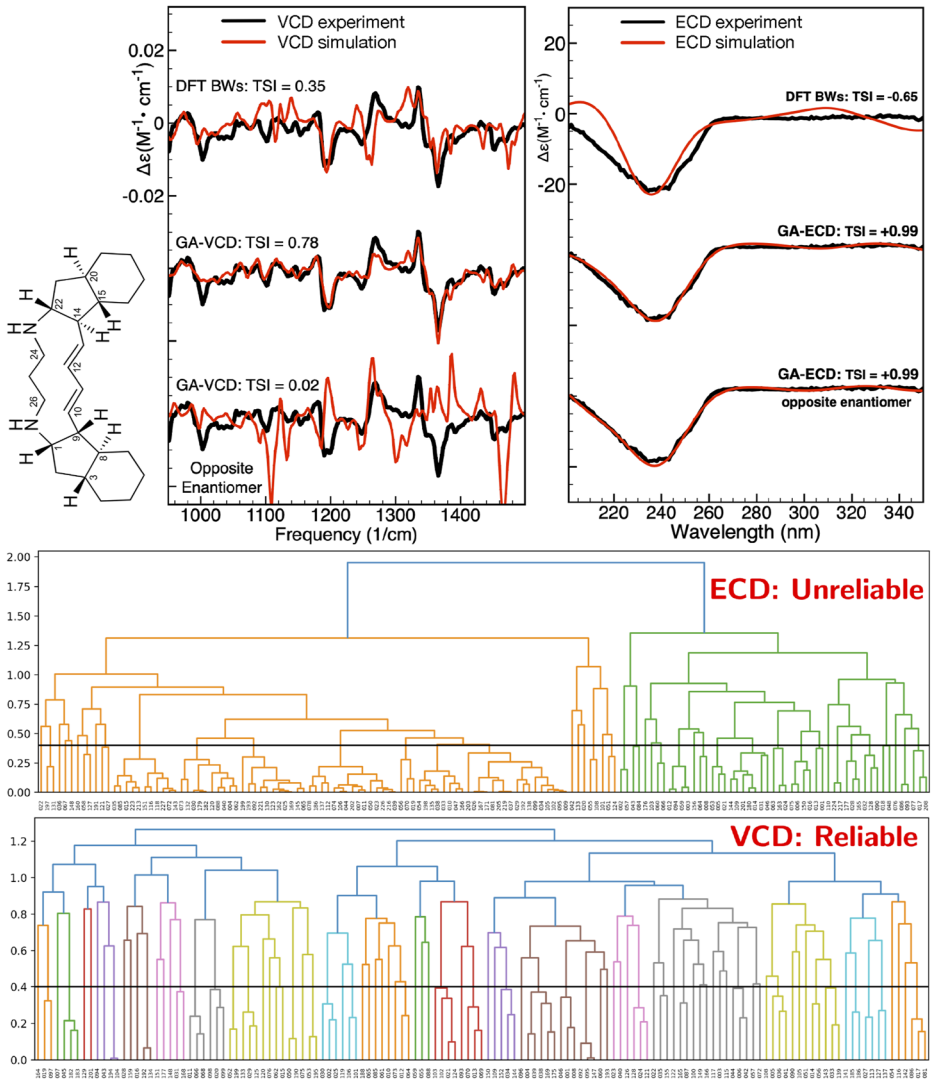

FIG. 6. Application of the GA-HC protocol to the VCD and ECD spectra of haliclonadiamine.[314] Upper panel: Simulation of the experimental VCD (left) and ECD (right) spectra using the genetic algorithm. Lower panel: Hierarchical clustering analysis of the ECD and VCD spectra computed for the low energy conformers of haliclonadiamine.

with ADF and TDDFT response methodology; the underlying theory, the implementations of the various contributions, and a variety of applications were described in Refs. 321–329.

7. NMR and ESR

Spectroscopic techniques related to the magnetic and quadrupolar interactions between the electrons and nuclei feature prominently in AMS. ADF can be used to compute the nuclear magnetic shielding σ,[330–335] the indirect (electron-mediated) nuclear spin–spin coupling (J-coupling),[336–338] and electric field gradient (EFG) tensors[339] underlying the quadrupolar interactions. SO interactions are treated variationally. The chemical shift in reference to the same isotope in a different environment is given by $\delta = (\sigma^{\mathrm{ref}} - \sigma)/(1 - \sigma^{\mathrm{ref}}) \simeq \sigma^{\mathrm{ref}} - \sigma$. The approximate version is almost always used because shielding constants are on the order of 0.01 (10^4 ppm) or less. In a nutshell, the chemical shift δ determines the location of the signal in the spectrum, J-coupling gives the splitting of signals due to the magnetic interactions between the nuclei, and for solid-state NMR of quadrupolar nuclei, the EFG tensor is of paramount importance for the width and shape of the signals in solid-state NMR. The paramagnetism of systems with unpaired electrons and the magnetic interactions between unpaired electrons and nuclear spins give rise to the main parameters of electron paramagnetic resonance (EPR) spectroscopy. The ADF developments are described in Refs. 340–346 and feature spin-unrestricted and quasi-restricted open-shell DFT approaches with the perturbational or variational treatment of SO effects. The electron g-factors parameterize the magnetic moment of the electronic system and determine the spectral location of the EPR signal. The hyperfine coupling A parameterizes the magnetic electron spin–nuclear spin interactions and determines the splitting of signals. For electronic states with spin >1/2, there is also the zero-field splitting (ZFS),[347–351] which parameterizes the magnetic interactions among the electrons. ZFS tensors can also be calculated

with ADF. Note that NMR and EPR are not the only spectroscopic techniques that probe the various aforementioned interactions.[352]

The ADF NMR and EPR modules are based on the ZORA Hamiltonian and use GIAO basis functions for NMR shielding and g-factors to avoid a spurious origin-dependence of the results. (For the hyperfine interaction with a given nuclide, the natural choice of the field-gauge origin is the nucleus.) The ADF NMR codes were among the first to feature general-purpose all-electron relativistic DFT capabilities, and therefore, many pioneering studies were undertaken with them. An advantage of ZORA vs other quasi-relativistic Hamiltonians is the relative simplicity of including magnetic perturbations at the operator level. Over the years, a number of benchmarks have been aimed at discerning the accuracy of the ZORA Hamiltonian for shielding and J-coupling.[335,353–358] It is known that ZORA accurately describes the relativistic effects in the valence shells of heavy atoms, but it affords large errors for the core shells. This would seem to imply that NMR parameters calculated with ZORA have large errors, but in practice, this is only the case for the absolute shielding σ.[335] The core–shell errors almost all cancel in the chemical shift, leaving the valence-shell relativistic effects to dominate the results. J-coupling has been shown to be dominated by the valence and outer core shells,[336] and therefore, ZORA performs accurately as well. In the cited references, explicit comparisons with four-component relativistic calculations demonstrated the accuracy of ZORA for NMR shifts and J-coupling. Similarly, the valence and outer core shell hyperfine integrals that determine the EPR hyperfine coupling are accurately described by ZORA.[353] EPR g-factors are dominated by the valence shells and also not a concern regarding the approximations in ZORA. The EFG is an electric perturbation and subject to picture-change effects. This refers to the different operator forms a physical quantity like the position can possess upon a change of picture. In this case, the four-component Dirac equation has to be transformed, as originally argued by Foldy and Wouthuysen,[359] to a picture where the large and small components are decoupled so that the two-component nonrelativistic limit can be obtained, yielding the Schrödinger equation plus perturbations: $\boldsymbol{r}$ in the Schrödinger picture of the Schrödinger equation is associated with a different quantity (the "mean position") than the operator $\boldsymbol{r}$ in the Dirac picture of the Dirac equation.[360,361] Van Lenthe and Baerends introduced the ZORA-4 approximation by which the four-component density is restored within the ZORA approximation.[339] Extensive benchmarks, also via implementations in other codes,[362,363] indicated good performance of ZORA-4, although perhaps not as good as ZORA for magnetic properties.

Pioneering applications of the ZORA NMR codes include studies of large solvent effects on these parameters in metal complexes.[332,364] A ^{199}Hg–^{199}Hg J-coupling of enormous magnitude, 284 kHz, was reported experimentally[365] for $[Hg_2]^{2+}$ complexated by crown ethers. ADF calculations[366] gave near-quantitative agreement with the experiment (non-hybrid DFT) and demonstrated that the crown ether ligands, in fact, lowered the J-coupling a lot relative to the free ion (predicted to have a coupling of ~0.9 MHz). A later study showed that finite nucleus effects reduced the coupling by almost 19%, but the use of a hybrid functional led to an increase, thus restoring the agreement with the experiment.[190] The prediction of an unusual ^{13}C shift (240 ppm) along with a small but significant ^{13}C–^{103}Rh J-coupling (27 Hz) by ADF DFT calculations aided the experimental observation of the NMR signal of a short-lived carbenoid di-Rh species that had been postulated but not detected for nearly 6 decades.[367]

ADF also features a set of analysis tools for NMR shielding, J-coupling, and EFG tensors in terms of natural bond orbitals (NBOs) and natural localized molecular orbitals (NLMOs) as generated by the NBO algorithms.[368] In particular, NMR shielding and J-coupling can be analyzed via scalar relativistic NLMOs/NBOs both in SO and in scalar ZORA calculations,[369–371] and EFG tensor analyses are presently available for scalar ZORA-4.[372] These analysis tools are in widespread use, as outlined in a recent article,[373] as they are able to deliver an intuitive breakdown of the tensor components in terms of "chemist's orbitals," i.e., core shell, lone pair, bonding, and more diffuse localized orthonormal orbitals. A recent application has focused on ^{103}Rh shielding tensors in complexes.[374] Earlier work by one of us demonstrated the unintuitive origin of substituent effects on aromatic ^{13}C NMR shifts,[375] which is featured in one of the tutorials available on the SCM website.[376] Finally, ADF also implements the calculation of Nucleus-Independent Chemical Shifts (NICS), which have also proven to be a powerful tool for the study of aromaticity.[377]

IV. QM ENGINES: PERIODIC SYSTEMS

A. BAND

1. Design

BAND is an AMS engine especially developed for periodic calculations, although it may be used for systems with any type of periodicity, including isolated molecules (0D), surfaces (2D), and crystals (3D).[17] It has been developed primarily to enable periodic calculations with the same "technology" as ADF: numerical integration,[29,31] atom centered basis functions (STOs and NAOs), and density fitting for accurate potentials.[17,37] This allows a seamless transition from (increasingly large) finite systems (e.g., metal clusters and impurities with increasing but finite "bulk environment") to the infinite periodic system.[378]

The atom centered basis set affords very similar analysis methods as are available in ADF. The fragment approach offers meaningful partial density of states based on fragment orbital gross populations and overlap populations (COOP).[379] Recent applications of band range from the prediction of superconductivity,[380] bandgap control,[381,382] battery research,[383] magnetocaloric effect,[384] electronegativity,[385] gas sensors,[386] to optical spectra.[387,388] Numerous analysis tools are available, which are integrated with the Graphical User Interface (GUI). Similar to ADF, BAND offers an energy decomposition analysis, taking, for instance, as fragments a metal slab and an adsorbing molecule.[389–402] There is the additional possibility, not present in the non-periodic electronic structure modules, of confining the basis functions to speed up the calculation by altering the radial part of the basis functions in order to make them more compact, which also avoids linear dependency problems that can arise specifically in periodic calculations. An important technical aspect that is specific to BAND is k-space sampling (i.e., the k-points used to sample the Brillouin zone), as it heavily influences the accuracy, the CPU time, and the memory usage of the calculation. The quadratic tetrahedron method[403,404] has excellent convergence characteristics.

2. Electronic structure options

For its calculations, BAND uses Density Functional Theory (DFT) in the Kohn–Sham approach, with LDA, GGA, meta-GGA, and range-separated hybrid functionals. To this end, the density matrix as calculated on the k-grid is Fourier transformed to real space, from which the real space exchange matrix follows,[405]

$$K_{ij}^{\vec{A}} = -\frac{1}{2}\sum_{\vec{C}\vec{D}}\sum_{lm} P_{lm}^{\vec{D}-\vec{C}}(\chi_i^0\chi_l^{\vec{C}}|\chi_m^{\vec{D}}\chi_j^{\vec{A}}), \tag{26}$$

where $\vec{A}$, $\vec{C}$, and $\vec{D}$ are cell indices. The real space cell dependent Hartree–Fock exchange matrix is calculated using PADF as described in Sec. III A 5. This is then transformed back to reciprocal space to obtain the exchange matrix in the k-points.

Scalar relativistic and spin–orbit effects can be included in the calculation through the ZORA scheme (see Sec. III E), in both the ground and excited states.[18,406,407] Continuum embedding schemes such as COSMO and SM12 (Sec. VI) are also shared between ADF and BAND for a seamless use across different engines.

There is also the option to add an empirical dispersion correction.[64,65]

3. Periodic calculations

The primary use of BAND is, of course, as a fully fledged code for periodic systems. It is one of the periodic codes that is based on the LCAO formalism instead of a plane wave basis. It does not use pseudopotentials. It is possible but not necessary to use frozen cores; all-electron calculations can be done just as well. Properties that are sensitive to core electron behavior, or to features of the density close to the nucleus (electric field gradients and spin–orbit coupling), are just as accurate as in the molecular ADF code. A difference with ADF is that BAND offers numerical atomic orbitals (NAOs). These are, in fact, used as a standard basis set, which can be augmented with STOs, from single-zeta to quadruple-zeta quality. In addition, basis sets of exclusively one or the other type are possible, and even Gaussian basis functions can be used (by casting them in the form of NAOs). The latter proved to be useful for testing correlation methods such as MP2 and RPA with literature data that had been obtained with Gaussian basis sets for molecules.[35] Here, the BAND program was applied to nonperiodic systems.

4. Properties

Besides the modeling of the structure and energetics of periodic systems, BAND offers the possibility of modeling numerous properties of such systems as well. Some types of calculations are specific for periodic systems. These include spectroscopic properties, both electronic (dependent on the band structure) and vibrational (including the modeling of phonons), which are described in more detail below, as well as mechanical properties of the material, such as the stress tensor and the elastic tensor **c** defined as the derivative of the energy E with respect to a generic strain deformation $\boldsymbol{\epsilon}$,

$$c_{\alpha,\beta} = \frac{1}{V}\frac{\partial^2 E}{\partial\epsilon_\alpha\partial\epsilon_\beta}, \tag{27}$$

where V is the volume of the unit cell for systems of periodicity 3, or the area or length for systems of periodicity 2 and 1, respectively. In BAND, these derivatives are evaluated using a numerical scheme, for each strain deformation. Computing the elastic tensor will also calculate the bulk modulus, Young's modulus, and shear modulus, as well as the Poisson ratio. The elastic tensor and moduli are not calculated by BAND directly, but rather they are assembled by the AMS driver using the data that BAND provides. Because of this, it is also possible to evaluate them within AMS by invoking any other engine that supports periodic boundary conditions.

In a semiconductor, the mobility of electrons and holes is related to the curvature of the bands at the top of the valence band and the bottom of the conduction band. BAND allows us to simulate this curvature, which is obtained by numerical differentiation.

Some techniques have been implemented specifically for periodic systems, as is the case for electron energy loss function spectroscopy (EELS), which can be calculated from the macroscopic dielectric function and is implemented in BAND.[408–411]

5. Electronic transport with nonequilibrium Green's functions (NEGF) in BAND, ADF, and DFTB

The QM engines in AMS can be used to simulate a number of charge transport properties for various types of system, including complex devices; see Sec. III D. Charge transport in multilayer devices with 2D periodicity, having a varied chemical nature, can be accurately modeled using BAND in a fully self-consistent NEGF treatment. Transport through single molecules between electrodes can be handled with an extension of the ADF code. Both implementations allow a varying degree of sophistication.[412]

In the case of nano-scale devices, specific methods are needed to tackle the modeling of systems composed of layers with a varied chemical nature while allowing for an accurate modeling of the electronic transport between them. The Non-Equilibrium Green's Functions formalism (NEGF) implemented in BAND (as well as ADF and DFTB) is especially useful for this purpose. NEGF is a formalism for solving the many-body Schrödinger equation of a non-equilibrium system coupled to semi-infinite electrodes, where electron transport is treated as a one-dimensional coherent scattering process in the "scattering region" for electrons coming from the electrodes.[413,414] The method itself is quite general and can be applied to a variety of practical systems. As examples, AMS offers tutorials on simulating electronic transport in a carbon nanotube or in a 1D gold chain, studying spin transport in chromium wires, and transport in a molecular junction between gold electrodes, among others.

B. Quantum ESPRESSO interface

In addition to BAND, we have also implemented an interface to the Quantum ESPRESSO (QE) program[415–417] within AMS, allowing a user to employ it as one of its engines for periodic calculations. AMS driver can obtain, for example, atomic forces from Quantum ESPRESSO to update the atomic positions in geometry optimizations, molecular dynamics, nudged elastic band, PES scans, or any of the other AMS driver tasks. The output is given in the normal AMS format, which means that it can natively be used with PLAMS and ParAMS.

V. QM ENGINES: SEMIEMPIRICAL METHODS

AMS is interfaced with two distinct semiempirical engines, i.e., DFTB (Sec. V A) and MOPAC (Sec. V B). These packages offer

a very cost-effective alternative to the more expensive *ab initio* approaches of ADF and BAND and are, therefore, suitable to be applied to the study of significantly larger systems. ADF also features an implementation of the ligand-field DFT method, which is especially suitable for complexes of *d* and *f* block elements; see Sec. V C. Multiscale methods typically employ more approximate, semiempirical, methods to describe an environment in which a central system is embedded for which a more complete quantum mechanical description is applied; see Sec. 6.

A. DFTB

The DFTB engine supports two different classes of model Hamiltonians, Grimme's extended tight-binding,[418,419] and the classic Slater–Koster based DFTB.[418,420,421] All these model Hamiltonians are obtained by applying tight-binding approximations to the DFT total energy expression. DFTB also benefits from all k-space sampling and numerical integration of BAND.

1. Slater–Koster based DFTB

The efficiency of Slater–Koster based DFTB stems from its use of an optimized minimum valence orbital basis that reduces the linear algebra operations and a two center approximation for the Kohn–Sham potential that allows precalculation and storage of integrals using the Slater–Koster tables.[418,420–422] This makes DFTB orders of magnitude faster than DFT but requires parameter files (containing the integrals) for all pairwise combinations of atoms in a molecule. Many elements can be handled with the parameter sets included in the distribution. There are three flavors of Slater–Koster based DFTB available: the "plain" DFTB Hamiltonian as introduced by Porezag and Seifert[420] without a self-consistency cycle, and the second order self-consistent charge extension SCC-DFTB (recently also called DFTB2),[421] which accounts for density fluctuations and improves results on polar bonds. Note that the self-consistent calculations are about an order of magnitude slower than calculations with the "plain" DFTB Hamiltonian. Finally, there is the third order extension known as DFTB3,[422] which improves the description of hydrogen-bonded complexes and proton affinities. DFTB3 calculations are only marginally slower than SCC-DFTB based calculations.

2. Extended tight-binding

The extended tight-binding (xTB) model Hamiltonian has recently been introduced by Grimme and co-workers.[419] It makes similar approximations as Slater–Koster based DFTB, but instead of using precalculated integrals, xTB employs a (small) basis of Slater-type orbitals and uses an extended Hückel-like approximation for the Hamiltonian. The DFTB engine supports the GFN1-xTB parameterization,[423] which is optimized for geometries, frequencies, and non-covalent interactions and covers all elements of the Periodic Table up to radon.

In addition to the calculation tasks that are common to all QM engines such as geometry optimizations, DFTB can be easily used to perform transport calculations. Electron transport can be modeled using the non-self-consistent NEGF formalism available in BAND (and ADF); see Sec. 4.

B. MOPAC

The Molecular Orbital PACkage (MOPAC) is a general-purpose semiempirical quantum chemistry engine for the study of molecular and periodic structures based on Dewar and Thiel's NDDO approximation.[424,425] MOPAC supports several types of calculations, including linear transit and PES scan, constrained geometry optimizations, molecular dynamics simulations, lattice optimization (also under pressure), elastic tensor and related properties (e.g., bulk modulus), phonon calculations, and more.

C. Ligand field DFT

It is well known that common DFT approaches have difficulties modeling systems containing transition metals and f-block elements. These systems may often be characterized by a complex electronic structure with closely lying energy levels, multi-reference character, and non-negligible relativistic effects. Ligand-Field DFT (LFDFT) is a semiempirical model with adjustable parameters that offers a cost-effective way to model specifically metal complexes of both d and f block elements.[426,427]

The key feature of the LFDFT approach is the explicit treatment of near degeneracy correlation using an *ad hoc* Configuration Interaction (CI) expansion within the active space of Kohn–Sham (KS) orbitals with dominant p-, d-, or f-character. The calculation of the CI-matrices is based on a symmetry decomposition in the full rotation group of the particular complex under investigation as well as on a ligand field analysis of the energies of all DFT single determinants (also known as micro-states) for frozen KS-orbitals corresponding to the averaged configuration, possibly with fractional occupations, of the p-, d- or f-orbitals.

Thus, LF theory considers active p-, d-, and/or f-electrons moving in the potential of a passive chemical environment generating the ligand field. The LFDFT model is also available extended for open-shell systems,[427] which is particularly relevant for inter-shell transitions in lanthanides, which are crucial for understanding the optical and magnetic properties of rare-earth materials.

VI. EMBEDDING

A. General

Embedding methods allow us to significantly save on computational time by partitioning a complex system into simpler, smaller parts, which may be treated at different levels of theory.[22,428–435] In cases where a system can be partitioned into a central moiety embedded within a certain environment, one useful classification looks at the types of interactions that are allowed between the two layers. Within a mechanical embedding scheme, only mechanical forces acting between the two layers are considered. This means that the geometry and, in general, the forces acting on the atoms are altered by the presence of the environment, but the QM density of the system is otherwise unaffected. This is a rather crude approximation because all electronic properties are then computed as if the system were isolated. A more refined approach is known as electrostatic embedding, in which the environment is endowed with a fixed charge density (e.g., static charges on the environment's atoms), which then acts on the QM system through a one-electron electrostatic interaction that is added to the Hamiltonian. The QM

density is, therefore, directly affected by the presence of the environment. Finally, we have polarizable embedding schemes in which the properties in the environment are directly affected by the QM density of the system. The electrostatic contributions of the environment, therefore, are dynamically calculated at the same time as the QM density until self-consistency is reached. Within AMS, all these three levels of embedding are included, with a choice of different methods for each, allowing for a great amount of flexibility for the user, and are here summarized. Note that in AMS, the subdivision of a system is totally flexible and does not necessarily have to adhere to a shell model where the lower level of theory is used for the environment wherein a smaller system is embedded; in fact, different parts of a system can be treated with different models that can be freely chosen by the user.

B. The hybrid engine

The coupling between quantum-mechanical and classical is easily achieved using the special-purpose hybrid engine, a tool designed to easily combine different engines within the AMS package and produce a more sophisticated description of a system. The interface is like that of any other AMS engine, with a range of settings as an input, and a potential energy surface, gradients, or other molecular properties as the main output. As such, the hybrid engine can be used in any AMS application, such as geometry optimization or molecular dynamics. The hybrid engine can be used for a wide range of multi-scale simulations, involving many different layers of the system and many different levels of accuracy. The hybrid engine can also handle cases where the boundary between the regions cuts through covalent bonds by assigning link atoms to satisfy the valence of the boundary atoms according to the AddRemove methodology.[436] By default, the engine adds hydrogen as a capping atom, although a different element can be selected by the user.

C. QM/MM

The most commonly used multi-scale setup is a combined quantum mechanical/molecular mechanical (QM/MM) scheme. Such a QM/MM scheme divides the system into two different regions: (i) a QM region that is described by a QM engine, such as ADF or DFTB, and (ii) an MM region that is described by an MM engine, such as the forcefield engine. Within the QM/MM definition, the user can choose between mechanical embedding and electrostatic embedding, and the choice determines which sub-options and which sub-engines are available, and in fact, almost any combination of methods is possible (QM/QM′, MM/MM′, MM/QM, where different QM engines may be combined, like ADF and DFTB for instance, or also different MM layers as well, which is indicated with MM/MM'). The resulting calculations may fall under either the mechanical embedding or electrostatic embedding regimes, depending on the user's choice of method.

D. Continuum models

Polarizable embedding methods can also be used within the QM engine specifically, and two of them in particular are available in AMS. The first and simplest is the conductor screening model (COSMO), in which the QM system sits within a cavity carved in a conductor material.[437] The QM density induces charges upon the surface of the cavity, and the interaction between the two layers is scaled by a function, which depends on a dielectric constant, in order to simulate the presence of a dielectric medium.[438] This model is particularly appropriate to model polar environments such as aqueous solutions, provided that other types of interactions, such as hydrogen bonds, can be neglected. Another continuum model implemented in AMS is the Minnesota's Solvation Model 12 (SM12).[439] SM12 makes use of the generalized Born approximation to calculate the bulk electrostatic contribution, based on a representation of the solute as a system of point charges located at the nuclear positions.[440] The SM12 model in ADF uses charge model 5 (CM5) charges.[441] CM5 is a class 4 charge model, making use of both empirical and density related terms. It is comprised of Hirshfeld charges, a simple bond order calculation, atomic distances, and atom specific parameters. The advantage of continuum models is that they slash the computational cost of treating a solution by completely smearing the solvent, thereby removing its atomistic description while keeping the most salient interactions, which for polar solvents are electrostatic. Another significant advantage of the continuum models is that by foregoing the atomistic description of the environment, one does not need one to sample the configurational space of the solute–solvent couple, and the structure of the solute alone is sufficient for the description.

E. Atomistic models

Atomistic models must be preceded by an appropriate sampling of the molecule-environment configurational space, either through a molecular dynamics simulation or some other method, depending on the specificities of the system. AMS implements two atomistic polarizable embedding methods. The first is the discrete interaction model (DIM), which can model any type of atomistic environment, from simple solvents to metal nanoparticles (see Fig. 7).[258] DIM/QM relies on one of three descriptions of the system: Discrete Reaction Field (DRF),[256,442–445] where the atoms interact via induced dipoles and static charge, Capacitance Polarizability Interaction Model (CPIM),[257] where the atoms interact via induced dipoles and induced charges, and Polarizability Interaction Model (PIM), where the atoms interact via induced dipoles only. DRF is best for solvents, CPIM is best for small metal nanoparticles, and

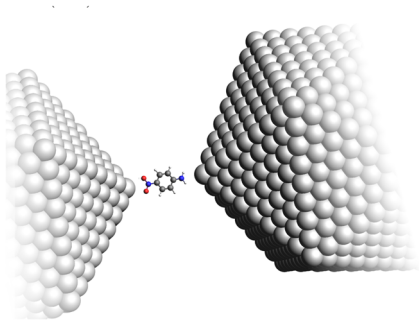

FIG. 7. para-Nitroaniline (pNA) in the junction between two Ag_{2057} clusters. The enhancement in the optical response properties of the pNA molecule under the influence of the silver clusters can be modeled in ADF using the DIM/QM method, where pNA is treated using DFT, while the metal is described using DIM.[454].

PIM is best for large metal nanoparticles. The DRF model in its own right is a hybrid Quantum Mechanical and Molecular Mechanics (QM/MM) model that is particularly suitable for studying solvation effects on (time-dependent) molecular properties such as dipole moments, excitation energies, and (hyper)polarizabilities. The classical solvent molecules are represented using distributed atomic charges and polarizabilities. The QM/MM interaction is split into an electrostatic and a polarization term, where the former term is the electrostatic operator and describes the Coulombic interaction between the QM system and the permanent charge distribution of the solvent molecules and the latter is the polarization operator and describes the many-body polarization of the solvent molecules, i.e., the change in the charge distribution of the solvent molecules due to interaction with the QM part and other solvent molecules. The charge distribution of the solvent is represented by atomic point charges and the many-body polarization by induced atomic dipoles at the solvent molecules. In order to perform a DRF calculation, two types of parameters (model atomic charges and atomic polarizabilities) for each type of atom in the MM part are required. The point charges should represent at least the permanent molecular dipole moment, and the distributed atomic polarizabilities should represent the full molecular polarizability tensor. The second QM/MM polarizable embedding method implemented in AMS is the fluctuating charge (FQ) model, also available in the more refined fluctuating charges and dipoles (FQFμ) version.[446] In this case, each MM atom is endowed with a charge (and possibly also a dipole) that can fluctuate in response to the electrostatic potential of the QM system. The charges and dipoles then affect the QM system through electrostatic interaction terms that are added into the Hamiltonian, and the whole system is solved self-consistently. The FQ(Fμ) model can be used both in fully *ab initio* calculations in ADF and in semiempirical calculations with the DFTB engine[447] and is particularly useful for the modeling of aqueous solutions since it can properly account for the directionality of hydrogen bonds[435,448] and has been developed with the specific aim of being able to model environmental effects upon spectroscopic observables[449] and as such has been extended to cover most spectroscopic response properties within AMS.[450–453]

The model has also been extended to the treatment of plasmonic phenomena in systems such as metal nanoparticles and graphene by allowing the fluctuating charges and dipoles to be complex. The method has been used to study enhanced spectroscopies such as SERS and surface-enhanced fluorescence (SEF).[262,263]

F. 3D-RISM

An intermediate method between the ones presented so far is the three-dimensional reference interaction site model (3D-RISM),[455] which combines a quantum chemical method for the solute with statistical mechanics description of molecular solvation based on density distribution functions. This method enables the calculations of thermodynamics, electronic properties, and molecular solvation structure of a solute molecule in a given molecular liquid or mixture at a modest computational cost. Using 3D-RISM, one can study chemical reactions, including reaction coordinates and transition state search, with the molecular solvation described from first principles based on a molecular-mechanics type description of the solvent. The method yields all the features available by using other solvation approaches.

G. Frozen density embedding

Finally, ADF also implements the Frozen Density Embedding (FDE) scheme for this purpose.[456,457] FDE is a quantum embedding method that divides a system by partitioning the total electronic density into two or more subsystems, which can be separate molecules, a molecule in a more complex environment, or any other type of division.[458,459] The density of the system is the sum of the subsystem densities, which may overlap and are constrained to integrate to the appropriate number of electrons. The FDE method works by keeping one part frozen, while the total energy is variationally optimized with respect to the other, although these roles may be switched between the two to reach an overall self-consistency if necessary. In this case, the method is often referred to as subsystem DFT (sDFT) and can be regarded as a first-principles alternative to Kohn–Sham DFT.[460,461] The FDE implementation in AMS[457] allows for the calculation of the energetics,[462] structure,[463] and bonding of complex systems, as well as electronic,[464–466] ESR,[467] and NMR spectra,[468,469] and can also be combined with the FQ method to obtain a three-layer description for complex systems.[451,470] For aggregates of coupled chromophores or other assemblies of molecules with coupled response, a subsystem version of TDDFT/TDA is also available.[471–474] It can be employed for calculations of UV–Vis absorption and circular dichroism spectra of exciton-coupled dyes as well as of optical rotatory dispersion and frequency-dependent polarizabilities. FDE can also be used to construct quasi-diabatic, charge-localized, and/or spin-localized electronic states. This allows us to extract electronic couplings for charge-transfer processes within the FDE-ET method[475,476] and to compute spin densities for radical cations/anions of molecular dimers with the FDE-diab method.[477]

VII. CLASSICAL ENGINES

To allow fast and approximate simulations of molecular systems, AMS provides classical force field engines that describe molecular systems using purely classical equations. The available force fields can be grouped into non-reactive force fields, reactive force fields, and machine learning potentials (MLPs).

A. Non-reactive force fields

The non-reactive force fields all have the same basic expression for the energy, which contains a bond stretching term (E_b), an angle bending term (E_a), a torsion angle rotation term (E_t), an improper angle bending term (E_{imp}), a van der Waals interaction term (E_{vdW}), and an electrostatic interaction term (E_e),

$$E = E_b + E_a + E_t + E_{imp} + E_{vdW} + E_e. \tag{28}$$

The most important difference between force fields lies in the parameters and functional forms for each individual energy contribution. In classical force field simulations, all atoms in the system are assigned atom types, and these atom types and their combinations (into pairs for bonds, triplets for angles, etc.) correspond to specific parameters, which are stored in parameter files. AMS has several parameter files available, but it is also possible for the user to provide a custom parameter file.

To the user, the most apparent difference between the available force fields lies in the usability. For some (UFF,[478] GFN-FF,[479] GAFF,[480] and APPLE & P[481]), the assignment of atom types is automatic, or even guaranteed to work for any system (UFF and GFN-FF). For others (AMBER[482] and TRIPOS[483]), atom-types have to be provided by the user for some or for all systems. The latter approach is in line with other classical molecular simulation software applications such as LAMMPS,[484] AMBER,[482] CHARMM,[485] NAMD,[486] and GROMACS.[487]

1. Automatically typed force fields

The UFF[478] force field has been around for many years and uses the same or similar simple expressions for the energy contributions as main stream force fields such as AMBER and CHARMM. The electrostatic energy contributes very little to the total energy in this force field, with an electrostatic energy interaction of zero for most systems. Water is the only exception, with electrostatics described as a simple Coulomb interaction between atoms with fixed charges.

GFN-FF[479] is a fairly recent addition to the force field family. It is a partially polarizable force field that uses a charge equilibration scheme to reassign atomic charges at each new geometry. All other interaction terms are more complex than traditional force field energy terms as well, while the number of GFN-FF parameters per element is relatively small. From a user perspective, applying UFF and GFN-FF is extremely simple since parameter setup is automatic and the user does not need to provide them manually, and successful parameter generation is all but guaranteed.

GAFF[480] is an AMBER-developed force field, parameterized for small organic molecules. It only contains atom types for main group elements. The energy expressions share their bond, van der Waals, and electrostatic energy terms with the AMBER force field, but the contribution of the electrostatic energy is much more significant. The force field is well established and can generally be relied upon to give reasonable results for its target systems. An atom-typing tool can be activated at runtime with a keyword in the AMS engine block. The tool uses the AMBER Antechamber software[488] under the hood. One of the limitations of Antechamber for GAFF is that it fails for periodic materials in chain, slab, or bulk form.

APPLE & P[481] is a polarizable force field that computes atomic dipole moments from atomic polarizabilities and then includes charge–dipole and dipole–dipole interactions in the electrostatic energy term. This improved description of electrostatics over the other available force fields makes APPLE & P the preferred choice for systems with charged species. AMS comes with a tool for automatic APPLE & P atom-typing, which lets APPLE & P easily be used for many solvents, solutes, and polymers. A drawback of the APPLE & P force field is that it has been parameterized using fixed bond lengths, and therefore, APPLE & P simulations require the bond lengths to be constrained to (approximately) equilibrium bond distances of the system.

2. User-typed force fields

The AMBER force field[482] is parameterized for biomolecules only. The energy expressions are the same as those for the GAFF force field. Like GAFF, it is well-established and generally reliable. While users are mainly expected to supply the atom-types themselves, AMS does offer limited atom-typing capability with the AMS pdb2adf utility program[489] that requires a PDB file as an input. When a PDB file is imported into the GUI, pdb2adf is automatically called. The tool is, however, focused on biomolecules, and, with incomplete or faulty PDB files for biomolecules, successful atom-typing cannot be guaranteed although a recoded version (to be included in a future AMS release) comes a long way to that goal and will function for DNA, RNA, sugars, and different AMBER force fields.

TRIPOS[483] is a force field similar in simplicity to GAFF and AMBER, which has been parameterized for materials. Only the expressions for torsion and improper energy terms differ from the AMBER expressions. While a large set of TRIPOS parameters is available in AMS, there is currently no AMS tool for automatic atom-typing for the force field.

B. ReaxFF (reactive force fields)

The ReaxFF (reactive-force field) method, initially developed by van Duin *et al.* for hydrocarbons,[490] combines a bond-order dependent potential with a polarizable charge method, a combination which is potentially suitable to model any type of material—covalent, ionic, or metallic.[491] Formally, the bond order is a measurement of the number of electrons involved in the bond between a pair of atoms. ReaxFF describes a functional relationship between the interatomic distance and bond order and subsequently connects bond order to bond potential energy. As the potential energy is a function of bond order, bond breaking and formation are possible, contrary to the case for any nonreactive potentials where bond connectivity is assumed as fixed. ReaxFF simulations are highly effective in capturing detailed chemical events, reaction pathways for systems up to and beyond ~1 000 000 atoms and for timescales beyond tens of nanoseconds, which are typically not accessible by QM-based techniques. In addition to bond orders and polarizable charges, ReaxFF features van der Waals interactions, valence angles, dihedral angles, three-body and four-body conjugation terms, and a hydrogen bond. ReaxFF differs from the "first generation" reactive force fields such as Tersoff and Brenner,[492,493] by applying a significantly longer-ranged bond-order relationship combined with a single-step bond order correction that reduces the weaker bond orders for fully coordinated atoms, which makes it possible to achieve more accurate reaction kinetics. Note that while ReaxFF is significantly faster—and scales better—than typical QM-based methods, ReaxFF is significantly (50–100 times) slower than most non-reactive force fields and first-generation reactive force fields like the Tersoff, Brenner, and EAM potentials.[494] Since its first development in 2001, ReaxFF parameter sets have been developed for many elements and element combinations. The Senftle *et al.* 2016 review paper[491] provides a comprehensive overview of the ReaxFF developments between 2001 and 2016, while the more recent review by Nayir and co-workers provides a more focused review of ReaxFF developments and applications to 2D-materials.[495] Initially, ReaxFF was developed using the Electronegativity Equilibration Method (EEM) charge calculation method from Mortier and co-workers.[496] The EEM is still in use within ReaxFF—but we also have ReaxFF potentials available that utilize the Atom Condensed Kohn–Sham 2 charge calculation method[497]—which is essentially an expanded version of EEM that solves the unphysical long-range charge transfer problems associated with EEM. Furthermore, ReaxFF does not

feature explicit coupling of charges to bond orders—which limits its accuracy for describing ionization processes. For chemical systems that involve explicit charge transfer—for example redox reactions at battery systems—we have developed a version of ReaxFF that includes a limited explicit electron concept (e-ReaxFF).[498] Initial e-ReaxFF versions typically only included a single explicit electron in a molecule—where the rest of the molecule was described with the ACKS2 charge method.[499] More recently, an all-electron version of e-ReaxFF, where all neutral atoms are described as a Drude-like cation/electron pair, was developed.[500] This all electron version enables a straightforward description of electron vacancies and was successfully applied to simulate electron transfer and redox reactions in graphene/Li systems.

C. Machine learning potentials

Machine learning potentials (MLPs), also known as machine learning force fields, use a machine learning method, for example artificial neural networks, to describe the potential energy surface. AMS includes a few so-called foundation models, which are applicable to a wide variety of molecules or materials.

The ANI-1x,[501] ANI-1ccx,[502] and ANI-2x[503] models are examples of high-dimensional neural network potentials.[504] They have been trained to describe energies, geometries, and torsion profiles of mostly organic molecules.

The more recent AIMNet2-ωB97MD3 and AIMNet2-B973c message-passing neural network models[505] incorporate dispersion and electrostatic interactions. They were trained to organic and inorganic molecules and ions containing the elements H, B, C, N, O, F, Si, P, S, Cl, As, Se, Br, and I.

The ANI and AIMNet2 models are committee models containing several independently trained neural networks. In this way, those models can provide an uncertainty measure on predicted energies and forces.

The final foundation model included with AMS is the M3GNet-UP-2022[506] graph neural network potential, which was trained to PBE and PBE+U data from the Materials Project for the entire Periodic Table. Because it gives quite reasonable results for widely different chemistries, it serves as an ideal starting point for reparameterizing custom ML potentials with ParAMS. All foundation models can be executed on a GPU.

In addition to the included foundation models, there is also an interface to the Atomic Simulation Environment (ASE),[507] which makes it possible for the user to independently couple other published models, such as the CHGNet,[508] MACE,[509] MatterSim,[510] or SO3LR[511] universal potentials, to the AMS driver. Similarly, it is possible to couple custom trained models from packages such as NequIP,[512] PiNN,[513] SchNetPack,[514] sGDML,[515] and DeePMD-kit,[516] or any other package that has an ASE calculator.

VIII. REACTION NETWORKS

Reaction networks are large sets of interconnected chemical reactions. They differ from simple reaction mechanisms in that there often are many possible (side) products.

The prototypical reaction network case happens during combustion, in which thousands of intermediates may form. These intermediates are themselves very reactive, leading to many possible reaction pathways. However, even under more normal reaction conditions, whether in enzymes or heterogeneous or homogeneous catalysis, it is not uncommon to observe many different reactions.

AMS contains several tools for reaction network generation, refinement, and analysis.

A. Reaction network generation

1. Reactive molecular dynamics

The most straightforward way of generating a reaction network is to run reactive molecular dynamics, for example with ReaxFF or machine learning potentials, and keep track of any chemical reactions during the trajectory.

In some cases, such as combustion simulations, the temperature is so high that reactions occur on a typical MD time scale. However, chemical reactions are typically rare events and need to somehow be promoted during the MD simulation. The nanoreactor by Wang *et al.*[517] applies a bias at regular intervals, accelerating all molecules toward the center of the box. An acceleration period is followed by an equilibration period. Other approaches that have been implemented within AMS are the uniform-acceptance force-biased Monte Carlo (fbMC) method[518] as well as the collective-variable-driven hyperdynamics (CVHD),[519] which uses a collective variable and metadynamics to drive the system toward a transition, for example bond breakage. Near the transition state, the bias is removed, and if a reactive event occurs, the (global) bias is reinstated. By using hyperdynamics, it is possible to recover the time it would have taken in an unbiased simulation to arrive at the same result, but the free-energy information is lost.

2. ChemTraYzer2

The main tool to analyze the resulting reactive trajectories is ChemTraYzer2 (CT2).[520] CT2 works by first detecting all connectivity (bond) changes between all adjacent frames of the MD trajectory. This typically large set of reactive events is refined using a number of user-defined time windows (e.g., filtering out reactive species whose lifetime is less than the parameter Δt_{stable}; or lumping together reactions within a certain time frame, if the overall reactants and products are identical). Equivalent molecules and reactions are then aggregated and used to calculate population dynamics of each species over the trajectory as well as rate constants and associated uncertainties[521] for each elementary reaction.

A major part of the CT2 algorithm is detecting if molecules and reactions are equivalent. In CT2, this is done with a custom hashing function on the molecular graph. This molecular hash is generic and can be applied to all molecular structures (including those with any element, exotic species, unstable intermediates, etc.), providing a distinct advantage over many other molecule representations. The only requirement to generate these hashes is connectivity information for the molecule. ChemTraYzer2 uses bond order thresholds to determine the connectivity (bonds with very low bond order and/or a short lifetime are discarded). Although some engines do not provide bond orders (e.g., machine-learning potentials), these can be reliably estimated using a bond-guessing algorithm.

For both unbiased and biased simulations, all reactions in the trajectory can easily be accessed and can be used to calculate the reaction barriers and free energies in a more traditional way

using geometry optimizations, transition state searches, or intrinsic reaction coordinates.

3. Reaction discovery

AMS implements a special reaction discovery workflow to simplify the discovery of possible (side) reactions from a set of reactants. It combines the nanoreactor, ChemTraYzer2, and a special product ranking algorithm. In this way, it is possible with a minimal user input to get a sorted list of possible side products.

4. ACE reaction

ACE reaction by Kim *et al.*[522] is a fast but approximate method to find likely mechanisms for the conversion of a set of reactants into user-specified products. At its core, the method enumerates over all bonds that can be broken and formed. Molecules are considered simply as graphs, with atoms as vertices and bonds as edges. Three-dimensional molecular geometries are only considered to determine the stability of generated intermediates.

In addition to molecular system info on all reactant and product molecules, the user needs to provide the atom indices for a set of active reactant atoms, which are the only atoms that can participate in bond breaking/forming.

The ACE reaction procedure can be divided into three steps: (i) intermediate generation, where a set of intermediates is generated by enumeratively breaking and forming bonds in the reactant molecules, (ii) network creation, where the intermediates are connected by elementary reactions, identifying for each reaction the mechanism with the smallest number of broken/formed bonds, and (iii) network minimization, where the most likely mechanism through each intermediate is extracted, using shortest path algorithms.

5. PES exploration

The PESExploration module is a powerful tool designed for automated exploration of the PES. This module offers several strategies, such as ProcessSearch and basin hopping, to efficiently locate and characterize critical points on a PES, such as minima (representing stable reactants, intermediates, or products) and saddle points (representing transition states). A collection of local minima, and optionally the transition states connecting them, is referred to as an energy landscape. By automating this process, PESExploration saves significant time and effort compared to manual exploration methods.

The most popular strategy for PES exploration in AMS is the "ProcessSearch." This strategy starts from an initial minimum and performs random displacements followed by saddle point searches using the dimer method.[523,524] Once a saddle point is found, it follows the reaction path to the connected minima. This process is repeated iteratively to map out the reaction network and discover possible reaction pathways. Thus, the energy landscape is iteratively expanded to include more and more minima and transition states.

With PESExploration, it is possible to investigate various chemical phenomena, including intramolecular reactions and dissociation processes. In addition, the module includes functionalities for detecting binding sites, which is particularly useful in heterogeneous catalysis. It offers flexibility in customizing the exploration strategy, allowing users to define constraints, adjust search parameters, and specify the level of theory for energy and gradient calculations by just changing the calculation engine. Unfortunately, due to the large number of evaluations of the potential, this module is computationally very demanding and normally only suitable for use with fast engines like DFTB, ReaxFF, or machine learning potentials. However, once an energy landscape has been found, it can be refined using DFT calculations with ADF or BAND.

B. Microkinetics and kinetic Monte Carlo

Once a reaction network has been obtained, it can be further analyzed with the help of microkinetics and kinetic Monte Carlo.

1. Microkinetics

AMS includes an interface to the microkinetics program MKMCXX,[525] which can be used to set up and run microkinetic simulations. In microkinetic simulations, for a given temperature and pressure, the concentrations of different chemical species are evolved using predefined reactions (the reaction network) with known rate coefficients. Microkinetics is a very fast way of solving the rate equations.

2. Kinetic Monte Carlo

AMS includes an interface to the Zacros kinetic Monte Carlo program,[526,527] which is particularly well suited for performing heterogeneous catalysis simulations. Kinetic Monte Carlo simulations explicitly take all elementary steps into account, including barriers for diffusion on the surface. Reactions only occur between neighboring molecules.

The interface, written in Python and called pyZacros, allows users to set up, run, and analyze Zacros simulations directly from Python scripts, streamlining the entire workflow. Designed as an extension of PLAMS (see Sec. XI), it inherits the robust way of managing input file preparation, job execution, file management, and output file processing. With pyZacros, you can define the lattice structure, adsorption sites, gas-phase species, surface reactions, and simulation parameters using intuitive Python syntax. It also provides tools for analyzing the simulation results, such as plotting coverages, rates, and reaction pathways. By automating these tasks, pyZacros makes it easier to perform complex kinetic Monte Carlo simulations and explore catalytic processes in greater detail. In addition, pyZacros can read energy landscapes directly from the AMS PESExploration module results to set up the Zacros simulation automatically.

Kinetic Monte Carlo is also extensively used in the Bumblebee program,[528–530] a simulation tool used to model the long-term behavior of organic light-emitting diode (OLED) materials, and works by tracking the diffusion of carriers, molecular emissions, and device degradation over time.

IX. FLUID-PHASE THERMODYNAMICS

AMS also contains a number of methods for the prediction of properties at the macroscale. The available methods in AMS are all fluid-phase thermodynamics models, which calculate the chemical potential (μ) as a function of temperature and concentration for all species in a liquid or gaseous phase. Because the chemical potential is a fundamental thermodynamic descriptor, it can be used to calculate many useful thermodynamic quantities, including activity coefficients, phase diagrams, solubilities, partial pressures, logP,

TABLE II. Some thermodynamic properties available in AMS.

Activity coefficients (γ)	Bubble/dew point curves
Chemical potentials (μ)	pK_a
Excess properties (G^E, H^E, S^E)	Free energy of solvation (ΔG_{solv})
Phase equilibria	Enthalpy of vaporization
(VLE, LLE, SLE)	(ΔH_{vap})
Henry's law constant	Flory–Huggins χ
Azeotropes	Binodal/spinodal curves
Partial pressures	Eutectics
logP	Distribution of conformers
Solubility of solids, liquids,	Distribution of associated
and gases in liquids	and dissociated species

and many others. A summary of some useful properties that can be calculated in AMS is given in Table II.

A. UNIFAC

The UNIFAC[531] method is one of the most well-known activity coefficient models. Like the UNIQUAC model it is derived from, UNIFAC is based on local composition theory and requires surface area, volume, and interaction energy parameters. However, while UNIQUAC requires known parameters for all these terms for every molecule, UNIFAC uses a group contribution method to generate the surface area and volume of each molecule as well as group interaction parameters for each group. This means that UNIFAC can be widely applied to many types of systems without the need for molecule-specific parameters. In addition, decades of development and significant parameterization efforts have led to UNIFAC being a very accurate and reliable model. The main drawback of this model is that the table of interaction parameters is incomplete, and UNIFAC cannot perform a calculation for any molecular system with a missing parameter.

B. COSMO-RS and COSMO-SAC

Like UNIFAC, the COSMO-RS[532] and COSMO-SAC[533] models are widely used and trusted in the chemistry and chemical engineering communities, for example when studying the thermodynamic properties of crude oil components in sea ice oil spills.[534] These models have extensive applications and very few parameters. There are additionally no areas of the chemical space for which there are missing parameters, meaning that COSMO-RS and COSMO-SAC can be applied to any chemical system. These methods are also particularly well-suited for use with AMS because they rely on quantum chemistry calculations, which can easily be achieved with our integrated computational chemistry suite.

The COSMO-RS and COSMO-SAC models calculate μ of each species relative to the ideal conductor ($\epsilon = \infty$) reference state. This reference state is not physically realistic but is readily accessible as a standard quantum chemistry calculation using the COSMO method.[438] To calculate μ values for a real mixture of compounds, the surface charge density of the COSMO surface is first sampled and then processed into a histogram called a σ-profile. The σ-profile relates surface charge density to molecular surface area and is the

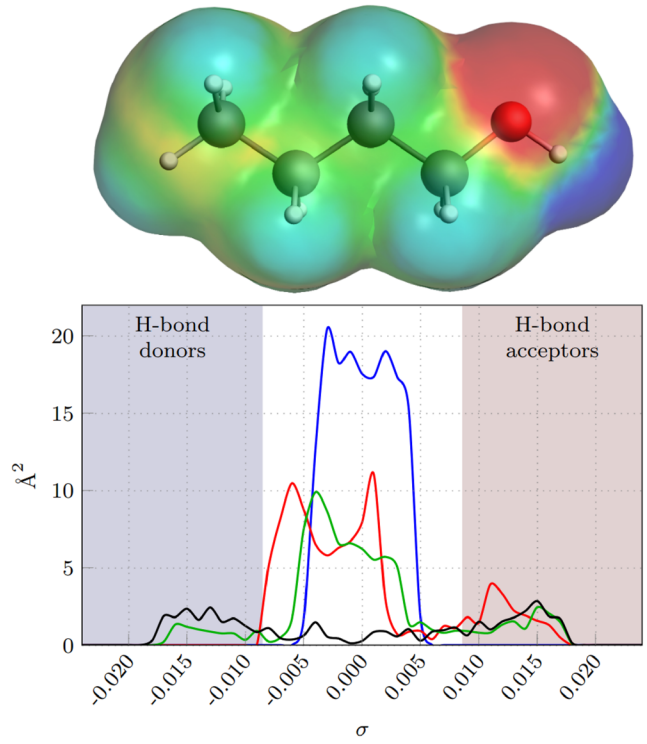

FIG. 8. The COSMO surface of 1-butanol (above) and example σ-profiles (below) for hexane (blue), acetone (red), ethanol (green), and water (black).

fundamental descriptor for a molecule in COSMO-RS and COSMO-SAC. Figure 8 provides an example of a COSMO surface and some σ-profiles for a few molecules. For a real mixture, chemical potentials are calculated from a statistical thermodynamics treatment of the σ-profiles of all compounds and energy penalty terms from electrostatics accounting for mismatched surface charges. The equation for the chemical potential in COSMO-RS (COSMO-SAC is very similar) of a surface segment with charge density σ in the ensemble mixture is given as follows:

$$\mu^S_\sigma = \frac{-RT}{a_{\text{eff}}} \ln\left(\sum_{\sigma'} p^S_{\sigma'} \exp\left(\frac{a_{\text{eff}}(\mu^S_{\sigma'} - e(\sigma,\sigma'))}{RT}\right)\right), \quad (29)$$

where a_{eff} is a constant, e represents a function for the energy penalty of placing two surface points with charge densities of σ and σ' in contact, p^S is the composition-weighted σ-profile of the mixture, R is the gas constant, and T is the absolute temperature. The chemical potential of each species is easily calculated from μ^S. It should also be noted that this equation is a simplified version of what is used in the AMS implementation as some methods distinguish H-bonding and non-H-bonding parts of the sigma profile, have temperature-dependent e function, etc. A more detailed description of COSMO-based methods is given in Ref. 535.

Equation (29) also demonstrates a major advantage of COSMO-RS/-SAC: users only need to perform the COSMO calculation once per compound—these results can be reused for that compound in any arbitrary mixture. In AMS, the results of a COSMO

calculation are stored in a `.coskf` file. For convenience, the software includes thousands of `.coskf` files for common molecules.

AMS contains various parameter sets for COSMO-RS, including some fit specifically for ADF COSMO results.[437] There are also several implementations of the COSMO-SAC model available in AMS, including those with improved dispersion interactions[536] and directional H-bonding.[537]

C. Extensions, application domains, and utilities

1. Ionic liquids

COSMO-RS/-SAC methods are known to work well for ionic liquid (IL) systems.[538] Successful applications have been demonstrated in many areas, including gas solubilities, VLE/LLE in aqueous and organic IL systems, and solvent replacement problems. Due to the nature of ILs, the charge is usually delocalized on at least one ion of the cation/anion pair. This leads to relatively low polarization and means that the σ-profiles of ILs tend to fall in the prediction domain of COSMO-RS/-SAC (typically mixtures of neutral species). This is clear in the AMS COSMO-RS/-SAC methods, where one can expect quality results when using ionic liquids with the default parameters. ILs in AMS work just like any other compound and can be used to calculate any available thermodynamic property. AMS also provides a database of several hundred `.coskf` files for common cations and anions.

2. Polymers

Polymers can also be modeled with COSMO-RS/-SAC. The default procedure involving a quantum chemistry calculation in the COSMO solvent is obviously untenable for the number of atoms in a typical polymer. To make them accessible to these methods, an approximation is done where we first calculate the COSMO surface exclusively for the central monomer of a trimer. This partial COSMO surface represents the average surface for a monomer, so its corresponding σ-profile is scaled up according to the number of repeat units in the whole polymer. This method can be used with the default COSMO-RS/-SAC parameters and a modified combinatorial term.[539] This approach works for many types of polymers: homopolymers, block copolymers, and alternating copolymers. For polymer systems, AMS additionally calculates activity coefficients in weight and volume fraction units, which are more conventional in the polymer literature.

3. Electrolytes

Charged species often demonstrate behavior that is difficult to capture for COSMO-RS/-SAC models. One of the primary reasons for this is that the electrostatic potential is not included in these models by default. In AMS, our COSMO-RS/-SAC methods have the option to add the Pitzer–Debye–Hückel (PDH) long-range electrostatic correction[540] in order to describe this missing contribution to the potential. Small ions present another challenge due to their high charge densities, and it is recommended to experiment with the default radii for small ions as these may be significantly different than their neutral counterparts.

4. Conformers, associations, and dissociations

COSMO-RS/-SAC models traditionally only use a single structure to represent a single component of a mixture. This paradigm works well for much of the chemical space but often fails to accurately describe solutions with more complex behavior. Such systems may involve an appreciable amount of multiple conformers of a single molecule at equilibrium, significant dimerization or trimerization, explicit association between two or more species, or a compound that dissociates to a significant degree. In AMS, all these phenomena can be modeled using the `Multispecies` tools, which allow a user to define a compound as a collection of conformers, dimers, dissociation products, etc., as well as specify explicit associations that occur with that compound and other species in the mixture.

The `Multispecies` program then uses COSMO-RS/-SAC to determine the optimal equilibrium distribution of all species subject to the mass balances defined by the problem. Although the program calculates chemical potentials for every unique species in the solution, it reports the chemical potential and activity coefficients for the *apparent* compounds, which correspond to values that would be measured in the lab. To our knowledge, the `Multispecies` tools are a unique feature of our software. Although many COSMO-RS/-SAC implementations allow for modeling conformers, ours stands alone in its ability to generically model dimerization, associations, and dissociations simultaneously.

5. Utilities

The fluid thermodynamics codes in AMS can also interface with a number of useful utility functions and programs. For example, the program `FastSigma` allows users to quickly estimate the σ-profile of a compound from its SMILES string, which circumvents the most expensive step (the COSMO calculation) of COSMO-RS/-SAC. These estimated profiles can immediately be used with COSMO-RS/-SAC, making `FastSigma` a very useful tool for quick estimations of thermodynamic properties or high-throughput screening. In addition, the program `PropPrediction` provides quick estimates for physical properties, including vapor pressures, melting points, density, and many others. This can be useful when a physical property is required to do a calculation (e.g., for VLE or SLE) but the experimental value is not known. The program `SolventOpt`[541] uses advanced optimization methods directly with the COSMO-RS/-SAC equations to optimize mixed solvents for solubility and separation applications.

X. PARAMETERIZATION: ParAMS

The ParAMS program is a general-purpose parameterization tool that can be used to parameterize any AMS engine.[542] The graphical user interface directly provides information on the progress of the parameterization, and how large any prediction errors are.

ParAMS contains specific interfaces to parameterize ReaxFF, DFTB (in particular, the GFN1-xTB Hamiltonian), and the M3GNet machine learning potential. Some example applications include training a ReaxFF force field for perovskites[543] and improving the Si interactions in GFN1-xTB.[544]

A. Training set

ParAMS is designed to be as flexible as possible with respect to the training set (and validation set and test set) entries.

The results from any AMS task can be used during the training, and multiple jobs can be combined into a single training set entry.

TABLE III. Common ParAMS properties in the training set. The task refers to the type of job that runs during the parameterization, not the task that was used to generate the reference data. For ML training, only single point calculations are supported.

No. of jobs	Task	Common extractors
1	Single point	Energy, forces, charges
1	Geom. opt.	Energy, bond lengths, angles
1	PES scan	Relative energy curve
≥2	Geom. opt.	Reaction energy
1	MD/NEB/. . .	Not commonly used

Table III lists the most common properties extracted from jobs, but more properties are supported, and any result that can be obtained by reading the AMS binary output file can be used for training.

The reference data can either come from experiment or from reference DFT calculations. In the latter case, ParAMS has a convenient set of result importers to extract the most common properties.

For example, Fig. 9 shows the DFT-calculated bond scan (ADF, PBE, DZP) for the C(1)–N(2) bond in N-methylimidazole in black. Importing such a PES scan into ParAMS can be done in two ways: either as five single point calculations (cf. red line in Fig. 9) or as an equivalent PES scan (purple line). If it is imported as PES scan, this means that during the parameterization, for every new set of ReaxFF parameters, AMS will perform a complete PES Scan, relaxing all other degrees of freedom. In either case, the training set entries correspond to the energy difference relative to the minimum, and the optimization would minimize the difference between the red/purple curve and the black reference curve.

In addition to the training set, a validation set can also be used. The optimization algorithm does not attempt to minimize the loss on the validation set. Instead, the validation set loss is calculated so that the user can judge if overfitting has taken place.

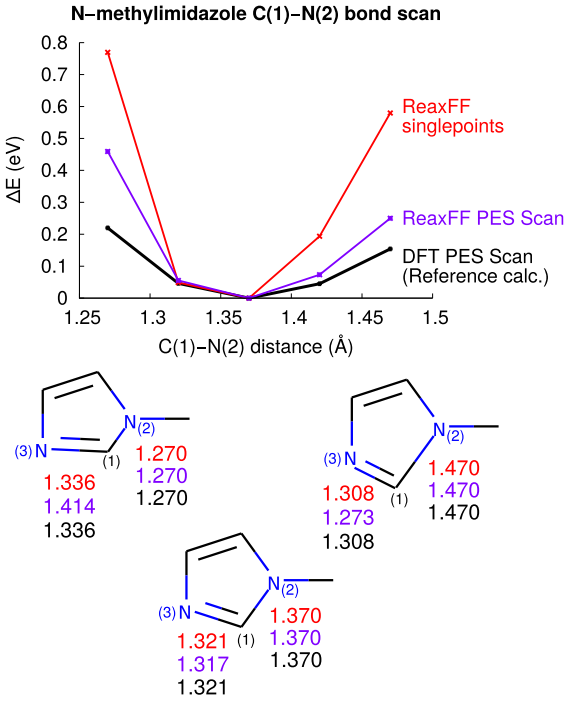

FIG. 9. Black: Energy curve for the C(1)–N(2) bond calculated with DFT. Red: ReaxFF single points on the DFT bond scan structures. Purple: Equivalent ReaxFF bond scan, using the same C(1)–N(2) distances but relaxing all other degrees of freedom. In the bottom half, three of the five molecules are shown with distortions exaggerated. The numbers show the C(1)–N(2) and C(1)–N(3) bond lengths (Å). The red and black structures are always identical, but the C(1)–N(3) bond length is different for the ReaxFF PES scan, as that bond (and all other bonds) is relaxed using ReaxFF.

B. Parameter optimization and sensitivity analysis

ReaxFF and DFTB optimizations run through GloMPO (Globally Managed Parallel Optimization).[545] This lets the user run many optimizers in parallel. Optimizers converging to bad solutions can be automatically turned off, and new ones started in their stead. The default optimizer in ParAMS is the Covariance Matrix Adaptation Evolution Strategy (CMA-ES), but many other algorithms are available.

The goal of the optimization is to get the lowest possible loss function value. The loss function is typically defined as the sum of squared-errors between the reference and computed values. Because the training set can contain different types of quantities (e.g., energies and forces) expressed in different units, the prediction error is first normalized by a parameter σ that accounts for the type of quantity and the unit that it is expressed in. An intuitive interpretation of σ is that it corresponds to an acceptable prediction error.

Force fields such as ReaxFF can be difficult to optimize due to their many degrees-of-freedom and noisy landscape. ParAMS includes a sensitivity tool based on the Hilbert–Schmidt independence criterion (HSIC) global sensitivity method.[546] This tool can be used as a preprocessing step to identify the most important parameters. By optimizing only the most sensitive parameters, the optimization is faster and less prone to overfitting.

C. Active learning

The accuracy of ML potentials is largely determined by the training set used during the fitting of the parameters. How to best construct good training and validation sets is the subject of active research.[547,548] The datasets should strike the balance of being sufficiently diverse, informative, and representative,[549] while at the same time not be too large in order to save time on reference DFT or *ab initio* calculations and parameter training.

In particular, the concept of active, iterative, or on-the-fly learning holds much promise. In this method, the trained ML potential itself is used to generate new structures for further expansion of the training set.

AMS includes a workflow for active learning (AL) of ML potentials based on molecular dynamics (MD) simulations. In order to promote structural diversity, the MD simulations can be set up to, for example, sample ranges of temperatures, pressures, densities, lattice strains, chemical compositions (e.g., with surface deposition), conformers (e.g., with CREST[24]), enforced chemical reactions or diffusion (targeted MD), or any user-defined structural collective variable (with PLUMED[23]). The MD-based workflow can also be

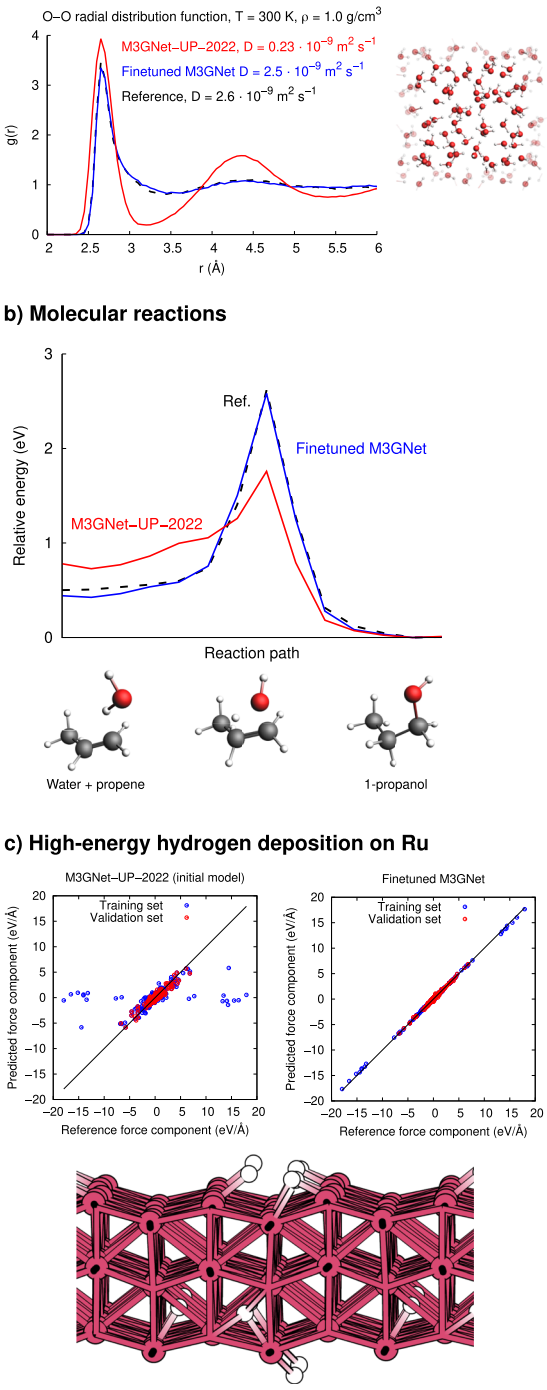

FIG. 10. Example results for fine-tuning the M3GNet-UP-2022 potential with active learning for various applications. (a) Liquid water radial distribution functions with self-diffusion coefficients D (reference method: ReaxFF Water2017.ff[551]), (b) reaction path of the addition reaction water + propene → 1-propanol, from climbing image nudged elastic band [reference method: PBE-D3(BJ)], and (c) high-energy hydrogen deposition on a Ru surface [reference method: PBE-D3(BJ)]. The input needed to reproduce these results is provided in the AMS documentation.

combined with manual addition of training data from NEB, PES scans, etc.

Two methods are implemented to select structures: (i) reference calculations are performed at given pre-defined points during the simulation, and if the model is not accurate enough, then the current and possibly additional structures are added to the training set, and (ii) if the model provides an uncertainty measure, then a reference calculation is performed when the uncertainty exceeds some threshold. These two methods loosely correspond to the concepts of offline and online active learning, respectively (see, for example, Ref. 550). To get uncertainty measures, ParAMS supports the training of committee models, which allow for the selection of training points through query-by-committee.

The AL workflow in AMS places a special emphasis on robustness. When applying ML potentials to MD simulations, there is a risk of catastrophic events when the simulation explores structures that are not similar to those in the training set. Such events include, for example, atoms overlapping or the system releasing a lot of energy, resulting in a significant temperature increase. AMS tries to identify such events during the AL and discards unrealistic structures through a set of reasonable simulation criteria.

The details of the workflow are described in the AMS documentation, which also provides several examples and case studies that illustrate how successful the active learning can be. Figure 10 shows how AL can be used to train ML potentials that (a) reproduce reference radial distribution functions and diffusion coefficients of liquid water, (b) give better reaction energies and barriers for molecular reactions, and (c) identify and correct highly inaccurate predictions in the M3GNet-UP-2022[506] universal model, for high-energy bombardment of hydrogen on a Ru surface (H in white and Ru in purple).

XI. PYTHON WORKFLOWS

AMS includes a Python distribution, `amspython`, that comes with many useful packages such as numpy, scipy, and RDkit preinstalled. Some packages contain AMS-specific functionality. The most prominent Python package for AMS is PLAMS (Python Library for Automating Molecular Simulations) although other Python libraries can also interface with AMS.[552,553]

PLAMS is an open-source package for setting up, running, and analyzing simulation jobs. PLAMS works for multiple different computational codes (not only AMS but also, for example, DFTB+ and ORCA) and can easily be expanded to handle new codes. Within AMS, PLAMS is used not only for AMS driver calculations but also to run ParAMS, conformer search, Zacros, etc.

PLAMS implements its own queueing system that also integrates with batch systems such as SLURM. This means that a script can contain multiple jobs. A job will only be started when there are available resources.

Example PLAMS script to calculate the single-point energy of water with ADF:

```
from scm.plams import from_smiles, Settings, AMSJob
molecule = from_smiles('O')
s = Settings()
s.input.ams.Task = 'SinglePoint'
```

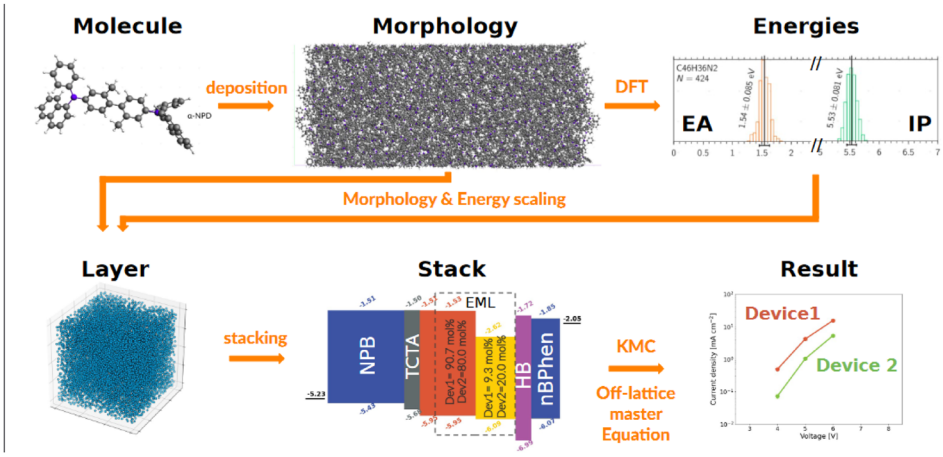

FIG. 11. Schematics of the AMS OLED workflow. The molecule(s) that make up the device are first deposited to form a morphology, and then, the electronic properties of the bulk are calculated quantum mechanically. The resulting data are used for the device-level simulations of the stack.

```
s.input.ADF.Basis.Type = 'TZP'
s.input.ADF.XC.GGA = 'PBE'
job = AMSJob(settings=s, molecule=molecule)
job.run()
energy = job.results.get_energy()
```

Scripts of this type can be set up to perform virtually any type of AMS simulation and to later parse and analyze the results with great flexibility.

By using PLAMS, we have also developed complex workflows that enable users to utilize some of the more involved parts of the software with great ease. One such example is the aforementioned reaction discovery workflow (see Sec. VIII B 3). Another is the OLED workflow, which has been especially developed to simulate the properties of highly complex OLED materials from first principles. The latter workflow, shown in Fig. 11, is composed of three different parts. The first is a deposition step, in which the molecules forming the main layer of the device are deposited one by one, forming thin film. This is achieved using a molecular dynamics and force-bias Monte Carlo calculation mimicking physical vapor deposition. In the second step, the morphology resulting from the deposition is used to obtain the distributions (and possibly spatial correlations) of molecular properties, such as ionization potential, electron affinity, and exciton energies at the DFT level. Each molecule's environment is taken into account in a polarizable QM/MM scheme using the DRF model described above. Finally, the properties calculated are fed to the Bumblebee program, a software application specifically developed to perform device-level OLED simulations using either experimental or calculated data as an input using the 3D kinetic Monte Carlo approach.[528–530] The first two steps (deposition and properties calculations) are fully integrated into the AMS GUI, allowing even non-expert users to easily utilize the entire workflow. It should also be remarked that the automation and integration of such a complex scheme are only possible thanks to the vast array of engines available within AMS as well as the Python integration, which seamlessly connect the result of classical MD simulations with complex quantum mechanical calculations.

XII. CONCLUSIONS

The Amsterdam Modeling Suite is a powerful tool that can perform a wide array of simulations on chemical systems. In this paper, we have presented the design principles that have guided the development of AMS and all of its packages and described the various modules that compose it, from the quantum chemistry engines such as ADF and BAND to the more recently developed machine-learning tools. The development of AMS started all the way back in the 1970s when the first contributions to the DFT code ADF were made, and over the following decades, the program was further augmented by expanding the range of methods and properties, refined to increase computational efficiency, and complemented with the addition of specialized codes such as ReaxFF and DFTB. Thanks to these advancements, AMS can now offer a solution to most quantum chemistry problems. We have also described the non-QM components of the suite that have been developed in recent years, including the classical engines that can perform molecular dynamics simulations, our program for fluid thermodynamics simulations, and the machine-learning, parameterization, and scripting tools. All these developments would be of little use if it were not for the presence of specific tools that allow even non-expert users to take full advantage of them. In AMS, these include our Graphical User Interface (GUI), which allows one to easily build a complex chemical system, easily invoke any of our engines, and analyze calculation results, and also the Python libraries that make it easy to write scripts that combine different calculations into workflows. In fact, the strength of AMS lies both in the quality of each of its components taken singularly and in their variety and interoperability, which allows for the creation of workflows for the simulation of highly complex systems and phenomena.

ACKNOWLEDGMENTS

Over time—several decades—very many people have contributed to the AMS program system. We are not able to list all of them here, but we want to single out a few contributors who have in the past been very instrumental for a long time. First of all,

Tom Ziegler and Jaap Snijders (both deceased) deserve many thanks for their momentous contributions. The relativistic functionality of ADF and the implemented spectroscopic simulation techniques owe very much to their work, drive, and enthusiasm. Bert te Velde has been primarily responsible for the development of BAND and as first CEO of the SCM company did the ground work for the development of the program system from a tool for academic research to an all-round simulation package.

This paper focuses on the scientific methods and implementation aspects. In practice, the GUI plays a very important role; it is for most users the primary vehicle for operating and navigating the large system. We thank Olivier Visser as an initiator and long-time developer, as well as Laurens Groot, for their efforts and achievements.

The many people who have contributed in the past, or in other ways than to the scientific background, are listed on the SCM website, at https://www.scm.com/partners-contributors.

The Amsterdam Modeling Suite and its many modules are distributed through the website www.scm.com where information on licensing can be found, such as the available modules and programs as well as the different types of licenses available. Much information is freely available, e.g., manuals for the various engines and overviews of the use of the GUI and of many tutorials.

AUTHOR DECLARATIONS

Conflict of Interest

The AMS suite is owned, extended, and commercially distributed by Software for Chemistry and Materials BV (SCM). It is continuously being developed and extended by academic developers and by SCM itself. Several authors are employees and/or shareholders of SCM.

Author Contributions

Evert Jan Baerends: Conceptualization (equal); Writing – original draft (equal). **Nestor F. Aguirre**: Writing – original draft (supporting). **Nick D. Austin**: Writing – original draft (supporting). **Jochen Autschbach**: Writing – original draft (supporting). **F. Matthias Bickelhaupt**: Writing – original draft (supporting). **Rosa Bulo**: Writing – original draft (supporting). **Chiara Cappelli**: Writing – original draft (supporting). **Adri C. T. van Duin**: Writing – original draft (supporting). **Franco Egidi**: Conceptualization (equal); Writing – original draft (equal). **Célia Fonseca Guerra**: Writing – original draft (supporting). **Arno Förster**: Writing – original draft (supporting). **Mirko Franchini**: Writing – original draft (supporting). **Theodorus P. M. Goumans**: Writing – original draft (supporting). **Thomas Heine**: Writing – original draft (supporting). **Matti Hellström**: Conceptualization (equal); Writing – original draft (equal). **Christoph R. Jacob**: Writing – original draft (supporting). **Lasse Jensen**: Writing – original draft (supporting). **Mykhaylo Krykunov**: Writing – original draft (supporting). **Erik van Lenthe**: Writing – original draft (supporting). **Artur Michalak**: Writing – original draft (supporting). **Mariusz M. Mitoraj**: Writing – original draft (supporting). **Johannes Neugebauer**: Writing – original draft (supporting). **Valentin Paul Nicu**: Writing – original draft (supporting). **Pier Philipsen**: Writing – original draft (supporting). **Harry Ramanantoanina**: Writing – original draft (supporting). **Robert Rüger**: Writing – original draft (supporting). **Georg Schreckenbach**: Writing – original draft (supporting). **Mauro Stener**: Writing – original draft (supporting). **Marcel Swart**: Writing – original draft (supporting). **Jos M. Thijssen**: Writing – original draft (supporting). **Tomáš Trnka**: Writing – original draft (supporting). **Lucas Visscher**: Writing – original draft (supporting). **Alexei Yakovlev**: Writing – original draft (supporting). **Stan van Gisbergen**: Writing – original draft (supporting).

DATA AVAILABILITY

Data sharing is not applicable to this article as no new data were created or analyzed in this study.

NOMENCLATURE

3D-RISM	three-dimensional reference interaction site model
AAT	atomic axial tensor
ABS	auxiliary basis set
AC	absolute configuration
ACE	automated construction of elementary reactions
ACFDT	adiabatic connection fluctuation–dissipation theorem
ACKS2	atom-condensed Kohn–Sham DFT approximated to second order
ADF	Amsterdam Density Functional program
AIMNet2	atoms-in-molecules neural network potential second generation
AL	active learning
ALDA	adiabatic local density approximation
AMS	Amsterdam Modeling Suite
ANI	Accurate neural network engine for molecular energies
AO	atomic orbital
APT	atomic polar tensor
ASD	activation strain diagram
ASE	Atomic Simulation Environment
ASM	activation strain model
AXK	approximate exchange kernel
BSE	Bethe–Salpeter equation
CBL	complete basis set limit
CD	circular dichroism
CI	configuration interaction
CM5	charge model 5
CMA-ES	covariance matrix adaptation evolution strategy
COOP	crystal orbital overlap population
COSMO	conductor screening model
CPIM	capacitance polarizability interaction model
CPL	circularly polarized luminescence
CPU	central processing unit
CREST	conformer–rotamer ensemble sampling tool
CSOV	constrained space orbital variation
CT2	ChemTraYzer2
CVHD	collective-variable-driven hyperdynamics
DFA	density functional approximation
DFT	density functional theory
DFTB	density functional tight binding
DH	double hybrid
DIM	discrete interaction model
DRF	discrete reaction field

EA	electron affinity
ECD	electronic circular dichroism
EDA	energy decomposition analysis
EDTM	electric dipole transition moment
EELS	electron energy loss spectroscopy
EEM	electronegativity equilibration method
EFG	electric field gradient
ERI	electron repulsion integral
ESID	energy splitting in dimer
ESR	electron spin resonance
ETS	extended transition state
evGW	eigenvalue-only self-consistent GW
fbMC	force-biased Monte Carlo
FCF	Franck–Condon factor
FDE	frozen density embedding
FF	force field
FNV	finite nuclear volume
FO	fragment orbital
FQ	fluctuating charges
FQFμ	fluctuating charges and dipoles
GAFF	general AMBER force field
GA-HC	genetic algorithm hierarchical clustering
GCMC	grand canonical Monte Carlo
GCO	general coupled-oscillator
GFN	geometry, frequency, noncovalent
GGA	generalized gradient approximation
GIAO	gauge-including atomic orbital
GloMPO	globally managed parallel optimization
GPU	graphics processing unit
GTO	Gaussian type orbital
GUI	graphical user interface
GWA	GW approximation
HC	hierarchical clustering
HF	Hartree–Fock
HFF	harmonic force field
HOMO	highest occupied molecular orbital
HSIC	Hilbert–Schmidt independence criterion
IL	ionic liquid
IP	ionization potential
IR	infrared
IRC	intrinsic reaction coordinate
KK	Kramers–Kronig
KMC	kinetic Monte Carlo
KS	Kohn–Sham
LDA	local density approximation
LFDFT	ligand field density functional theory
LLE	liquid–liquid equilibria
LRC	long-range corrected
LRI	local resolution of the identity
LUMO	lowest unoccupied molecular orbital
M3GNet	materials three-body graph network interatomic potential
MAPA	four-component Dirac equation for a model potential
MBH	mobile block Hessian
MBPT	many-body perturbation theory
MCD	magnetic circular dichroism
MD	molecular dynamics
MDTM	magnetic dipole transition moment
MLP	machine learning potential
MM	molecular mechanics
MO	molecular orbital
MOPAC	Molecular Orbital PACkage program
MOR	magneto-optical rotation
MP2	Møller–Plesset perturbation theory second order
NAO	numerical atomic orbital
NBO	natural bond orbital
NDDO	neglect of diatomic differential overlap
NEGF	non-equilibrium Green's function
NEXAFS	near edge x-ray absorption fine structure
NICS	nucleus-independent chemical shift
NLMO	natural localized molecular orbital
NMR	nuclear magnetic resonance
NOCV	natural orbitals for chemical valence
OLED	organic light-emitting diode
ORD	optical rotatory dispersion
PADF	pair atomic density fitting
ParAMS	Parameter Optimization for Atomistic and Molecular Simulations program
PARI	pair atomic resolution of the identity
PDH	Pitzer–Debye–Hückel
PES	potential energy surface
PIM	polarizability interaction model
PLAMS	Python library for automating molecular simulations
PLUMED	PLUgin for MolEcular Dynamics
pNA	*para*-nitroaniline
PolTDDFT	polarizability time-dependent density functional theory
PSII	photosystem II
QE	Quantum ESPRESSO
QM	quantum mechanics
qsGW	quasiparticle self-consistent GW
QTAIM	quantum theory of atoms in molecules
QUILD	quantum-regions interconnected by local descriptions
QZ4P	quadruple zeta STO basis plus 4 polarization functions
RC	reaction center
ReaxFF	reactive force field
RI	resolution of the identity
ROA	Raman optical activity
RPA	random phase approximation
RR	resonance Raman
SAOP	statistical average of orbital potentials
SCC	self-consistent charge
SCF	self-consistent field
SCM	Software for Chemistry and Materials
sDFT	subsystem density functional theory
SERS	surface-enhanced Raman spectroscopy
SFO	symmetry-adapted linear combinations of fragment orbitals
sGDML	symmetric gradient domain machine learning
SIESTA	Spanish Initiative for Electronic Simulations with Thousands of Atoms
SLE	solid–liquid equilibria
SLURM	Simple Linux Utility for Resource Management
SM12	solvation model 12 (Minnesota)

SMILES	Simplified Molecular Input Line Entry System
SO	spin–orbit
SOCME	spin–orbit coupling matrix elements
SOSEX	second-order screened exchange
SOX	second-order exchange
sTDA	simplified Tamm–Dancoff approximation
sTDDFT	simplified time-dependent density functional theory
STO	Slater type orbital
TDA	Tamm–Dancoff approximation
TDDFT	time-dependent density functional theory
TS	transition state
TZP	triple zeta STO basis plus polarization
UFF	universal force field
UNIFAC	universal quasichemical functional group activity coefficient
UNIQUAC	universal quasichemical
VCD	vibrational circular dichroism
VDD	Voronoi deformation density
VLE	vapor–liquid equilibria
X2C	exact two-component
XANES	x-ray absorption near edge structure
XAS	x-ray absorption spectroscopy
XES	x-ray emission spectra
XPS	x-ray photoelectron spectroscopy
xTB	extended tight binding
ZFS	zero-field splitting
Zlm fit	density fitting with radial spline functions and real spherical harmonics
ZORA	zeroth order regular approximation

REFERENCES

[1]E. J. Baerends, D. E. Ellis, and P. Ros, "Self-consistent molecular Hartree–Fock–Slater calculations I. The computational procedure," Chem. Phys. **2**, 41–51 (1973).
[2]C. Fonseca Guerra, J. G. Snijders, G. te Velde, and E. J. Baerends, "Towards an order- N DFT method," Theor. Chem. Acc.: Theory, Comput., Model. **99**, 391–403 (1998).
[3]R. M. Martin, L. Reining, and D. M. Ceperley, *Interacting Electrons* (Cambridge University Press, 2016).
[4]C. Møller and M. S. Plesset, "Note on an approximation treatment for many-electron systems," Phys. Rev. **46**, 618–622 (1934).
[5]W. Macke, "Über die wechselwirkungen im Fermi-Gas. Polarisationserscheinungen, correlationsenergie, elektronenkondensation," Z. Naturforsch. A **5**, 192–208 (1950).
[6]D. Bohm and D. Pines, "A collective description of electron interactions: III. Coulomb interactions in a degenerate electron gas," Phys. Rev. **92**, 609–625 (1953).
[7]M. Gell-Mann and K. A. Brueckner, "Correlation energy of an electron gas at high density," Phys. Rev. **106**, 364–368 (1957).
[8]P. Nozières and D. Pines, "Correlation energy of a free electron gas," Phys. Rev. **111**, 442–454 (1958).
[9]L. Hedin, "New method for calculating the one-particle Green's function with application to the electron-gas problem," Phys. Rev. **139**, A796 (1965).
[10]G. Strinati, "Application of the Green's functions method to the study of the optical properties of semiconductors," La Rivista del Nuovo Cimento **11**, 1–86 (1988).
[11]F. Aryasetiawan and O. Gunnarsson, "The **GW** method," Rep. Prog. Phys. **61**, 237–312 (1998).
[12]G. Onida, L. Reining, and A. Rubio, "Electronic excitations: Density-functional versus many-body Green's-function approaches," Rev. Mod. Phys. **74**, 601 (2002).
[13]E. v. Lenthe, E. J. Baerends, and J. G. Snijders, "Relativistic regular two-component Hamiltonians," J. Chem. Phys. **99**, 4597–4610 (1993).
[14]E. van Lenthe, E. J. Baerends, and J. G. Snijders, "Relativistic total energy using regular approximations," J. Chem. Phys. **101**, 9783–9792 (1994).
[15]E. van Lenthe, J. G. Snijders, and E. J. Baerends, "The zero-order regular approximation for relativistic effects: The effect of spin–orbit coupling in closed shell molecules," J. Chem. Phys. **105**, 6505–6516 (1996).
[16]E. van Lenthe, A. Ehlers, and E.-J. Baerends, "Geometry optimizations in the zero order regular approximation for relativistic effects," J. Chem. Phys. **110**, 8943–8953 (1999).
[17]G. te Velde and E. J. Baerends, "Precise density-functional method for periodic structures," Phys. Rev. B **44**, 7888–7903 (1991).
[18]P. Romaniello and P. L. de Boeij, "Relativistic two-component formulation of time-dependent current-density functional theory: Application to the linear response of solids," J. Chem. Phys. **127**, 174111 (2007).
[19]J. Baker, "Constrained optimization in delocalized internal coordinates," J. Comput. Chem. **18**, 1079–1095 (1997).
[20]J. Baker *et al.*, "Geometry optimization in delocalized internal coordinates: An efficient quadratically scaling algorithm for large molecules," J. Chem. Phys. **110**, 4986–4991 (1999).
[21]M. Swart and F. Matthias Bickelhaupt, "Optimization of strong and weak coordinates," Int. J. Quantum Chem. **106**, 2536–2544 (2006).
[22]M. Swart and F. M. Bickelhaupt, "QUILD: QUantum-regions interconnected by local descriptions," J. Comput. Chem. **29**, 724–734 (2008).
[23]M. Bonomi, D. Branduardi, G. Bussi, C. Camilloni, D. Provasi, P. Raiteri, D. Donadio, F. Marinelli, F. Pietrucci, R. A. Broglia, and M. Parrinello, "PLUMED: A portable plugin for free-energy calculations with molecular dynamics," Comput. Phys. Commun. **180**, 1961–1972 (2009).
[24]S. Grimme, "Exploration of chemical compound, conformer, and reaction space with meta-dynamics simulations based on tight-binding quantum chemical calculations," J. Chem. Theory Comput. **15**, 2847–2862 (2019).
[25]D. Garay-Ruiz, J. Buils, N. A. G. Bandeira, S. Floquet, E. Cadot, and C. Bo, "Thinking about the box: Exploring the electronic structure of a cuboidal-shaped Mo_{84} anionic nanocapsule," Inorg. Chem. **64**, 2716–2722 (2025).
[26]D. E. Ellis, "Application of diophantine integration to Hartree–Fock and configuration interaction calculations," Int. J. Quantum Chem. **2**, 35–42 (2009).
[27]D. E. Ellis and G. S. Painter, "Discrete variational method for the energy-band problem with general crystal potentials," Phys. Rev. B **2**, 2887–2898 (1970).
[28]P. M. Boerrigter, G. te Velde, and J. E. Baerends, "Three-dimensional numerical integration for electronic structure calculations," Int. J. Quantum Chem. **33**, 87–113 (1988).
[29]G. te Velde and E. J. Baerends, "Numerical integration for polyatomic systems," J. Comput. Phys. **99**, 84–98 (1992).
[30]C. Fonseca Guerra, J.-W. Handgraaf, E. J. Baerends, and F. M. Bickelhaupt, "Voronoi deformation density (VDD) charges: Assessment of the Mulliken, Bader, Hirshfeld, Weinhold, and VDD methods for charge analysis," J. Comput. Chem. **25**, 189–210 (2004).
[31]M. Franchini, P. H. T. Philipsen, and L. Visscher, "The Becke fuzzy cells integration scheme in the Amsterdam density functional program suite," J. Comput. Chem. **34**, 1819–1827 (2013).
[32]A. D. Becke, "A multicenter numerical integration scheme for polyatomic molecules," J. Chem. Phys. **88**, 2547–2553 (1988).
[33]M. Güell, J. M. Luis, M. Solà, and M. Swart, "Importance of the basis set for the spin state energetics of iron complexes," J. Phys. Chem. A **112**, 6384–6391 (2008).
[34]G. te Velde, F. M. Bickelhaupt, E. J. Baerends, C. Fonseca Guerra, S. J. A. van Gisbergen, J. G. Snijders, and T. Ziegler, "Chemistry with ADF," J. Comput. Chem. **22**, 931–967 (2001).
[35]E. Spadetto, P. H. T. Philipsen, A. Förster, and L. Visscher, "Toward pair atomic density fitting for correlation energies with benchmark accuracy," J. Chem. Theory Comput. **19**, 1499–1516 (2023).
[36]E. Van Lenthe and E. J. Baerends, "Optimized Slater-type basis sets for the elements 1–118," J. Comput. Chem. **24**, 1142–1156 (2003).

[37]M. Franchini, P. H. T. Philipsen, E. van Lenthe, and L. Visscher, "Accurate Coulomb potentials for periodic and molecular systems through density fitting," J. Chem. Theory Comput. **10**, 1994–2004 (2014).
[38]F. L. Hirshfeld, "Bonded-atom fragments for describing molecular charge densities," Theor. Chim. Acta **44**, 129–138 (1977).
[39]B. Delley, "An all-electron numerical method for solving the local density functional for polyatomic molecules," J. Chem. Phys. **92**, 508–517 (1990).
[40]V. I. Lebedev, "Quadratures on a sphere," USSR Comput. Math. Math. Phys. **16**, 10–24 (1976).
[41]H. Sambe and R. H. Felton, "A new computational approach to Slater's SCF–$X\alpha$ equation," J. Chem. Phys. **62**, 1122–1126 (1975).
[42]B. I. Dunlap, J. W. D. Connolly, and J. R. Sabin, "On some approximations in applications of $X\alpha$ theory," J. Chem. Phys. **71**, 3396–3402 (1979).
[43]R. B. Murphy, Y. Cao, M. D. Beachy, M. N. Ringnalda, and R. A. Friesner, "Efficient pseudospectral methods for density functional calculations," J. Chem. Phys. **112**, 10131–10141 (2000).
[44]M. Sierka, A. Hogekamp, and R. Ahlrichs, "Fast evaluation of the Coulomb potential for electron densities using multipole accelerated resolution of identity approximation," J. Chem. Phys. **118**, 9136–9148 (2003).
[45]M. A. Watson, N. C. Handy, and A. J. Cohen, "Density functional calculations, using Slater basis sets, with exact exchange," J. Chem. Phys. **119**, 6475–6481 (2003).
[46]A. Sodt, J. E. Subotnik, and M. Head-Gordon, "Linear scaling density fitting," J. Chem. Phys. **125**, 194109 (2006).
[47]A. Sodt and M. Head-Gordon, "Hartree-Fock exchange computed using the atomic resolution of the identity approximation," J. Chem. Phys. **128**, 104106 (2008).
[48]A. C. Ihrig, J. Wieferink, I. Y. Zhang, M. Ropo, X. Ren, P. Rinke, M. Scheffler, and V. Blum, "Accurate localized resolution of identity approach for linear-scaling hybrid density functionals and for many-body perturbation theory," New J. Phys. **17**, 093020 (2015).
[49]D. S. Hollman, H. F. Schaefer, and E. F. Valeev, "Semi-exact concentric atomic density fitting: Reduced cost and increased accuracy compared to standard density fitting," J. Chem. Phys. **140**, 064109 (2014).
[50]D. S. Hollman, H. F. Schaefer, and E. F. Valeev, "Fast construction of the exchange operator in an atom-centred basis with concentric atomic density fitting," Mol. Phys. **115**, 2065–2076 (2017).
[51]M. Krykunov, T. Ziegler, and E. v. Lenthe, "Hybrid density functional calculations of nuclear magnetic shieldings using Slater-type orbitals and the zeroth-order regular approximation," Int. J. Quantum Chem. **109**, 1676–1683 (2009).
[52]E. Rebolini, R. Izsák, S. S. Reine, T. Helgaker, and T. B. Pedersen, "Comparison of three efficient approximate exact-exchange algorithms: The chain-of-spheres algorithm, pair-atomic resolution-of-the-identity method, and auxiliary density matrix method," J. Chem. Theory Comput. **12**, 3514–3522 (2016).
[53]P. Lin, X. Ren, and L. He, "Accuracy of localized resolution of the identity in periodic hybrid functional calculations with numerical atomic orbitals," J. Phys. Chem. Lett. **11**, 3082–3088 (2020).
[54]P. Lin, X. Ren, and L. He, "Efficient hybrid density functional calculations for large periodic systems using numerical atomic orbitals," J. Chem. Theory Comput. **17**, 222–239 (2021).
[55]R. Shi, P. Lin, M. Y. Zhang, L. He, and X. Ren, "Subquadratic-scaling real-space random phase approximation correlation energy calculations for periodic systems with numerical atomic orbitals," Phys. Rev. B **109**, 035103 (2024).
[56]F. Aquilante, T. B. Pedersen, and R. Lindh, "Low-cost evaluation of the exchange Fock matrix from Cholesky and density fitting representations of the electron repulsion integrals," J. Chem. Phys. **126**, 194106 (2007).
[57]A. Förster, M. Franchini, E. van Lenthe, and L. Visscher, "A quadratic pair atomic resolution of the identity based SOS-AO-MP2 algorithm using Slater type orbitals," J. Chem. Theory Comput. **16**, 875–891 (2020).
[58]L. N. Wirz, S. S. Reine, and T. B. Pedersen, "On resolution-of-the-identity electron repulsion integral approximations and variational stability," J. Chem. Theory Comput. **13**, 4897–4906 (2017).
[59]P. Merlot, T. Kjærgaard, T. Helgaker, R. Lindh, F. Aquilante, S. Reine, and T. B. Pedersen, "Attractive electron-electron interactions within robust local fitting approximations," J. Comput. Chem. **34**, 1486–1496 (2013).
[60]X. Ren, P. Rinke, V. Blum, J. Wieferink, A. Tkatchenko, A. Sanfilippo, K. Reuter, and M. Scheffler, "Resolution-of-identity approach to Hartree–Fock, hybrid density functionals, RPA, MP2 and *GW* with numeric atom-centered orbital basis functions," New J. Phys. **14**, 053020 (2012).
[61]B. I. Dunlap, "Robust and variational fitting: Removing the four-center integrals from center stage in quantum chemistry," J. Mol. Struct.: THEOCHEM **529**, 37–40 (2000).
[62]U. Ekström, L. Visscher, R. Bast, A. J. Thorvaldsen, and K. Ruud, "Arbitrary-order density functional response theory from automatic differentiation," J. Chem. Theory Comput. **6**, 1971–1980 (2010).
[63]S. Lehtola, C. Steigemann, M. J. T. Oliveira, and M. A. L. Marques, "Recent developments in libxc—A comprehensive library of functionals for density functional theory," SoftwareX **7**, 1–5 (2018).
[64]S. Grimme, J. Antony, S. Ehrlich, and H. Krieg, "A consistent and accurate *ab initio* parametrization of density functional dispersion correction (DFT-D) for the 94 elements H-Pu," J. Chem. Phys. **132**, 154104 (2010).
[65]E. Caldeweyher, S. Ehlert, A. Hansen, H. Neugebauer, S. Spicher, C. Bannwarth, and S. Grimme, "A generally applicable atomic-charge dependent London dispersion correction," J. Chem. Phys. **150**, 154122 (2019).
[66]S. Grimme, "Semiempirical hybrid density functional with perturbative second-order correlation," J. Chem. Phys. **124**, 034108 (2006).
[67]A. Förster and L. Visscher, "Double hybrid DFT calculations with Slater type orbitals," J. Comput. Chem. **41**, 1660–1684 (2020).
[68]E. G. Hohenstein, R. M. Parrish, and T. J. Martínez, "Tensor hypercontraction density fitting. I. Quartic scaling second- and third-order Møller–Plesset perturbation theory," J. Chem. Phys. **137**, 1085 (2012).
[69]R. M. Parrish, E. G. Hohenstein, T. J. Martínez, and C. D. Sherrill, "Tensor hypercontraction. II. Least-squares renormalization," J. Chem. Phys. **137**, 224106 (2012).
[70]S. Kozuch, D. Gruzman, and J. M. L. Martin, "DSD-BLYP: A general purpose double hybrid density functional including spin component scaling and dispersion correction," J. Phys. Chem. C **114**, 20801–20808 (2010).
[71]S. Kozuch and J. M. L. Martin, "DSD-PBEP86: In search of the best double-hybrid DFT with spin-component scaled MP2 and dispersion corrections," Phys. Chem. Chem. Phys. **13**, 20104–20107 (2011).
[72]S. Kozuch and J. M. L. Martin, "Spin-component-scaled double hybrids: An extensive search for the best fifth-rung functionals blending DFT and perturbation theory," J. Comput. Chem. **34**, 2327–2344 (2013).
[73]G. Santra, N. Sylvetsky, and J. M. L. Martin, "Minimally empirical double-hybrid functionals trained against the GMTKN55 database: RevDSD-PBEP86-D4, revDOD-PBE-D4, and DOD-SCAN-D4," J. Phys. Chem. A **123**, 5129–5143 (2019).
[74]A. Najibi and L. Goerigk, "DFT-D4 counterparts of leading meta-generalized-gradient approximation and hybrid density functionals for energetics and geometries," J. Comput. Chem. **41**, 2562–2572 (2020).
[75]D. C. Langreth and J. P. Perdew, "The exchange-correlation energy of a metallic surface," Solid State Commun. **17**, 1425–1429 (1975).
[76]D. C. Langreth and J. P. Perdew, "Exchange-correlation energy of a metallic surface: Wave-vector analysis," Phys. Rev. B **15**, 2884–2901 (1977).
[77]E. Engel and R. M. Dreizler, "From explicit to implicit density functionals," J. Comput. Chem. **20**, 31–50 (1999).
[78]A. Görling, "Orbital- and state-dependent functionals in density-functional theory," J. Chem. Phys. **123**, 062203 (2005).
[79]S. Kümmel and L. Kronik, "Orbital-dependent density functionals: Theory and applications," Rev. Mod. Phys. **80**, 3–60 (2008).
[80]A. Görling, "Hierarchies of methods towards the exact Kohn–Sham correlation energy based on the adiabatic-connection fluctuation-dissipation theorem," Phys. Rev. B **99**, 235120 (2019).
[81]B. D. Nguyen, G. P. Chen, M. M. Agee, A. M. Burow, M. P. Tang, and F. Furche, "Divergence of many-body perturbation theory for noncovalent interactions of large molecules," J. Chem. Theory Comput. **16**, 2258–2273 (2020).
[82]A. Heßelmann and A. Görling, "Random-phase approximation correlation methods for molecules and solids," Mol. Phys. **109**, 2473–2500 (2011).
[83]H. Eshuis, J. E. Bates, and F. Furche, "Electron correlation methods based on the random phase approximation," Theor. Chem. Acc. **131**, 1084 (2012).

[84]X. Ren, P. Rinke, C. Joas, and M. Scheffler, "Random-phase approximation and its applications in computational chemistry and materials science," J. Mater. Sci. **47**, 7447–7471 (2012).
[85]G. P. Chen, V. K. Voora, M. M. Agee, S. G. Balasubramani, and F. Furche, "Random-phase approximation methods," Annu. Rev. Phys. Chem. **68**, 421–445 (2017).
[86]T. M. Henderson and G. E. Scuseria, "The connection between self-interaction and static correlation: A random phase approximation perspective," Mol. Phys. **108**, 2511–2517 (2010).
[87]J. Paier, X. Ren, P. Rinke, G. E. Scuseria, A. Grüneis, G. Kresse, and M. Scheffler, "Assessment of correlation energies based on the random-phase approximation," New J. Phys. **14**, 043002 (2012).
[88]X. Ren, P. Rinke, G. E. Scuseria, and M. Scheffler, "Renormalized second-order perturbation theory for the electron correlation energy: Concept, implementation, and benchmarks," Phys. Rev. B **88**, 035120 (2013).
[89]J. E. Bates and F. Furche, "Communication: Random phase approximation renormalized many-body perturbation theory," J. Chem. Phys. **139**, 171103 (2013).
[90]J. Harl and G. Kresse, "Cohesive energy curves for noble gas solids calculated by adiabatic connection fluctuation-dissipation theory," Phys. Rev. B **77**, 045136 (2008).
[91]J. Harl and G. Kresse, "Accurate bulk properties from approximate many-body techniques," Phys. Rev. Lett. **103**, 056401 (2009).
[92]S. Lebègue, J. Harl, T. Gould, J. G. Ángyán, G. Kresse, and J. F. Dobson, "Cohesive properties and asymptotics of the dispersion interaction in graphite by the random phase approximation," Phys. Rev. Lett. **105**, 196401 (2010).
[93]X. Ren, F. Merz, H. Jiang, Y. Yao, M. Rampp, H. Lederer, V. Blum, and M. Scheffler, "All-electron periodic G_0W_0 implementation with numerical atomic orbital basis functions: Algorithm and benchmarks," Phys. Rev. Mater. **5**, 013807 (2021).
[94]G. Jansen, R. F. Liu, and J. G. Ángyán, "On the equivalence of ring-coupled cluster and adiabatic connection fluctuation-dissipation theorem random phase approximation correlation energy expressions," J. Chem. Phys. **133**, 154106 (2010).
[95]J. G. Ángyán, R. F. Liu, J. Toulouse, and G. Jansen, "Correlation energy expressions from the adiabatic-connection fluctuation-dissipation theorem approach," J. Chem. Theory Comput. **7**, 3116–3130 (2011).
[96]T. Olsen, C. E. Patrick, J. E. Bates, A. Ruzsinszky, and K. S. Thygesen, "Beyond the RPA and GW methods with adiabatic xc-kernels for accurate ground state and quasiparticle energies," npj Comput. Mater. **5**, 106 (2019).
[97]A. Förster, "Assessment of the second-order statically screened exchange correction to the random phase approximation for correlation energies," J. Chem. Theory Comput. **18**, 5948–5965 (2022).
[98]J. Erhard, P. Bleiziffer, and A. Görling, "Power series approximation for the correlation kernel leading to Kohn–Sham methods combining accuracy, computational efficiency, and general applicability," Phys. Rev. Lett. **117**, 143002 (2016).
[99]E. Trushin, A. Thierbach, and A. Görling, "Toward chemical accuracy at low computational cost: Density-functional theory with σ-functionals for the correlation energy," J. Chem. Phys. **154**, 014104 (2021).
[100]S. Fauser, E. Trushin, C. Neiss, and A. Görling, "Chemical accuracy with σ-functionals for the Kohn–Sham correlation energy optimized for different input orbitals and eigenvalues," J. Chem. Phys. **155**, 134111 (2021).
[101]J. Erhard, S. Fauser, E. Trushin, and A. Görling, "Scaled σ-functionals for the Kohn–Sham correlation energy with scaling functions from the homogeneous electron gas," J. Chem. Phys. **157**, 114105 (2022).
[102]D. Dhingra, A. Shori, and A. Förster, "Chemically accurate singlet-triplet gaps of organic chromophores and linear acenes by the random phase approximation and σ-functionals," J. Chem. Phys. **159**, 194105 (2023).
[103]S. Fauser, A. Förster, L. Redeker, C. Neiss, J. Erhard, E. Trushin, and A. Görling, "Basis set requirements of σ-functionals for Gaussian- and slater-type basis functions and comparison with range-separated hybrid and double hybrid functionals," J. Chem. Theory Comput. **20**, 2404–2422 (2024).
[104]S. Fauser, V. Drontschenko, C. Ochsenfeld, and A. Görling, "Accurate NMR shieldings with σ-functionals," J. Chem. Theory Comput. **20**, 6028–6036 (2024).
[105]D. Golze, M. Dvorak, and P. Rinke, "The *GW* compendium: A practical guide to theoretical photoemission spectroscopy," Front. Chem. **7**, 377 (2019).
[106]J. W. Knight, X. Wang, L. Gallandi, O. Dolgounitcheva, X. Ren, J. V. Ortiz, P. Rinke, T. Körzdörfer, and N. Marom, "Accurate ionization potentials and electron affinities of acceptor molecules III: A benchmark of GW methods," J. Chem. Theory Comput. **12**, 615–626 (2016).
[107]F. Bruneval, N. Dattani, and M. J. van Setten, "The GW miracle in many-body perturbation theory for the ionization potential of molecules," Front. Chem. **9**, 749779 (2021).
[108]C. A. McKeon, S. M. Hamed, F. Bruneval, and J. B. Neaton, "An optimally tuned range-separated hybrid starting point for ab initio GW plus Bethe–Salpeter equation calculations of molecules," J. Chem. Phys. **157**, 074103 (2022).
[109]A. Marie and P. F. Loos, "Reference energies for valence ionizations and satellite transitions," J. Chem. Theory Comput. **20**, 4751–4777 (2024).
[110]E. E. Salpeter and H. A. Bethe, "A relativistic equation for bound-state problems," Phys. Rev. **84**, 1232–1242 (1951).
[111]A. Förster and L. Visscher, "Low-Order scaling G_0W_0 by pair atomic density fitting," J. Chem. Theory Comput. **16**, 7381–7399 (2020).
[112]A. Förster and L. Visscher, "GW100: A slater-type orbital perspective," J. Chem. Theory Comput. **17**, 5080–5097 (2021).
[113]A. Förster and L. Visscher, "Low-Order scaling quasiparticle self-consistent GW for molecules," Front. Chem. **9**, 736591 (2021).
[114]A. Förster and L. Visscher, "Quasiparticle self-consistent *GW*-Bethe–Salpeter equation calculations for large chromophoric systems," J. Chem. Theory Comput. **18**, 6779–6793 (2022).
[115]A. Förster, E. van Lenthe, E. Spadetto, and L. Visscher, "Two-component *GW* calculations: Cubic scaling implementation and comparison of partially self-consistent variants," J. Chem. Theory Comput. **19**, 5958–5976 (2023).
[116]F. Bruneval and A. Förster, "Fully dynamic *G*3*W*2 self-energy for finite systems: Formulas and benchmark," J. Chem. Theory Comput. **20**, 3218–3230 (2024).
[117]A. Förster and L. Visscher, "Exploring the statically screened G_3W_2 correction to the *GW* self-energy: Charged excitations and total energies of finite systems," Phys. Rev. B **105**, 125121 (2022).
[118]A. Förster and F. Bruneval, "Why does the *GW* approximation give accurate quasiparticle energies? The cancellation of vertex corrections quantified," J. Phys. Chem. Lett. **15**, 12526–12534 (2024).
[119]A. Förster, "Beyond quasi-particle self-consistent *GW* for molecules with vertex corrections," J. Chem. Theory Comput. **21**, 1709–1721 (2025).
[120]H. N. Rojas, R. W. Godby, and R. J. Needs, "Space-time method for *ab initio* calculations of self-energies and dielectric response functions of solids," Phys. Rev. Lett. **74**, 1827–1831 (1995).
[121]M. M. Rieger, L. Steinbeck, I. D. White, H. N. Rojas, and R. W. Godby, "The *GW* space-time method for the self-energy of large systems," Comput. Phys. Commun. **117**, 211–228 (1999).
[122]P. Liu, M. Kaltak, J. Klimeš, and G. Kresse, "Cubic scaling GW: Towards fast quasiparticle calculations," Phys. Rev. B **94**, 165109 (2016).
[123]J. Wilhelm, D. Golze, L. Talirz, J. Hutter, and C. A. Pignedoli, "Toward *GW* calculations on thousands of atoms," J. Phys. Chem. Lett. **9**, 306–312 (2018).
[124]J. Wilhelm, P. Seewald, and D. Golze, "Low-scaling *GW* with benchmark accuracy and application to phosphorene nanosheets," J. Chem. Theory Comput. **17**, 1662–1677 (2021).
[125]I. Duchemin and X. Blase, "Cubic-Scaling all-electron *GW* calculations with a separable density-fitting space–time approach," J. Chem. Theory Comput. **17**, 2383–2393 (2021).
[126]M. Kaltak, J. Klimeš, and G. Kresse, "Low scaling algorithms for the random phase approximation: Imaginary time and laplace transformations," J. Chem. Theory Comput. **10**, 2498–2507 (2014).
[127]F. Bruneval, "Ionization energy of atoms obtained from *GW* self-energy or from random phase approximation total energies," J. Chem. Phys. **136**, 194107 (2012).
[128]M. J. Van Setten, F. Weigend, and F. Evers, "The *GW*-method for quantum chemistry applications: Theory and implementation," J. Chem. Theory Comput. **9**, 232–246 (2013).
[129]S. Lebègue, B. Arnaud, M. Alouani, and P. E. Bloechl, "Implementation of an all-electron GW approximation based on the projector augmented wave method

without plasmon pole approximation: Application to Si, SiC, AlAs, InAs, NaH, and KH," Phys. Rev. B **67**, 155208 (2003).
[130]M. S. Hybertsen and S. G. Louie, "First-principles theory of quasiparticles: Calculation of band gaps in semiconductors and insulators," Phys. Rev. Lett. **55**, 1418–1421 (1985).
[131]M. S. Hybertsen and S. G. Louie, "Electron correlation in semiconductors and insulators: Band gaps and quasiparticle energies," Phys. Rev. B **34**, 5390 (1986).
[132]S. V. Faleev, M. van Schilfgaarde, and T. Kotani, "All-electron self-consistent *GW* approximation: Application to Si, MnO, and NiO," Phys. Rev. Lett. **93**, 126406 (2004).
[133]M. van Schilfgaarde, T. Kotani, and S. Faleev, "Quasiparticle self-consistent *GW* theory," Phys. Rev. Lett. **96**, 226402 (2006).
[134]T. Kotani, M. van Schilfgaarde, and S. V. Faleev, "Quasiparticle self-consistent *GW* method: A basis for the independent-particle approximation," Phys. Rev. B **76**, 165106 (2007).
[135]X. Gui, C. Holzer, and W. Klopper, "Accuracy assessment of *GW* starting points for calculating molecular excitation energies using the Bethe–Salpeter formalism," J. Chem. Theory Comput. **14**, 2127–2136 (2018).
[136]D. Golze, J. Wilhelm, M. J. Van Setten, and P. Rinke, "Core-level binding energies from *GW*: An efficient full-frequency approach within a localized basis," J. Chem. Theory Comput. **14**, 4856–4869 (2018).
[137]M. J. Van Setten, R. Costa, F. Viñes, and F. Illas, "Assessing *GW* approaches for predicting core level binding energies," J. Chem. Theory Comput. **14**, 877–883 (2018).
[138]D. Golze, L. Keller, and P. Rinke, "Accurate absolute and relative core-level binding energies from *GW*," J. Phys. Chem. Lett. **11**, 1840–1847 (2020).
[139]R. L. Panadés-Barrueta and D. Golze, "Accelerating core-level *GW* calculations by combining the contour deformation approach with the analytic continuation of *W*," J. Chem. Theory Comput. **19**, 5450–5464 (2023).
[140]F. Bruneval, T. Rangel, S. M. Hamed, M. Shao, C. Yang, and J. B. Neaton, "MOLGW 1: Many-body perturbation theory software for atoms, molecules, and clusters," Comput. Phys. Commun. **208**, 149–161 (2016).
[141]M. L. Tiago and J. R. Chelikowsky, "Optical excitations in organic molecules, clusters, and defects studied by first-principles Green's function methods," Phys. Rev. B **73**, 205334 (2006).
[142]A. Marie and P.-F. Loos, "A similarity renormalization group approach to Green's function methods," J. Chem. Theory Comput. **19**, 3943–3957 (2023).
[143]V. Vlček, "Stochastic vertex corrections: Linear scaling methods for accurate quasiparticle energies," J. Chem. Theory Comput. **15**, 6254–6266 (2019).
[144]C. H. Patterson, "Molecular ionization energies from GW and Hartree–Fock theory: Polarizability, screening, and self-energy vertex corrections," J. Chem. Theory Comput. **20**, 7479–7493 (2024).
[145]S. Vacondio, D. Varsano, A. Ruini, and A. Ferretti, "Going beyond the GW approximation using the time-dependent Hartree–Fock vertex," J. Chem. Theory Comput. **20**, 4718–4737 (2024).
[146]K. Morokuma, "Molecular orbital studies of hydrogen bonds. III. C=O···H–O hydrogen bond in $H_2CO\cdots H_2O$ and $H_2CO\cdots 2H_2O$," J. Chem. Phys. **55**, 1236 (1971).
[147]K. Kitaura and K. Morokuma, "A new energy decomposition scheme for molecular interactions within the Hartree–Fock approximation," Int. J. Quantum Chem. **10**, 325 (1976).
[148]K. Morokuma, "Why do molecules interact? The origin of electron donor–acceptor complexes, huydrogen bonding and proton affinity," Acc. Chem. Res. **10**, 294–300 (1977).
[149]T. Ziegler and A. Rauk, "On the calculation of bonding energies by the Hartree Fock Slater method: I. The transition state method," Theor. Chim. Acta **46**, 1–10 (1977).
[150]T. Ziegler and A. Rauk, "CO,CS,N_2, PF_3 and $CNCH_3$ as σ donors and π acceptors. A theoretical study by the Hartree–Fock–Slater transition state method," Inorg. Chem. **18**, 1755–1759 (1979).
[151]F. M. Bickelhaupt, N. M. M. Nibbering, E. M. van Wezenbeek, and E. J. Baerends, "Central bond in the three CN.cntdot.dimers NC-CN, CN-CN and CN-NC: Electron pair bonding and Pauli repulsion effects," J. Phys. Chem. **96**, 4864–4873 (1992).
[152]F. M. Bickelhaupt and E. J. Baerends, in *Reviews in Computational Chemistry*, edited by K. B. Lipkowitz and D. B. Boyd (Wiley-VCH, New York, 2000), Chap. 1, Vol. 15, pp. 1–86.
[153]E. J. Baerends and A. Rozendaal, in *Analysis of σ-Bonding, π-(back)Bonding and The Synergic Effect in Cr(CO)$_6$, NATO ASI Series C*, edited by A. Veillard (D. Reidel Publishing Company, 1986), Vol. 176, pp. 159–177.
[154]P. S. Bagus, K. Hermann, and C. W. Bauschlicher, Jr., "Model studies of Al_4CO and Al_4NH_3," J. Chem. Phys. **80**, 4378–4386 (1984).
[155]F. M. Bickelhaupt, "Understanding reactivity with Kohn–Sham molecular orbital theory: E2–S_N2 mechanistic spectrum and other concepts," J. Comput. Chem. **20**, 114–128 (1999).
[156]I. Fernández and F. M. Bickelhaupt, "The activation strain model and molecular orbital theory: Understanding and designing chemical reactions," Chem. Soc. Rev. **43**, 4953–4967 (2014).
[157]F. M. Bickelhaupt and K. N. Houk, "Analyzing reaction rates with the distortion/interaction-activation strain model," Angew. Chem., Int. Ed. **56**, 10070–10086 (2017).
[158]W.-J. van Zeist, A. H. Koers, L. P. Wolters, and F. M. Bickelhaupt, "Reaction coordinates and the transition-vector approximation to the IRC," J. Chem. Theory Comput. **4**, 920–928 (2008).
[159]W. V. Zeist *et al.*, "PyFrag—Streamlining your reaction path analysis," J. Comput. Chem. **29**, 312–315 (2008).
[160]X. Sun, T. M. Soini, J. Poater, T. A. Hamlin, and F. M. Bickelhaupt, "PyFrag 2019—Automating the exploration and analysis of reaction mechanisms," J. Comput. Chem. **40**, 2227–2233 (2019).
[161]T. Ziegler and A. Rauk, "A theoretical study of the ethylene-metal bond in complexes between Cu^+, Ag^+, Au^+, Pt(0) or Pt(2+) and ethylene, based on the Hartree-Fock-Slater transition-state method," Inorg. Chem. **1558–1565**, 1558–1565 (1979).
[162]D. Post and E. J. Baerends, "Cluster studies of CO adsorption. III. CO on small Cu clusters," J. Chem. Phys. **78**, 5663 (1983).
[163]T. Ziegler, V. Tschinke, and C. Ursenbach, "Thermal stability and kinetic lability of the metal-carbonyl bond. A theoretical study on $M(CO)_6$ (M=Cr, Mo, W), $M(CO)_5$ (M=Fe, Ru, Os) and $M(CO)_4$ (M=Ni, Pd, Pt)," J. Am. Chem. Soc. **109**, 4825–4837 (1987).
[164]K. L. Kunze and E. R. Davidson, "Energetics and electronic structure of chromium hexacarbonyl," J. Phys. Chem. **96**, 2129–2141 (1992).
[165]C. Fonseca Guerra *et al.*, "Hydrogen bonding in DNA base Pairs: reconciliation of theory and experiment," J. Am. Chem. Soc. **122**, 4117–4128 (2000).
[166]L. P. Wolters and F. M. Bickelhaupt, "The activation strain model and molecular orbital theory," Wiley Interdiscip. Rev.: Comput. Mol. Sci. **5**, 324–343 (2015).
[167]G. Frenking, I. Fernandez, N. Holzmann, S. Pan, I. Krossing, and M. Zhou, "Metal-CO bonding in mononuclear transition metal carbonyl complexes," J. Am. Chem. Soc. Au **1**, 623–645 (2021).
[168]M. Mitoraj and A. Michalak, "Natural orbitals for chemical valence as descriptors of chemical bonding in transition metal complexes," J. Mol. Model. **13**, 347–355 (2007).
[169]M. Mitoraj and A. Michalak, "Donor–Acceptor properties of ligands from the natural orbitals for chemical valence," Organometallics **26**, 6576–6580 (2007).
[170]A. Michalak, M. Mitoraj, and T. Ziegler, "Bond orbitals from chemical valence theory," J. Phys. Chem. A **112**, 1933–1939 (2008).
[171]M. P. Mitoraj, A. Michalak, and T. Ziegler, "A combined charge and energy decomposition scheme for bond analysis," J. Chem. Theory Comput. **5**, 962–975 (2009).
[172]C. Nieuwland, P. Vermeeren, F. M. Bickelhaupt, and C. Fonseca Guerra, "Understanding chemistry with thesymmetry-decomposed voronoi deformation density charge analysis," J. Comput. Chem. **44**, 2108–2119 (2023).
[173]J. I. Rodríguez, "An efficient method for computing the QTAIM topology of a scalar field: The electron density case," J. Comput. Chem. **34**, 681–686 (2013).
[174]P. W. Ayers and S. Jenkins, "Bond metallicity measures," Comput. Theor. Chem. **1053**, 112–122 (2015), a part of Special Issue: Understanding structure and reactivity from topology and beyond.

[175]V. Tognetti and L. Joubert, "Density functional theory and Bader's atoms-in-molecules theory: Towards a vivid dialogue," Phys. Chem. Chem. Phys. **16**, 14539–14550 (2014).
[176]Y. A. Abramov, "On the possibility of kinetic energy density evaluation from the experimental electron-density distribution," Acta Crystallogr., Sect. A:Found. Adv. **53**, 264–272 (1997).
[177]G. Hoffmann, V. Tognetti, and L. Joubert, "Can molecular and atomic descriptors predict the electrophilicity of Michael acceptors?," J. Mol. Model. **24**, 281–5023 (2018).
[178]R. G. Parr, L. v. Szentpály, and S. Liu, "Electrophilicity index," J. Am. Chem. Soc. **121**, 1922–1924 (1999).
[179]P. W. Ayers, J. S. M. Anderson, J. I. Rodriguez, and Z. Jawed, "Indices for predicting the quality of leaving groups," Phys. Chem. Chem. Phys. **7**, 1918–1925 (2005).
[180]J. L. Gázquez, A. Cedillo, and A. Vela, "Electrodonating and electroaccepting powers," J. Phys. Chem. A **111**, 1966–1970 (2007).
[181]M. D. Newton, "Quantum chemical probes of electron-transfer kinetics: The nature of donor–acceptor interactions," Chem. Rev. **91**, 767–792 (1991).
[182]K. Senthilkumar, F. C. Grozema, F. M. Bickelhaupt, and L. D. A. Siebbeles, "Charge transport in columnar stacked triphenylenes: Effects of conformational fluctuations on charge transfer integrals and site energies," J. Chem. Phys. **119**, 9809–9817 (2003).
[183]K. Senthilkumar, F. C. Grozema, C. F. Guerra, F. M. Bickelhaupt, F. D. Lewis, Y. A. Berlin, M. A. Ratner, and L. D. A. Siebbeles, "Absolute rates of hole transfer in DNA," J. Am. Chem. Soc. **127**, 14894–14903 (2005).
[184]L. Visscher and E. van Lenthe, "On the distinction between scalar and spin–orbit relativistic effects," Chem. Phys. Lett. **306**, 357–365 (1999).
[185]A. j. Sadlej and J. g. Snijders, "Spin separation in the regular Hamiltonian approach to solutions of the Dirac equation," Chem. Phys. Lett. **229**, 435–438 (1994).
[186]E. van Lenthe, R. van Leeuwen, E. J. Baerends, and J. G. Snijders, "Relativistic regular two-component Hamiltonians," Int. J. Quantum Chem. **57**, 281–293 (1996).
[187]K. G. Dyall, "An exact separation of the spin-free and spin-dependent terms of the Dirac–Coulomb–Breit Hamiltonian," J. Chem. Phys. **100**, 2118–2127 (1994).
[188]W. Kutzelnigg and W. Liu, "Quasirelativistic theory equivalent to fully relativistic theory," J. Chem. Phys. **123**, 241102 (2005).
[189]L. Visscher and K. g. Dyall, "Dirac–Fock atomic electronic structure calculations using different nuclear charge distributions," At. Data Nucl. Data Tables **67**, 207–224 (1997).
[190]J. Autschbach, "Magnitude of finite-nucleus-size effects in relativistic density functional computations of indirect NMR nuclear spin–spin coupling constants," ChemPhysChem **10**, 2274–2283 (2009).
[191]J. Autschbach and T. Ziegler, "Double perturbation theory: A powerful tool in computational coordination chemistry," Coord. Chem. Rev. **238–239**, 83–126 (2003).
[192]S. J. A. van Gisbergen, J. G. Snijders, and E. J. Baerends, "Implementation of time-dependent density functional response equations," Comput. Phys. Commun. **118**, 119–138 (1999).
[193]D. Jacquemin, V. Wathelet, E. A. Perpète, and C. Adamo, "Extensive TD-DFT benchmark: Singlet excited states of organic molecules," J. Chem. Theor. Comp. **5**, 2420–2435 (2009).
[194]D. Jacquemin, A. Planchat, C. Adamo, and B. Mennucci, "TD-DFT assessment of functionals for optical 0–0 transitions in solvated dyes," J. Chem. Theory Comput. **8**, 2359–2372 (2012).
[195]A. D. Laurent and D. Jacquemin, "TD-DFT benchmarks: A review," Int. J. Quantum Chem. **113**, 2019–2039 (2013).
[196]O. V. Gritsenko, Ł. M. Mentel, and E. J. Baerends, "On the errors of local density (LDA) and generalized gradient (GGA) approximations to the Kohn–Sham potential and orbital energies," J. Chem. Phys. **144**, 204114 (2016).
[197]O. V. Gritsenko, P. R. T. Schipper, and E. J. Baerends, "Approximation of the exchange-correlation Kohn–Sham potential with a statistical average of different orbital model potentials," Chem. Phys. Lett. **302**, 199–207 (1999).
[198]O. V. Gritsenko, P. R. T. Schipper, and E. J. Baerends, "Ensuring proper short-range and asymptotic behavior of the exchange-correlation Kohn–Sham potential by modeling with a statistical average of different orbital model potentials," Int. J. Quant. Chem. **76**, 407–419 (2000).
[199]P. R. T. Schipper, O. V. Gritsenko, S. J. A. van Gisbergen, and E. J. Baerends, "Molecular calculations of excitation energies and (hyper)polarizabilities with a statistical average of orbital model exchange-correlation potentials," J. Chem. Phys. **112**, 1344 (2000).
[200]R. van Meer, O. V. Gritsenko, and E. J. Baerends, "Physical meaning of virtual Kohn–Sham orbitals and orbital energies: An ideal basis for the description of molecular excitations," J. Chem. Theory Comput. **10**, 4432–4441 (2014).
[201]F. Wang and T. Ziegler, "A simplified relativistic time-dependent density-functional theory formalism for the calculations of excitation energies including spin-orbit coupling effect," J. Chem. Phys. **123**, 154102 (2005).
[202]F. Wang, T. Ziegler, E. van Lenthe, S. van Gisbergen, and E. J. Baerends, "The calculation of excitation energies based on the relativistic two-component zeroth-order regular approximation and time-dependent density-functional with full use of symmetry," J. Chem. Phys. **122**, 204103 (2005).
[203]K. Mori, T. P. M. Goumans, E. van Lenthe, and F. Wang, "Predicting phosphorescent lifetimes and zero-field splitting of organometallic complexes with time-dependent density functional theory including spin–orbit coupling," Phys. Chem. Chem. Phys. **16**, 14523–14530 (2014).
[204]C. S. Chibueze and L. Visscher, "Restricted open-shell time-dependent density functional theory with perturbative spin–orbit coupling," J. Chem. Phys. **161**, 094112 (2024).
[205]S. Hirata and M. Head-Gordon, "Time-dependent density functional theory within the Tamm–Dancoff approximation," Chem. Phys. Lett. **314**, 291–299 (1999).
[206]C. Bannwarth and S. Grimme, "A simplified time-dependent density functional theory approach for electronic ultraviolet and circular dichroism spectra of very large molecules," Comput. Theor. Chem. **1040–1041**, 45–53 (2014), a part of Special Issue: Excited states: From isolated molecules to complex environments.
[207]S. Grimme, "A simplified Tamm-Dancoff density functional approach for the electronic excitation spectra of very large molecules," J. Chem. Phys. **138**, 244104 (2013).
[208]R. Rüger, E. van Lenthe, T. Heine, and L. Visscher, "Tight-binding approximations to time-dependent density functional theory—A fast approach for the calculation of electronically excited states," J. Chem. Phys. **144**, 184103 (2016).
[209]S. Havenridge, R. Rüger, and C. M. Aikens, "Analytical excited state gradients for time-dependent density functional theory plus tight binding (TDDFT + TB)," J. Chem. Phys. **158**, 224103 (2023).
[210]O. Baseggio, G. Fronzoni, and M. Stener, "A new time dependent density functional algorithm for large systems and plasmons in metal clusters," J. Chem. Phys. **143**, 024106 (2015).
[211]M. Medves, L. Sementa, D. Toffoli, G. Fronzoni, A. Fortunelli, and M. Stener, "An efficient hybrid scheme for time dependent density functional theory," J. Chem. Phys. **152**, 184104 (2020).
[212]O. Baseggio, D. Toffoli, G. Fronzoni, M. Stener, L. Sementa, and A. Fortunelli, "Extension of the time-dependent density functional complex polarizability algorithm to circular dichroism: Implementation and applications to Ag_8 and $Au_{38}(SC_2H_4C_6H_5)_{24}$," J. Phys. Chem. C **120**, 24335–24345 (2016).
[213]L. Sementa, G. Barcaro, O. Baseggio, M. De Vetta, A. Dass, E. Aprà, M. Stener, and A. Fortunelli, "Ligand-enhanced optical response of gold nanomolecules and its fragment projection analysis: The case of $Au_{30}(SR)_{18}$," J. Phys. Chem. C **121**, 10832–10842 (2017).
[214]S. Malola, L. Lehtovaara, J. Enkovaara, and H. Häkkinen, "Birth of the localized surface plasmon resonance in monolayer-protected gold nanoclusters," ACS Nano **7**, 10263–10270 (2013).
[215]S. Theivendran, L. Chang, A. Mukherjee, L. Sementa, M. Stener, A. Fortunelli, and A. Dass, "Principles of optical spectroscopy of aromatic alloy nanomolecules: $Au_{36-x}Ag_x(SPh\text{-}tBu)_{24}$," J. Phys. Chem. C **122**, 4524–4531 (2018).
[216]L. Chang, O. Baseggio, L. Sementa, D. Cheng, G. Fronzoni, D. Toffoli, E. Aprà, M. Stener, and A. Fortunelli, "Individual component map of rotatory strength and rotatory strength density plots as analysis tools of circular dichroism spectra of complex systems," J. Chem. Theory Comput. **14**, 3703–3714 (2018).
[217]A. J. Atkins, C. R. Jacob, and M. Bauer, "Probing the electronic structure of substituted ferrocenes with high-resolution XANES spectroscopy," Chem.–Eur. J. **18**, 7021–7025 (2012).

[218]A. J. Atkins, M. Bauer, and C. R. Jacob, "The chemical sensitivity of x-ray spectroscopy: High energy resolution XANES versus x-ray emission spectroscopy of substituted ferrocenes," Phys. Chem. Chem. Phys. **15**, 8095–8105 (2013).
[219]A. Boubnov, H. W. P. Carvalho, D. E. Doronkin, T. Günter, E. Gallo, A. J. Atkins, C. R. Jacob, and J.-D. Grunwaldt, "Selective catalytic reduction of NO over Fe-ZSM-5: Mechanistic insights by operando HERFD-XANES and valence-to-core x-ray emission spectroscopy," J. Am. Chem. Soc. **136**, 13006–13015 (2014).
[220]A. J. Atkins, M. Bauer, and C. R. Jacob, "High-resolution x-ray absorption spectroscopy of iron carbonyl complexes," Phys. Chem. Chem. Phys. **17**, 13937–13948 (2015).
[221]T. Günter, H. W. P. Carvalho, D. E. Doronkin, T. Sheppard, P. Glatzel, A. J. Atkins, J. Rudolph, C. R. Jacob, M. Casapu, and J.-D. Grunwaldt, "Structural snapshots of the SCR reaction mechanism on Cu-SSZ-13," Chem. Commun. **51**, 9227–9230 (2015).
[222]J. Rudolph and C. R. Jacob, "Revisiting the dependence of Cu K-edge x-ray absorption spectra on oxidation state and coordination environment," Inorg. Chem. **57**, 10591–10607 (2018).
[223]M. Stener, G. Fronzoni, and M. de Simone, "Time dependent density functional theory of core electrons excitations," Chem. Phys. Lett. **373**, 115–123 (2003).
[224]G. Fronzoni, M. Stener, P. Decleva, F. Wang, T. Ziegler, E. van Lenthe, and E. j. Baerends, "Spin–orbit relativistic time dependent density functional theory calculations for the description of core electron excitations: $TiCl_4$ case study," Chem. Phys. Lett. **416**, 56–63 (2005).
[225]N. Lee, T. Petrenko, U. Bergmann, F. Neese, and S. DeBeer, "Probing valence orbital composition with iron Kβ x-ray emission spectroscopy," J. Am. Chem. Soc. **132**, 9715–9727 (2010).
[226]S. Bernadotte, A. J. Atkins, and C. R. Jacob, "Origin-independent calculation of quadrupole intensities in x-ray spectroscopy," J. Chem. Phys. **137**, 204106 (2012).
[227]M. Rohlfing and S. G. Louie, "Excitonic effects and the optical absorption spectrum of hydrogenated Si clusters," Phys. Rev. Lett. **80**, 3320–3323 (1998).
[228]X. Blase, I. Duchemin, and D. Jacquemin, "The Bethe–Salpeter equation in chemistry: Relations with TD-DFT, applications and challenges," Chem. Soc. Rev. **47**, 1022–1043 (2018).
[229]M. E. Casida *et al.*, "Time-dependent density-functional theory for molecules and molecular solids," J. Mol. Struct.: THEOCHEM **914**, 1–2 (2009).
[230]F. Bruneval, S. M. Hamed, and J. B. Neaton, "A systematic benchmark of the ab initio Bethe–Salpeter equation approach for low-lying optical excitations of small organic molecules," J. Chem. Phys. **142**, 244101 (2015).
[231]X. Blase and C. Attaccalite, "Charge-transfer excitations in molecular donor-acceptor complexes within the many-body Bethe–Salpeter approach," Appl. Phys. Lett. **99**, 171909 (2011).
[232]I. Duchemin, T. Deutsch, and X. Blase, "Short-range to long-range charge-transfer excitations in the zincbacteriochlorin-bacteriochlorin complex: A bethe-salpeter study," Phys. Rev. Lett. **109**, 167801 (2012).
[233]C. Faber, I. Duchemin, T. Deutsch, and X. Blase, "Many-body Green's function study of coumarins for dye-sensitized solar cells," Phys. Rev. B **86**, 155315 (2012).
[234]P. F. Loos, M. Comin, X. Blase, and D. Jacquemin, "Reference energies for intramolecular charge-transfer excitations," J. Chem. Theory Comput. **17**, 3666–3686 (2021).
[235]I. Duchemin, D. Jacquemin, and X. Blase, "Combining the GW formalism with the polarizable continuum model: A state-specific non-equilibrium approach," J. Chem. Phys. **144**, 164106 (2016).
[236]I. Duchemin, C. A. Guido, D. Jacquemin, and X. Blase, "The bethe–salpeter formalism with polarisable continuum embedding: Reconciling linear-response and state-specific features," Chem. Sci. **9**, 4430–4443 (2018).
[237]G. Tirimbò, V. Sundaram, O. Çaylak, W. Scharpach, J. Sijen, C. Junghans, J. Brown, F. Z. Ruiz, N. Renaud, J. Wehner, and B. Baumeier, "Excited-state electronic structure of molecules using many-body Green's functions: Quasiparticles and electron–hole excitations with VOTCA-XTP," J. Chem. Phys. **152**, 114103 (2020).
[238]A. R. Kshirsagar and R. Poloni, "Assessing the role of the Kohn–Sham density in the calculation of the low-lying bethe–salpeter excitation energies," J. Phys. Chem. A **127**, 2618–2627 (2023).
[239]T. Yanai, D. P. Tew, and N. C. Handy, "A new hybrid exchange–correlation functional using the Coulomb-attenuating method (CAM-B3LYP)," Chem. Phys. Lett. **393**, 51–57 (2004).
[240]M. A. Rohrdanz, K. M. Martins, and J. M. Herbert, "A long-range-corrected density functional that performs well for both ground-state properties and time-dependent density functional theory excitation energies, including charge-transfer excited states," J. Chem. Phys. **130**, 054112 (2009).
[241]Z. Hashemi and L. Leppert, "Assessment of the *ab initio* bethe–salpeter equation approach for the low-lying excitation energies of bacteriochlorophylls and chlorophylls," J. Phys. Chem. A **125**, 2163–2172 (2021).
[242]M. Reiher and J. Neugebauer, "A mode-selective quantum chemical method for tracking molecular vibrations applied to functionalized carbon nanotubes," J. Chem. Phys. **118**, 1634–1641 (2003).
[243]S. Luber, J. Neugebauer, and M. Reiher, "Intensity tracking for theoretical infrared spectroscopy of large molecules," J. Chem. Phys. **130**, 064105 (2009).
[244]A. Ghysels, D. Van Neck, V. Van Speybroeck, T. Verstraelen, and M. Waroquier, "Vibrational modes in partially optimized molecular systems," J. Chem. Phys. **126**, 224102 (2007).
[245]R. Terrett, R. Stranger, T. Frankcombe, and R. J. Pace, "Vibrational intensities in the mobile block Hessian approximation," Phys. Chem. Chem. Phys. **19**, 6654–6664 (2017).
[246]D. A. Long, *The Raman Effect: A unified treatment of the Theory of Raman Scattering by Molecules* (John Wiley & Sons Ltd, 2002).
[247]L. Barron, *Molecular Light Scattering and Optical Activity*, 2nd ed. (Cambridge University Press, Cambridge, 2004).
[248]L. Jensen, L. L. Zhao, J. Autschbach, and G. C. Schatz, "Theory and method for calculating resonance Raman scattering from resonance polarizability derivatives," J. Chem. Phys. **123**, 174110 (2005).
[249]N. Valley, L. Jensen, J. Autschbach, and G. C. Schatz, "Theoretical studies of surface enhanced hyper-Raman spectroscopy: The chemical enhancement mechanism," J. Chem. Phys. **133**, 054103 (2010).
[250]N. Valley, L. Jensen, J. Autschbach, and G. C. Schatz, in *Computational Methods for Large Systems*, edited by J. R. Reimers (John Wiley & Sons, Singapore, 2011), pp. 493–514.
[251]J. Neugebauer, E. J. Baerends, E. V. Efremov, F. Ariese, and C. Gooijer, "Combined theoretical and experimental deep-UV resonance Raman studies of substituted pyrenes," J. Phys. Chem. A **109**, 2100–2106 (2005).
[252]S. Gómez, P. Lafiosca, F. Egidi, T. Giovannini, and C. Cappelli, "UV-resonance Raman spectra of systems in complex environments: A multiscale modeling applied to doxorubicin intercalated into dna," J. Chem. Inf. Model. **63**, 1208–1217 (2023).
[253]T. Petrenko and F. Neese, "Analysis and prediction of absorption band shapes, fluorescence band shapes, resonance Raman intensities, and excitation profiles using the time-dependent theory of electronic spectroscopy," J. Chem. Phys. **127**, 164319 (2007).
[254]L. Jensen, C. M. Aikens, and G. C. Schatz, "Electronic structure methods for studying surface-enhanced Raman scattering," Chem. Soc. Rev. **37**, 1061–1073 (2008).
[255]S. M. Morton, D. W. Silverstein, and L. Jensen, "Theoretical studies of plasmonics using electronic structure methods," Chem. Rev. **111**, 3962–3994 (2011).
[256]L. Jensen, P. T. van Duijnen, and J. G. Snijders, "A discrete solvent reaction field model for calculating frequency-dependent hyperpolarizabilities of molecules in solution," J. Chem. Phys. **119**, 12998–13006 (2003).
[257]L. Jensen, P.-O. Åstrand, and K. V. Mikkelsen, "An atomic capacitance–polarizability model for the calculation of molecular dipole moments and polarizabilities," Int. J. Quantum Chem. **84**, 513–522 (2001).
[258]J. L. Payton, S. M. Morton, J. E. Moore, and L. Jensen, "A discrete interaction model/quantum mechanical method for simulating surface-enhanced Raman spectroscopy," J. Chem. Phys. **136**, 214103 (2012).
[259]D. V. Chulhai and L. Jensen, "Simulating surface-enhanced Raman optical activity using atomistic electrodynamics-quantum mechanical models," J. Phys. Chem. A **118**, 9069–9079 (2014).
[260]L. Jensen, J. Autschbach, M. Krykunov, and G. C. Schatz, "Resonance vibrational Raman optical activity: A time-dependent density functional theory approach," J. Chem. Phys. **127**, 134101 (2007).

[261]C. M. Aikens and G. C. Schatz, "TDDFT studies of absorption and SERS spectra of pyridine interacting with Au_{20}," J. Phys. Chem. A **110**, 13317–13324 (2006).
[262]P. Lafiosca, L. Nicoli, L. Bonatti, T. Giovannini, S. Corni, and C. Cappelli, "QM/classical modeling of surface enhanced Raman scattering based on atomistic electromagnetic models," J. Chem. Theory Comput. **19**, 3616–3633 (2023).
[263]P. Grobas Illobre, P. Lafiosca, T. Guidone, F. Mazza, T. Giovannini, and C. Cappelli, "Multiscale modeling of surface enhanced fluorescence," Nanoscale Adv. **6**, 3410–3425 (2024).
[264]H.-C. Jankowiak, J. L. Stuber, and R. Berger, "Vibronic transitions in large molecular systems: Rigorous prescreening conditions for Franck-Condon factors," J. Chem. Phys. **127**, 234101 (2007).
[265]F. Santoro, R. Improta, A. Lami, J. Bloino, and V. Barone, "Effective method to compute Franck-Condon integrals for optical spectra of large molecules in solution," J. Chem. Phys. **126**, 084509 (2007).
[266]J. R. Reimers, K. R. Wilson, and E. J. Heller, "Complex time dependent wave packet technique for thermal equilibrium systems: Electronic spectra," J. Chem. Phys. **79**, 4749–4757 (1983).
[267]D. Barton, C. König, and J. Neugebauer, "Vibronic-Structure tracking: A shortcut for vibrationally resolved UV/Vis-spectra calculations," J. Chem. Phys. **141**, 164115 (2014).
[268]Z. Hu, J. Autschbach, and L. Jensen, "Simulating third-order nonlinear optical properties using damped cubic response theory within time-dependent density functional theory," J. Chem. Theory Comput. **12**, 1294–1304 (2016).
[269]S. J. A. van Gisbergen, J. G. Snijders, and E. J. Baerends, "A density functional theory study of frequency-dependent polarizabilities and Van der Waals dispersion coefficients for polyatomic molecules," J. Chem. Phys. **103**, 9347–9354 (1995).
[270]S. J. A. van Gisbergen, C. Fonseca Guerra, and E. J. Baerends, "Towards excitation energies and (hyper)polarizability calculations of large molecules. Application of parallelization and linear scaling techniques to time-dependent density functional response theory," J. Comput. Chem. **21**, 1511–1523 (2000).
[271]L. Jensen, J. Autschbach, and G. C. Schatz, "Finite lifetime effects on the polarizability within time-dependent density-functional theory," J. Chem. Phys. **122**, 224115 (2005).
[272]Z. Hu, J. Autschbach, and L. Jensen, "Simulation of resonance hyper-Rayleigh scattering of molecules and metal clusters using a time-dependent density functional theory approach," J. Chem. Phys. **141**, 124305 (2014).
[273]A. Ye, S. Patchkovskii, and J. Autschbach, "Static and dynamic second hyperpolarizability calculated by time–dependent density functional cubic response theory with local contribution and natural bond orbital analysis," J. Chem. Phys. **127**, 074104 (2007).
[274]A. Ye and J. Autschbach, "Study of static and dynamic first hyperpolarizabilities using time-dependent density functional quadratic response theory with local contribution and natural bond orbital analysis," J. Chem. Phys. **125**, 234101 (2006).
[275]A. Devarajan, A. Gaenko, and J. Autschbach, "Two–component relativistic density functional method for computing nonsingular complex linear response of molecules based on the zeroth order regular approximation," J. Chem. Phys. **130**, 194102 (2009).
[276]W. Kauzmann, *Quantum Chemistry* (Academic Press, New York, 1957).
[277]J. Autschbach, "Computing chiroptical properties with first–principles theoretical methods: Background and illustrative examples," Chirality **21**, E116–E152 (2009).
[278]J. Autschbach and T. Ziegler, "Calculating molecular electric and magnetic properties from time-dependent density functional response theory," J. Chem. Phys. **116**, 891–896 (2002).
[279]J. Autschbach, T. Ziegler, S. J. A. van Gisbergen, and E. J. Baerends, "Chiroptical properties from time-dependent density functional theory. I. Circular dichroism spectra of organic molecules," J. Chem. Phys. **116**, 6930–6940 (2002).
[280]J. Autschbach, S. Patchkovskii, T. Ziegler, S. J. A. van Gisbergen, and E. Jan Baerends, "Chiroptical properties from time-dependent density functional theory. II. Optical rotations of small to medium sized organic molecules," J. Chem. Phys. **117**, 581–592 (2002).
[281]J. Autschbach, L. Jensen, G. C. Schatz, Y. C. E. Tse, and M. Krykunov, "Time–dependent density functional calculations of optical rotatory dispersion including resonance wavelengths as a potentially useful tool for determining absolute configurations of chiral molecules," J. Phys. Chem. A **110**, 2461–2473 (2006).
[282]M. Rudolph and J. Autschbach, "Fast generation of nonresonant and resonant optical rotatory dispersion curves with the help of circular dichroism calculations and Kramers–Kronig transformations," Chirality **20**, 995–1008 (2008).
[283]M. Krykunov, M. D. Kundrat, and J. Autschbach, "Calculation of circular dichroism spectra from optical rotatory dispersion, and vice versa, as complementary tools for theoretical studies of optical activity using time–dependent density functional theory," J. Chem. Phys. **125**, 194110 (2006).
[284]M. Krykunov and J. Autschbach, "Calculation of origin-independent optical rotation tensor components in approximate time-dependent density functional theory," J. Chem. Phys. **125**, 034102 (2006).
[285]M. Krykunov and J. Autschbach, "Calculation of optical rotation with time-periodic magnetic-field-dependent basis functions in approximate time-dependent density-functional theory," J. Chem. Phys. **123**, 114103 (2005).
[286]M. Krykunov and J. Autschbach, "Calculation of static and dynamic linear magnetic response in approximate time-dependent density functional theory," J. Chem. Phys. **126**, 024101 (2007).
[287]J. Autschbach, F. E. Jorge, and T. Ziegler, "Density functional calculations on electronic circular dichroism spectra of chiral transition metal complexes," Inorg. Chem. **42**, 2867–2877 (2003).
[288]F. E. Jorge, J. Autschbach, and T. Ziegler, "On the origin of the optical activity in the d–d transition region of tris-bidentate Co(III) and Rh(III) complexes," Inorg. Chem. **42**, 8902–8910 (2003).
[289]F. E. Jorge, J. Autschbach, and T. Ziegler, "On the origin of optical activity in tris-diamine complexes of Co(III) and Rh(III): A simple model based on time-dependent density function theory," J. Am. Chem. Soc. **127**, 975–985 (2005).
[290]F. Furche, R. Ahlrichs, C. Wachsmann, E. Weber, A. Sobanski, F. Vögtle, and S. Grimme, "Circular dichroism of helicenes investigated by time-dependent density functional theory," J. Am. Chem. Soc. **122**, 1717–1724 (2000).
[291]S. Grimme, "Calculation of frequency dependent optical rotation using density functional response theory," Chem. Phys. Lett. **339**, 380–388 (2001).
[292]L. A. Nafie, "Theory of resonance Raman optical activity: The single electronic state limit," Chem. Phys. **205**, 309–322 (1996).
[293]L. Abella, H. D. Ludowieg, and J. Autschbach, "Theoretical Study of the Raman Optical Activity Spectra of $[M(en)_3]^{3+}$ with M = Co, Rh," Chirality **32**, 741–752 (2020).
[294]G. Li, M. Alshalalfeh, Y. Yang, J. R. Cheeseman, P. Bouř, and Y. Xu, "Can one measure resonance Raman optical activity?," Angew. Chem., Int. Ed. **133**, 22175 (2021).
[295]J. P. Riehl and F. S. Richardson, "Circularly polarized luminescence spectroscopy," Chem. Rev. **86**, 1–16 (1986).
[296]H. D. Ludowieg, M. Srebro-Hooper, J. Crassous, and J. Autschbach, "Optical activity of spin-forbidden electronic transitions in metal complexes from time-dependent density functional theory with spin-orbit coupling," Chem.Open **11**, e202200020 (2022).
[297]P. J. Stephens, "Theory of vibrational circular dichroism," J. Phys. Chem. **89**, 748–752 (1985).
[298]J. Gerratt and I. M. Mills, "Force constants and dipole-moment derivatives of molecules from perturbed Hartree–Fock calculations. I," J. Chem. Phys. **49**, 1719–1729 (1968).
[299]J. A. Pople, R. Krishnan, H. B. Schlegel, and J. S. Binkley, "Derivative studies in Hartree–Fock and Møller–Plesset theories," Int. J. Quantum Chem. **16**, 225–241 (1979).
[300]G. Schreckenbach and T. Ziegler, "Calculation of NMR shielding tensors using gauge-including atomic orbitals and modern density functional theory," J. Phys. Chem. **99**, 606–611 (1995).
[301]S. K. Wolff, "Analytical second derivatives in the Amsterdam density functional package," Int. J. Quantum Chem. **104**, 645–659 (2005).
[302]V. P. Nicu, J. Neugebauer, S. K. Wolff, and E. J. Baerends, "A vibrational circular dichroism implementation within a Slater-type-orbital based density functional framework and its application to hexa- and hepta-helicenes," Theor. Chem. Acc. **119**(1–3), 245–263 (2008).
[303]F. London, "Théorie quantique des courants interatomiques dans les combinaisons aromatiques," J. Phys. Radium **8**, 397–409 (1937).

[304]R. Ditchfield, "Self-consistent perturbation theory of diamagnetism: I. A gauge-invariant LCAO method for N.M.R. chemical shifts," Mol. Phys. **27**, 789–807 (1974).
[305]K. L. Bak, P. Jørgensen, T. Helgaker, K. Ruud, and H. J. A. Jensen, "Gauge-origin independent multi-configurational self-consistent-field theory for vibrational circular dichroism," J. Chem. Phys. **98**, 8873–8887 (1993).
[306]V. P. Nicu, E. Debie, W. Herrebout, B. Van der Veken, P. Bultinck, and E. J. Baerends, "A VCD robust mode analysis of induced chirality: The case of pulegone in chloroform," Chirality **21**, E287–E297 (2010).
[307]V. P. Nicu, M. Heshmat, and E. J. Baerends, "Signatures of counter-ion association and hydrogen bonding in vibrational circular dichroism spectra," Phys. Chem. Chem. Phys. **13**, 8811–8825 (2011).
[308]V. P. Nicu, E. J. Baerends, and P. L. Polavarapu, "Understanding solvent effects in vibrational circular dichroism spectra: [1,1′-Binaphthalene]-2,2′-diol in dichloromethane, acetonitrile, and dimethyl sulfoxide solvents," J. Phys. Chem. A **116**, 8366–8373 (2012).
[309]V. Nicu, A. Mandi, T. Kurtan, and P. Polavarapu, "On the complementarity of ECD and VCD techniques," Chirality **26**, 525–531 (2014).
[310]M. Passarello, S. Abbate, G. Longhi, S. Lepri, R. Ruzziconi, and V. P. Nicu, "Importance of C*–H based modes and large amplitude motion effects in vibrational circular dichroism spectra: The case of the chiral adduct of dimethyl fumarate and anthracene," J. Phys. Chem. A **118**, 4339–4350 (2014).
[311]M. A. J. Koenis, E. H. Tiekink, D. M. E. van Raamsdonk, N. U. Joosten, S. A. Gooijer, V. P. Nicu, L. Visscher, and W. J. Buma, "Analytical chemistry on many-center chiral compounds based on vibrational circular dichroism: Absolute configuration assignments and determination of contaminant levels," Anal. Chim. Acta **1090**, 100–105 (2019).
[312]M. A. J. Koenis, Y. Xia, S. R. Domingos, L. Visscher, W. J. Buma, and V. P. Nicu, "Taming conformational heterogeneity in and with vibrational circular dichroism spectroscopy," Chem. Sci. **10**, 7680 (2019).
[313]M. A. J. Koenis, V. P. Nicu, L. Visscher, C. Kuehn, M. Bremer, M. Krier, H. Untenecker, U. Zhumaev, B. Küstner, and W. J. Buma, "Vibrational circular dichroism studies of exceptionally strong chirality inducers in liquid crystals," Phys. Chem. Chem. Phys. **23**, 10021 (2021).
[314]G. Marton, M. A. J. Koenis, H.-B. Liu, C. A. Bewley, W. J. Buma, and V. P. Nicu, "An artificial intelligence approach for tackling conformational energy uncertainties in chiroptical spectroscopies," Angew. Chem., Int. Ed. **62**, e202307053 (2023).
[315]P. J. Stephens, "Gauge dependence of vibrational magnetic dipole transition moments and rotational strengths," J. Phys. Chem. **91**, 1712–1715 (1987).
[316]V. P. Nicu and E. J. Baerends, "On the origin dependence of the angle made by the electric and magnetic vibrational transition dipole moment vectors," Phys. Chem. Chem. Phys. **13**, 16126–16129 (2011).
[317]V. P. Nicu, E. J. Baerends, and E. J. Baerends, "Effects of complex formation on vibrational circular dichroism spectra," J. Phys. Chem. A **112**(30), 6978–6991 (2008).
[318]M. A. J. Koenis, O. Visser, L. Visscher, W. J. Buma, and V. P. Nicu, "GUI implementation of VCDtools, A program to analyze computed vibrational circular dichroism spectra," J. Chem. Inf. Model. **60**, 259–267 (2020).
[319]V. P. Nicu, "Revisiting an old concept: The coupled oscillator model for VCD. Part 1: The generalised coupled oscillator mechanism and its intrinsic connection to the strength of VCD signals," Phys. Chem. Chem. Phys. **18**, 21202 (2016).
[320]V. P. Nicu, "Revisiting an old concept: The coupled oscillator model for VCD. Part 2: Implications of the generalised coupled oscillator mechanism for the VCD robustness concept," Phys. Chem. Chem. Phys. **18**, 21213 (2016).
[321]A. Banerjee, J. Autschbach, and T. Ziegler, "A gauge-origin independent expression for the Verdet constant within the time-dependent density functional theory," Int. J. Quantum Chem. **101**, 572–578 (2005).
[322]M. Krykunov, A. Banerjee, T. Ziegler, and J. Autschbach, "Calculation of Verdet constants with time-dependent density functional theory: Implementation and results for small molecules," J. Chem. Phys. **122**, 074105 (2005).
[323]M. Seth, T. Ziegler, and J. Autschbach, "Application of magnetically perturbed time–dependent density functional theory to magnetic circular dichroism. III. Temperature–dependent magnetic circular dichroism induced by spin–orbit coupling," J. Chem. Phys. **129**, 104105 (2008).
[324]M. Seth, M. Krykunov, T. Ziegler, and J. Autschbach, "Application of magnetically perturbed time-dependent density functional theory to magnetic circular dichroism. II. Calculation of A terms," J. Chem. Phys. **128**, 234102 (2008).
[325]M. Seth, M. Krykunov, T. Ziegler, J. Autschbach, and A. Banerjee, "Application of magnetically perturbed time-dependent density functional theory to magnetic circular dichroism: Calculation of B terms," J. Chem. Phys. **128**, 144105 (2008).
[326]M. Krykunov, M. Seth, T. Ziegler, and J. Autschbach, "Calculation of the magnetic circular dichroism B term from the imaginary part of the Verdet constant using damped time-dependent density functional theory," J. Chem. Phys. **127**, 244102 (2007).
[327]M. Seth, J. Autschbach, and T. Ziegler, "Calculation of the B term of magnetic circular dichroism: A time-dependent density functional theory approach," J. Chem. Theory Comput. **3**, 434–447 (2007).
[328]M. Seth, T. Ziegler, and J. Autschbach, "*Ab initio* calculation of the *C*/*D* ratio of magnetic circular dichroism," J. Chem. Phys. **122**, 094112 (2005).
[329]M. Seth, T. Ziegler, A. Banerjee, J. Autschbach, S. J. A. van Gisbergen, and E. J. Baerends, "Calculation of the $_A$–term of magnetic circular dichroism based on time dependent-density functional theory I. Formulation and implementation," J. Chem. Phys. **120**, 10942–10954 (2004).
[330]G. Schreckenbach and T. Ziegler, "Calculation of NMR shielding tensors based on density functional theory and a scalar relativistic Pauli-type Hamiltonian. The application to transition metal complexes," Int. J. Quantum Chem. **61**, 899–918 (1997).
[331]S. K. Wolff and T. Ziegler, "Calculation of DFT-GIAO NMR shifts with the inclusion of spin-orbit coupling," J. Chem. Phys. **109**, 895–905 (1998).
[332]S. K. Wolff, T. Ziegler, E. van Lenthe, and E. J. Baerends, "Density functional calculations of nuclear magnetic shieldings using the zeroth-order regular approximation (ZORA) for relativistic effects: ZORA nuclear magnetic resonance," J. Chem. Phys. **110**, 7689–7698 (1999).
[333]J. Autschbach and E. Zurek, "Relativistic density functional calculations of the ^{129}Xe chemical shift in Xe@C_{60}," J. Phys. Chem. A **107**, 4967–4972 (2003).
[334]M. Krykunov, T. Ziegler, and E. van Lenthe, "Implementation of a hybrid DFT method for calculating NMR shieldings using slater-type orbitals with spin-orbital coupling included. Applications to ^{187}Os, ^{195}Pt, and ^{13}C in heavy-metal complexes," J. Phys. Chem. A **113**, 11495–11500 (2009).
[335]J. Autschbach, "The role of the exchange-correlation response kernel and scaling corrections in relativistic density functional nuclear magnetic shielding calculations with the zeroth-order regular approximation," Mol. Phys. **111**, 2544–2554 (2013).
[336]J. Autschbach and T. Ziegler, "Nuclear spin–spin coupling constants from regular approximate relativistic density functional calculations. I. Formalism and scalar relativistic results for heavy metal compounds," J. Chem. Phys. **113**, 936–947 (2000).
[337]J. Autschbach and T. Ziegler, "Nuclear spin–spin coupling constants from regular approximate relativistic density functional calculations. II. Spin–orbit coupling effects and anisotropies," J. Chem. Phys. **113**, 9410–9418 (2000).
[338]J. Autschbach, "Two–component relativistic hybrid density functional computations of nuclear spin–spin coupling tensors using Slater–type basis sets and density–fitting techniques," J. Chem. Phys. **129**, 094105 (2008).
[339]E. van Lenthe and E. J. Baerends, "Density functional calculations of nuclear quadrupole coupling constants in the zero-order regular approximation for relativistic effects," J. Chem. Phys. **112**, 8279–8292 (2000).
[340]G. Schreckenbach and T. Ziegler, "Density functional calculations of NMR chemical shifts and ESR g-tensors," Theor. Chem. Acc.: Theory, Comput., Model. **99**, 71–82 (1998).
[341]S. Patchkovskii and T. Ziegler, "Prediction of electron paramagnetic resonance g-tensors of transition metal complexes using density functional theory: First applications to some axial d^1 MEX_4 systems," J. Chem. Phys. **111**, 5730–5740 (1999).
[342]E. van Lenthe, P. E. S. Wormer, and A. van der Avoird, "Density functional calculations of molecular *g*-tensors in the zero-order regular approximation for relativistic effects," J. Chem. Phys. **107**, 2488–2498 (1997).
[343]E. van Lenthe, A. van der Avoird, and P. E. S. Wormer, "Density functional calculations of molecular hyperfine interactions in the zero order regular approximation for relativistic effects," J. Chem. Phys. **108**, 4783–4796 (1998).

[344]E. van Lenthe, A. van der Avoird, W. R. Hagen, and E. J. Reijerse, "Density functional calculations of *g*-tensors of low-spin iron(I) and iron(III) porphyrins," J. Phys. Chem. A **104**, 2070–2077 (2000).
[345]J. Autschbach and B. Pritchard, "Calculation of molecular g-tensors using the zeroth-order regular approximation and density functional theory: Expectation value versus linear response approaches," Theor. Chem. Acc. **129**, 453–466 (2011).
[346]J. Autschbach, S. Patchkovskii, and B. Pritchard, "Calculation of hyperfine tensors and paramagnetic NMR shifts using the relativistic zeroth-order regular approximation and density functional theory," J. Chem. Theory Comput. **7**, 2175–2188 (2011).
[347]M. R. Pederson and S. N. Khanna, "Magnetic anisotropy barrier for spin tunneling in $Mn_{12}O_{12}$ molecules," Phys. Rev. B **60**, 9566–9572 (1999).
[348]F. Neese, "Calculation of the zero-field splitting tensor on the basis of hybrid density functional and Hartree–Fock theory," J. Chem. Phys. **127**, 164112 (2007).
[349]C. van Wüllen, "Magnetic anisotropy from density functional calculations. Comparison of different approaches: $Mn_{12}O_{12}$ acetate as a test case," J. Chem. Phys. **130**, 194109 (2009).
[350]S. Schmitt, P. Jost, and C. van Wüllen, "Zero-field splittings from density functional calculations: Analysis and improvement of known methods," J. Chem. Phys. **134**, 194113 (2011).
[351]K. Mori, T. P. M. Goumans, E. van Lenthe, and F. Wang, "Predicting phosphorescent lifetimes and zero-field splitting of organometallic complexes with time-dependent density functional theory including spin–orbit coupling," Phys. Chem. Chem. Phys. **16**, 14523–14530 (2014).
[352]D. L. Bryce and R. E. Wasylishen, "Indirect nuclear spin−spin coupling tensors in diatomic Molecules: A comparison of results obtained by experiment and first principles calculations," J. Am. Chem. Soc. **122**, 3197–3205 (2000).
[353]J. Autschbach, "The accuracy of hyperfine integrals in relativistic NMR computations based on the zeroth-order regular approximation," Theor. Chem. Acc.: Theory, Comput., Model. **112**, 52–57 (2004).
[354]V. Arcisauskaite, J. I. Melo, L. Hemmingsen, and S. P. A. Sauer, "Nuclear magnetic resonance shielding constants and chemical shifts in linear ^{199}Hg compounds: A comparison of three relativistic computational methods," J. Chem. Phys. **135**, 044306 (2011).
[355]A. Wodyński, M. Repiský, and M. Pecul, "A comparison of two-component and four-component approaches for calculations of spin-spin coupling constants and NMR shielding constants of transition metal cyanides," J. Chem. Phys. **137**, 014311 (2012).
[356]J. Vícha, J. Novotný, M. Straka, M. Repisky, K. Ruud, S. Komorovsky, and R. Marek, "Structure, solvent, and relativistic effects on the NMR chemical shifts in square-planar transition-metal complexes: Assessment of DFT approaches," Phys. Chem. Chem. Phys. **17**, 24944–24955 (2015).
[357]A. C. Castro, D. Balcells, M. Repisky, T. Helgaker, and M. Cascella, "First-Principles calculation of 1H NMR chemical shifts of complex metal polyhydrides: The essential inclusion of relativity and dynamics," Inorg. Chem. **59**, 17509–17518 (2020).
[358]S. Komorovsky, K. Jakubowska, P. Świder, M. Repisky, and M. Jaszuński, "NMR spin–spin coupling constants derived from relativistic four-component DFT theory–analysis and visualization," J. Phys. Chem. A **124**, 5157–5169 (2020).
[359]L. L. Foldy and S. A. Wouthuysen, "On the Dirac theory of spin 1/2 particles and its non-relativistic limit," Phys. Rev. **78**, 29 (1950).
[360]E. J. Baerends, W. H. E. Schwarz, P. Schwerdtfeger, and J. G. Snijders, "Relativistic atomic orbital contractions and expansions: Magnitudes and explanations," J. Phys. B.: At., Mol. Opt. Phys. **23**, 3225–3240 (1990).
[361]Y. Ikabata and H. Nakai, "Picture-change correction in relativistic density functional theory," Phys. Chem. Chem. Phys. **23**, 15458–15474 (2021).
[362]F. Neese, A. Wolf, T. Fleig, M. Reiher, and B. A. Hess, "Calculation of electric-field gradients based on higher-order generalized Douglas–Kroll transformations," J. Chem. Phys. **122**, 204107 (2005).
[363]F. Aquino, N. Govind, and J. Autschbach, "Electric field gradients calculated from two-component hybrid density functional theory including spin–orbit coupling," J. Chem. Theory Comput. **6**, 2669–2686 (2010).
[364]J. Autschbach and T. Ziegler, "Solvent effects on heavy atom nuclear spin–spin coupling Constants: A theoretical study of Hg−C and Pt−P couplings," J. Am. Chem. Soc. **123**, 3341–3349 (2001).
[365]R. Malleier, H. Kopacka, W. Schuh, K. Wurst, and P. Peringer, "$^1J(^{199}$Hg-^{199}Hg) values of up to 284 kHz in complexes of $[Hg\text{-}Hg]^{2+}$ with crown ethers: The largest indirect coupling constants," Chem. Commun. **2001**, 51–52.
[366]J. Autschbach, C. D. Igna, and T. Ziegler, "A theoretical study of the large Hg-Hg spin-spin coupling constants in Hg_2^{2+}, Hg_3^{2+}, and Hg_2^{2+}– crown-ether complexes," J. Am. Chem. Soc. **125**, 4937–4942 (2003).
[367]K. P. Kornecki, J. F. Briones, V. Boyarskikh, F. Fullilove, J. Autschbach, K. E. Schrote, K. M. Lancaster, H. M. L. Davies, and J. F. Berry, "Direct spectroscopic characterization of a transitory dirhodium donor–acceptor carbene complex," Science **342**, 351–354 (2013).
[368]E. D. Glendening, C. R. Landis, and F. Weinhold, "Natural bond orbital methods," WIREs Comput. Mol. Sci. **2**, 1–42 (2012).
[369]J. Autschbach, "Analyzing NMR shielding tensors calculated with two–component relativistic methods using spin–free localized molecular orbitals," J. Chem. Phys. **128**, 164112 (2008).
[370]J. Autschbach and S. Zheng, "Analyzing Pt chemical shifts calculated from relativistic density functional theory using localized orbitals: The role of Pt lone pairs," Magn. Reson. Chem. **46**, S45–S55 (2008).
[371]J. Autschbach, "Analyzing molecular properties calculated with two-component relativistic methods using spin-free natural bond orbitals: NMR spin-spin coupling constants," J. Chem. Phys. **127**, 124106 (2007).
[372]J. Autschbach, S. Zheng, and R. W. Schurko, "Analysis of electric field gradient tensors at quadrupolar nuclei in common structural motifs," Concepts Magn. Reson., Part A **36A**, 84–126 (2010).
[373]A. Fernández-Alarcón and J. Autschbach, "Relativistic density functional NMR tensors analyzed with spin-free localized molecular orbitals," ChemPhysChem **24**, e202200667 (2023).
[374]S. T. Holmes, J. Schönzart, A. B. Philips, J. J. Kimball, S. Termos, A. R. Altenhof, Y. Xu, C. A. O'Keefe, J. Autschbach, and R. W. Schurko, "Structure and bonding in rhodium coordination compounds: A ^{103}Rh solid-state NMR and relativistic DFT study," Chem. Sci. **15**, 2181–2196 (2024).
[375]R. V. Viesser, L. C. Ducati, C. F. Tormena, and J. Autschbach, "The unexpected roles of σ and π orbitals in electron donor and acceptor group effects on the ^{13}C NMR chemical shifts in substituted benzenes," Chem. Sci. **8**, 6570–6576 (2017).
[376]Analysis of NMR parameters with Localized Molecular Orbitals, https://www.scm.com/doc/Tutorials/NMR/NMRAnalysisWithNLMOAndNBO.html, accessed 06 Jun 2024.
[377]Z. Chen, C. S. Wannere, C. Corminboeuf, R. Puchta, and P. v. R. Schleyer, "Nucleus-Independent chemical shifts (NICS) as an aromaticity criterion," Chem. Rev. **105**, 3842–3888 (2005).
[378]G. te Velde and E. J. Baerends, "Slab versus cluster approach for chemisorption studies. CO on Cu(100)," Chem. Phys. **177**, 399–406 (1993).
[379]R. Hoffmann, *Solids and Surfaces* (VCH, Weinheim (BRD), 1988).
[380]M. G. Goesten, "Be–Be π-bonding and predicted superconductivity in MBe_2 (M=Zr, Hf)," Angew. Chem., Int. Ed. **61**, e202114303 (2022).
[381]M. G. Goesten, Y. Xia, U. Aschauer, and M. Amsler, "Conformational gap control in $CsTaS_3$," J. Am. Chem. Soc. **144**, 3398–3410 (2022).
[382]M. G. Goesten and R. Hoffmann, "Mirrors of bonding in metal halide perovskites," J. Am. Chem. Soc. **140**, 12996–13010 (2018).
[383]A. Majid, M. Ramzan, S. Ahmad, and M. Alkhedher, "Unraveling the potential of Al_2CO bilayer as anode material in magnesium ion battery and unsuitability for lithium ion battery," J. Alloys Compd. **981**, 173697 (2024).
[384]H. Xie, W. Su, H. Lu, Z. Mo, D. Wang, H. Sun, L. tian, X. Gao, Z. Li, and J. Shen, "Enhanced low-field magnetocaloric effect in Nb and Al co-substituted $EuTiO_3$ compounds," J. Mater. Sci. Technol. **118**, 128–135 (2022).
[385]S. Racioppi, P. Hyldgaard, and M. Rahm, "Quantifying atomic volume, partial charge, and electronegativity in condensed phases," J. Phys. Chem. C **128**, 4009–4017 (2024).
[386]S. Nachimuthu, Y.-H. Kuo, D. H. Khanh, Z.-J. Zhu, and J.-C. Jiang, "Density functional theory study on sensing properties of g-C_3N_4 sheet to atmospheric gasses: Role of zigzag and armchair edges," J. Chin. Chem. Soc. **70**, 349–358 (2023).
[387]S. Cavo, J. A. Berger, and P. Romaniello, "Accurate optical spectra of solids from pure time-dependent density functional theory," Phys. Rev. B **101**, 115109 (2020).

[388]A. Cadiau, N. Kolobov, S. Srinivasan, M. G. Goesten, H. Haspel, A. V. Bavykina, M. R. Tchalala, P. Maity, A. Goryachev, A. S. Poryvaev, M. Eddaoudi, M. V. Fedin, O. F. Mohammed, and J. Gascon, "A titanium metal–organic framework with visible-light-responsive photocatalytic activity," Angew. Chem., Int. Ed. **59**, 13468–13472 (2020).
[389]P. H. T. Philipsen and E. J. Baerends, "Role of the Fermi surface in adsorbate–metal interactions: An energy decomposition analysis," J. Phys. Chem. B **110**, 12470–12479 (2006).
[390]M. Raupach and R. Tonner, "A periodic energy decomposition analysis method for the investigation of chemical bonding in extended systems," J. Chem. Phys. **142**, 194105 (2015).
[391]F. Thiemann, H. Weiske, and R. E. Tonner-Zech, "Trends in the reactivity of pentacyclic ether derivatives on silicon and germanium surfaces revealed by energy decomposition analysis for extended systems," Eur. J. Org Chem. **27**, e202400560 (2024).
[392]P. P. Wellmann, F. Pieck, and R. Tonner-Zech, "An atomistic picture of buildup and degradation reactions in area-selective atomic layer deposition with a small molecule inhibitor," Chem. Mater. **36**, 7343–7361 (2024).
[393]J. Anders, H. Wiedenhaupt, F. Kreuter, R. Tonner-Zech, and B. Paulus, "Chemical bonding of HF, HCl, and H_2O onto YF_3 surfaces: Quantification by first principles," J. Comput. Chem. **44**, 1986–1997 (2023).
[394]B. P. Klein, A. Ihle, S. R. Kachel, L. Ruppenthal, S. J. Hall, L. Sattler, S. M. Weber, J. Herritsch, A. Jaegermann, D. Ebeling, R. J. Maurer, G. Hilt, R. Tonner-Zech, A. Schirmeisen, and J. M. Gottfried, "Topological Stone–Wales defects enhance bonding and electronic coupling at the graphene/metal interface," ACS Nano **16**, 11979–11987 (2022).
[395]J.-N. Luy, P. Henkel, D. Grigjanis, J. Jung, D. Mollenhauer, and R. Tonner-Zech, "Bonding character of intermediates in on-surface Ullmann reactions revealed with energy decomposition analysis," J. Comput. Chem. **44**, 179–189 (2022).
[396]F. Pieck and R. Tonner-Zech, "Alkyne-Functionalized cyclooctyne on Si(001): Reactivity studies and surface bonding from an energy decomposition analysis perspective," Molecules **26**, 6653 (2021).
[397]F. Kreuter and R. Tonner, "Surface functionalization with nonalternant aromatic compounds: A computational study of azulene and naphthalene on Si(001)," J. Phys.: Condens. Matter **33**, 444003 (2021).
[398]J.-N. Luy and R. Tonner, "Organic functionalization at the Si(001) dimer vacancy Defect—Structure, bonding, and reactivity," J. Phys. Chem. C **125**, 5635–5646 (2021).
[399]T. Glaser, J. Meinecke, C. Länger, J.-N. Luy, R. Tonner, U. Koert, and M. Dürr, "Combined XPS and DFT investigation of the adsorption modes of methyl enol ether functionalized cyclooctyne on Si(001)," ChemPhysChem **22**, 404–409 (2021).
[400]T. E. Sandoval, F. Pieck, R. Tonner, and S. F. Bent, "Effect of heteroaromaticity on adsorption of pyrazine on the Ge(100)-2 × 1 surface," J. Phys. Chem. C **124**, 22055–22068 (2020).
[401]S. R. Kachel, B. P. Klein, J. M. Morbec, M. Schöniger, M. Hutter, M. Schmid, P. Kratzer, B. Meyer, R. Tonner, and J. M. Gottfried, "Chemisorption and physisorption at the metal/organic interface: Bond energies of naphthalene and azulene on coinage metal surfaces," J. Phys. Chem. C **124**, 8257–8268 (2020).
[402]B. P. Klein, S. E. Harman, L. Ruppenthal, G. M. Ruehl, S. J. Hall, S. J. Carey, J. Herritsch, M. Schmid, R. J. Maurer, R. Tonner, C. T. Campbell, and J. M. Gottfried, "Enhanced bonding of pentagon–heptagon defects in graphene to metal surfaces: Insights from the adsorption of azulene and naphthalene to Pt(111)," Chem. Mater. **32**, 1041–1053 (2020).
[403]G. Wiesenekker, G. t. Velde, and E. J. Baerends, "Analytic quadratic integration over the two-dimensional Brillouin zone," J. Phys. C: Solid State Phys. **21**, 4263 (1988).
[404]G. Wiesenekker and E. J. Baerends, "Quadratic integration over the three-dimensional Brillouin zone," J. Phys.: Condens. Matter **3**, 6721 (1991).
[405]A. Irmler, A. M. Burow, and F. Pauly, "Robust periodic Fock exchange with atom-centered Gaussian basis sets," J. Chem. Theory Comput. **14**, 4567–4580 (2018).
[406]P. H. T. Philipsen, E. van Lenthe, J. G. Snijders, and E. J. Baerends, "Relativistic calculations on the adsorption of CO on the (111) surfaces of Ni, Pd, and Pt within the zeroth-order regular approximation," Phys. Rev. B **56**, 13556–13562 (1997).
[407]P. H. T. Philipsen and E. J. Baerends, "Relativistic calculations to assess the ability of the generalized gradient approximation to reproduce trends in cohesive properties of solids," Phys. Rev. B **61**, 1773–1778 (2000).
[408]F. Kootstra, P. L. de Boeij, and J. G. Snijders, "Efficient real-space approach to time-dependent density functional theory for the dielectric response of nonmetallic crystals," J. Chem. Phys. **112**, 6517–6531 (2000).
[409]F. Kootstra, P. L. de Boeij, and J. G. Snijders, "Application of time-dependent density-functional theory to the dielectric function of various nonmetallic crystals," Phys. Rev. B **62**, 7071–7083 (2000).
[410]P. L. de Boeij, F. Kootstra, J. A. Berger, R. van Leeuwen, and J. G. Snijders, "Current density functional theory for optical spectra: A polarization functional," J. Chem. Phys. **115**, 1995–1999 (2001).
[411]P. Romaniello and P. L. de Boeij, "Time-dependent current-density-functional theory for the metallic response of solids," Phys. Rev. B **71**, 155108 (2005).
[412]C. J. O. Verzijl, J. S. Seldenthuis, and J. M. Thijssen, "Applicability of the wide-band limit in DFT-based molecular transport calculations," J. Chem. Phys. **138**, 094102 (2013).
[413]C. J. O. Verzijl and J. M. Thijssen, "DFT-based molecular transport implementation in ADF/BAND," J. Phys. Chem. C **116**, 24393–24412 (2012).
[414]J. A. Celis Gil and J. M. Thijssen, "Transport gap renormalization at a metal-molecule interface using DFT-NEGF and spin unrestricted calculations," J. Chem. Phys. **147**, 084102 (2017).
[415]P. Giannozzi *et al.*, "QUANTUM ESPRESSO: A modular and open-source software project for quantum simulations of materials," J. Phys.: Condens. Matter **21**, 395502 (2009).
[416]P. Giannozzi *et al.*, "Advanced capabilities for materials modelling with Quantum ESPRESSO," J. Phys.: Condens. Matter **29**, 465901 (2017).
[417]P. Giannozzi, O. Baseggio, P. Bonfà, D. Brunato, R. Car, I. Carnimeo, C. Cavazzoni, S. de Gironcoli, P. Delugas, F. Ferrari Ruffino, A. Ferretti, N. Marzari, I. Timrov, A. Urru, and S. Baroni, "Quantum ESPRESSO toward the exascale," J. Chem. Phys. **152**, 154105 (2020).
[418]M. Elstner and G. Seifert, "Density functional tight binding," Philos. Trans. R. Soc. A **372**, 20120483 (2014).
[419]C. Bannwarth, E. Caldeweyher, S. Ehlert, A. Hansen, P. Pracht, J. Seibert, S. Spicher, and S. Grimme, "Extended tight-binding quantum chemistry methods," Wiley Interdiscip. Rev.: Comput. Mol. Sci. **11**, e1493 (2021).
[420]D. Porezag, T. Frauenheim, T. Köhler, G. Seifert, and R. Kaschner, "Construction of tight-binding-like potentials on the basis of density-functional theory: Application to carbon," Phys. Rev. B **51**, 12947–12957 (1995).
[421]M. Elstner, D. Porezag, G. Jungnickel, J. Elsner, M. Haugk, T. Frauenheim, S. Suhai, and G. Seifert, "Self-consistent-charge density-functional tight-binding method for simulations of complex materials properties," Phys. Rev. B **58**, 7260 (1998).
[422]M. Gaus, Q. Cui, and M. Elstner, "DFTB3: Extension of the self-consistent-charge density-functional tight-binding method (SCC-DFTB)," J. Chem. Theory Comput. **7**, 931–948 (2011).
[423]S. Grimme, C. Bannwarth, and P. Shushkov, "A robust and accurate tight-binding quantum chemical method for structures, vibrational frequencies, and noncovalent interactions of large molecular systems parametrized for all spd-block elements (Z = 1–86)," J. Chem. Theory Comput. **13**, 1989–2009 (2017).
[424]M. J. S. Dewar and W. Thiel, "Ground states of molecules. 38. The MNDO method. Approximations and parameters," J. Am. Chem. Soc. **99**, 4899–4907 (1977).
[425]J. J. P. Stewart, "Optimization of parameters for semiempirical methods VI: More modifications to the NDDO approximations and re-optimization of parameters," J. Mol. Model. **19**, 1–32 (2013).
[426]M. Atanasov, C. A. Daul, and C. Rauzy, in *Optical Spectra and Chemical Bonding in Inorganic Compounds: Special Volume Dedicated to Professor Jørgensen I*, edited by D. M. P. Mingos and T. Schönherr (Springer, Berlin Heidelberg, 2004), pp. 97–125.
[427]H. Ramanantoanina, W. Urland, F. Cimpoesu, and C. Daul, "Ligand field density functional theory calculation of the $4f^2 \rightarrow 4f^15d^1$ transitions in the quantum cutter Cs_2KYF_6:Pr^{3+}," Phys. Chem. Chem. Phys. **15**, 13902–13910 (2013).
[428]A. S. P. Gomes and C. R. Jacob, "Quantum-chemical embedding methods for treating local electronic excitations in complex chemical systems," Annu. Rep. Prog. Chem., Sec. C **108**, 222–277 (2012).

[429]H.-M. Senn and W. Thiel, "QM/MM methods for biological systems," Top. Curr. Chem. **268**, 173–290 (2007).
[430]J. Tomasi, B. Mennucci, and R. Cammi, "Quantum mechanical continuum solvation models," Chem. Rev. **105**, 2999–3094 (2005).
[431]H. M. Senn and W. Thiel, "QM/MM methods for biomolecular systems," Angew. Chem., Int. Ed. **48**, 1198–1229 (2009).
[432]A. Goez and J. Neugebauer, in *Frontiers of Quantum Chemistry*, edited by M. J. Wójcik, H. Nakatsuji, B. Kirtman, and Y. Ozaki (Springer, Singapore, 2018), pp. 139–179.
[433]Q. Sun and G. K.-L. Chan, "Quantum embedding theories," Acc. Chem. Res. **49**, 2705–2712 (2016).
[434]J. M. Herbert, "Dielectric continuum methods for quantum chemistry," Wiley Interdiscip. Rev.: Comput. Mol. Sci. **11**, e1519 (2021).
[435]T. Giovannini, F. Egidi, and C. Cappelli, "Molecular spectroscopy of aqueous solutions: A theoretical perspective," Chem. Soc. Rev. **49**, 5664–5677 (2020).
[436]M. Swart, "AddRemove: A new link model for use in QM/MM studies," Int. J. Quantum Chem. **91**, 177–183 (2003).
[437]C. C. Pye, T. Ziegler, E. Van Lenthe, and J. N. Louwen, "An implementation of the conductor-like screening model of solvation within the Amsterdam density functional package—Part II. COSMO for real solvents," Can. J. Chem. **87**, 790–797 (2009).
[438]A. Klamt and G. Schüürmann, "COSMO: A new approach to dielectric screening in solvents with explicit expressions for the screening energy and its gradient," J. Chem. Soc., Perkin Trans. 2 **1993**, 799–805.
[439]C. A. Peeples and G. Schreckenbach, "Implementation of the SM12 solvation model into ADF and comparison with COSMO," J. Chem. Theory Comput. **12**, 4033–4041 (2016).
[440]A. V. Marenich, C. J. Cramer, and D. G. Truhlar, "Generalized Born solvation model SM12," J. Chem. Theory Comput. **9**, 609–620 (2013).
[441]A. V. Marenich, S. V. Jerome, C. J. Cramer, and D. G. Truhlar, "Charge model 5: An extension of hirshfeld population analysis for the accurate description of molecular interactions in gaseous and condensed phases," J. Chem. Theory Comput. **8**, 527–541 (2012).
[442]M. Swart and P. T. van Duijnen, "DRF90: A polarizable force field," Mol. Simul. **32**, 471–484 (2006).
[443]P. T. Van Duijnen, M. Swart, and L. Jensen, in *Solvation Effects on Molecules and Biomolecules: Computational Methods and Applications*, edited by S. Canuto (Springer, Netherlands, Dordrecht, 2008), pp. 39–102.
[444]L. Jensen, P. T. van Duijnen, and J. G. Snijders, "A discrete solvent reaction field model within density functional theory," J. Chem. Phys. **118**, 514–521 (2003).
[445]L. Jensen, P. T. van Duijnen, and J. G. Snijders, "A discrete solvent reaction field model for calculating molecular linear response properties in solution," J. Chem. Phys. **119**, 3800–3809 (2003).
[446]C. Cappelli, "Integrated QM/polarizable MM/continuum approaches to model chiroptical properties of strongly interacting solute–solvent systems," Int. J. Quantum Chem. **116**, 1532–1542 (2016).
[447]P. Lafiosca, S. Gómez, T. Giovannini, and C. Cappelli, "Absorption properties of large complex molecular systems: The DFTB/fluctuating charge approach," J. Chem. Theory Comput. **18**, 1765–1779 (2022).
[448]C. Sepali, S. Gómez, E. Grifoni, T. Giovannini, and C. Cappelli, "Computational spectroscopy of aqueous solutions: The underlying role of conformational sampling," J. Phys. Chem. B **128**, 5083–5091 (2024).
[449]T. Giovannini, F. Egidi, and C. Cappelli, "Theory and algorithms for chiroptical properties and spectroscopies of aqueous systems," Phys. Chem. Chem. Phys. **22**, 22864–22879 (2020).
[450]C. Sepali, P. Lafiosca, S. Gómez, T. Giovannini, and C. Cappelli, "Effective fully polarizable QM/MM approaches to compute Raman and Raman Optical Activity spectra in aqueous solution," Spectrochim. Acta, Part A **305**, 123485 (2024).
[451]P. Lafiosca, F. Rossi, F. Egidi, T. Giovannini, and C. Cappelli, "Multiscale frozen density embedding/molecular mechanics approach for simulating magnetic response properties of solvated systems," J. Chem. Theory Comput. **20**, 266–279 (2024).
[452]L. Nicoli, T. Giovannini, and C. Cappelli, "Assessing the quality of QM/MM approaches to describe vacuo-to-water solvatochromic shifts," J. Chem. Phys. **157**, 214101 (2022).
[453]C. Sepali, S. Skoko, L. Guglielmero, T. Giovannini, A. Mezzetta, F. D'Andrea, C. S. Pomelli, L. Guazzelli, and C. Cappelli, "Deciphering the structure of deep eutectic solvents: A computational study from the solute's viewpoint," J. Mol. Liq. **399**, 124326 (2024).
[454]Z. Hu and L. Jensen, "A discrete interaction model/quantum mechanical method for simulating plasmon-enhanced two-photon absorption," J. Chem. Theory Comput. **14**, 5896–5903 (2018).
[455]S. Gusarov, T. Ziegler, and A. Kovalenko, "Self-consistent combination of the three-dimensional RISM theory of molecular solvation with analytical gradients and the Amsterdam density functional package," J. Phys. Chem. A **110**, 6083–6090 (2006).
[456]T. A. Wesolowski, "Hydrogen-Bonding-Induced shifts of the excitation energies in nucleic acid bases: An interplay between electrostatic and electron density overlap effects," J. Am. Chem. Soc. **126**, 11444–11445 (2004).
[457]C. R. Jacob, J. Neugebauer, and L. Visscher, "A flexible implementation of frozen-density embedding for use in multilevel simulations," J. Comput. Chem. **29**, 1011–1018 (2008).
[458]T. A. Wesolowski and A. Warshel, "Frozen density functional approach for ab initio calculations of solvated molecules," J. Phys. Chem. **97**, 8050–8053 (1993).
[459]T. A. Wesolowski, S. Shedge, and X. Zhou, "Frozen-density embedding strategy for multilevel simulations of electronic structure," Chem. Rev. **115**, 5891–5928 (2015).
[460]C. R. Jacob and J. Neugebauer, "Subsystem density-functional theory," Wiley Interdiscip. Rev.: Comput. Mol. Sci. **4**, 325–362 (2014).
[461]C. R. Jacob and J. Neugebauer, "Subsystem density-functional theory (update)," Wiley Interdiscip. Rev.: Comput. Mol. Sci. **14**, e1700 (2024).
[462]D. Schlüns, K. Klahr, C. Mück-Lichtenfeld, L. Visscher, and J. Neugebauer, "Subsystem-DFT potential-energy curves for weakly interacting systems," Phys. Chem. Chem. Phys. **17**, 14323–14341 (2015).
[463]D. Schlüns, M. Franchini, A. W. Götz, J. Neugebauer, C. R. Jacob, and L. Visscher, "Analytical gradients for subsystem density functional theory within the slater-function-based amsterdam density functional program," J. Comp. Chem. **38**, 238–249 (2017).
[464]J. Neugebauer, M. J. Louwerse, E. J. Baerends, and T. A. Wesolowski, "The merits of the frozen-density embedding scheme to model solvatochromic shifts," J. Chem. Phys. **122**, 094115 (2005).
[465]J. Neugebauer, C. R. Jacob *et al.*, "An explicit quantum chemical method for modeling large solvation shells applied to aminocoumarin C151," J. Phys. Chem. A **109**, 7805–7814 (2005).
[466]J. Neugebauer and E. J. Baerends, "Exploring the ability of frozen-density embedding to model induced circular dichroism," J. Phys. Chem. A **110**, 8786–8796 (2006).
[467]J. Neugebauer, M. J. Louwerse, P. Belanzoni, T. A. Wesolowski, and E. J. Baerends, "Modeling solvent effects on electron-spin-resonance hyperfine couplings by frozen-density embedding," J. Chem. Phys. **123**, 114101 (2005).
[468]C. R. Jacob and L. Visscher, "Calculation of nuclear magnetic resonance shieldings using frozen-density embedding," J. Chem. Phys. **125**, 194104 (2006).
[469]R. E. Bulo, C. R. Jacob, and L. Visscher, "NMR solvent shifts of acetonitrile from frozen density embedding calculations," J. Phys. Chem. A **112**, 2640–2647 (2008).
[470]F. Egidi, S. Angelico, P. Lafiosca, T. Giovannini, and C. Cappelli, "A polarizable three-layer frozen density embedding/molecular mechanics approach," J. Chem. Phys. **154**, 164107 (2021).
[471]J. Neugebauer, "Couplings between electronic transitions in a subsystem formulation of time-dependent density functional theory," J. Chem. Phys. **126**, 134116 (2007).
[472]J. Neugebauer, "On the calculation of general response properties in subsystem density functional theory," J. Chem. Phys. **131**, 084104 (2009).
[473]J. Neugebauer, C. Curutchet, A. Muñoz-Losa, and B. Mennucci, "A subsystem TDDFT approach for solvent screening effects on excitation energy transfer couplings," J. Chem. Theory Comput. **6**, 1843–1851 (2010).
[474]C. König, N. Schlüter, and J. Neugebauer, "Direct determination of exciton couplings from subsystem time-dependent density-functional theory within the Tamm–Dancoff approximation," J. Chem. Phys. **138**, 034104 (2013).
[475]M. Pavanello and J. Neugebauer, "Modelling charge transfer reactions with the frozen density embedding formalism," J. Chem. Phys. **135**, 234103 (2011).

[476]M. Pavanello, T. Van Voorhis, L. Visscher, and J. Neugebauer, "An accurate and linear-scaling method for calculating charge-transfer excitation energies and diabatic couplings," J. Chem. Phys. **138**, 054101 (2013).
[477]D. G. Artiukhin and J. Neugebauer, "Frozen-density embedding as a quasi-diabatization tool: Charge-localized states for spin-density calculations," J. Chem. Phys. **148**, 214104 (2018).
[478]A. K. Rappé, C. J. Casewit, K. S. Colwell, W. A. Goddard III, and W. M. Skiff, "UFF, a full periodic table force field for molecular mechanics and molecular dynamics simulations," J. Am. Chem. Soc. **114**, 10024–10035 (1992).
[479]S. Spicher and S. Grimme, "Robust atomistic modeling of materials, organometallic, and biochemical systems," Angew. Chem., Int. Ed. **59**, 15665–15673 (2020).
[480]J. Wang, R. M. Wolf, J. W. Caldwell, P. A. Kollman, and D. A. Case, "Development and testing of a general AMBER force field," J. Comput. Chem. **25**, 1157–1174 (2004).
[481]O. Borodin, "Polarizable force field development and molecular dynamics simulations of ionic liquids," J. Phys. Chem. B **113**, 11463–11478 (2009).
[482]W. D. Cornell, P. Cieplak, C. I. Bayly, I. R. Gould, K. M. Merz, D. M. Ferguson, D. C. Spellmeyer, T. Fox, J. W. Caldwell, and P. A. Kollman, "A second generation force field for the simulation of proteins, nucleic acids, and organic molecules," J. Am. Chem. Soc. **117**, 5179–5197 (1995).
[483]M. Clark, R. D. Cramer III, and N. van Opdenbosch, "Validation of the general purpose tripos 5.2 force field," J. Comput. Chem. **10**, 982–1012 (1989).
[484]A. P. Thompson, H. M. Aktulga, R. Berger, D. S. Bolintineanu, W. M. Brown, P. S. Crozier, P. J. in 't Veld, A. Kohlmeyer, S. G. Moore, T. D. Nguyen, R. Shan, M. J. Stevens, J. Tranchida, C. Trott, and S. J. Plimpton, "LAMMPS—A flexible simulation tool for particle-based materials modeling at the atomic, meso, and continuum scales," Comput. Phys. Commun. **271**, 108171 (2022).
[485]B. R. Brooks *et al.*, "CHARMM: The biomolecular simulation program," J. Comput. Chem. **30**, 1545–1614 (2009).
[486]J. C. Phillips, R. Braun, W. Wang, J. Gumbart, E. Tajkhorshid, E. Villa, C. Chipot, R. D. Skeel, L. Kalé, and K. Schulten, "Scalable molecular dynamics with NAMD," J. Comput. Chem. **26**, 1781–1802 (2005).
[487]M. J. Abraham, T. Murtola, R. Schulz, S. Páll, J. C. Smith, B. Hess, and E. Lindahl, "GROMACS: High performance molecular simulations through multi-level parallelism from laptops to supercomputers," SoftwareX **1-2**, 19–25 (2015).
[488]J. Wang, W. Wang, P. A. Kollman, and D. A. Case, "Automatic atom type and bond type perception in molecular mechanical calculations," J. Mol. Graphics Modell. **25**, 247–260 (2006).
[489]M. Swart, pdb2adf Documentation, https://www.scm.com/doc/Hybrid/pdb2adf/pdb2adf.html.
[490]A. C. T. van Duin, S. Dasgupta, F. Lorant, and W. A. Goddard, "ReaxFF: A reactive force field for hydrocarbons," J. Phys. Chem. A **105**, 9396–9409 (2001).
[491]T. P. Senftle, S. Hong, M. M. Islam, S. B. Kylasa, Y. Zheng, Y. K. Shin, C. Junkermeier, R. Engel-Herbert, M. J. Janik, H. M. Aktulga, T. Verstraelen, A. Grama, and A. C. T. van Duin, "The ReaxFF reactive force-field: Development, applications and future directions," npj Comput. Mater. **2**, 15011 (2016).
[492]J. Tersoff, "Empirical interatomic potential for carbon, with applications to amorphous carbon," Phys. Rev. Lett. **61**, 2879–2882 (1988).
[493]D. W. Brenner, "Empirical potential for hydrocarbons for use in simulating the chemical vapor deposition of diamond films," Phys. Rev. B **42**, 9458–9471 (1990).
[494]S. J. Plimpton and A. P. Thompson, "Computational aspects of many-body potentials," MRS Bull. **37**, 513–521 (2012).
[495]N. Nayir, Q. Mao, T. Wang, M. Kowalik, Y. Zhang, M. Wang, S. Dwivedi, G.-U. Jeong, Y. K. Shin, and A. van Duin, "Modeling and simulations for 2D materials: A ReaxFF perspective," 2D Mater. **10**, 032002 (2023).
[496]W. J. Mortier, S. K. Ghosh, and S. Shankar, "Electronegativity-equalization method for the calculation of atomic charges in molecules," J. Am. Chem. Soc. **108**, 4315–4320 (1986).
[497]T. Verstraelen, P. W. Ayers, V. Van Speybroeck, and M. Waroquier, "ACKS2: Atom-condensed Kohn–Sham DFT approximated to second order," J. Chem. Phys. **138**, 074108 (2013).
[498]M. M. Islam, G. Kolesov, T. Verstraelen, E. Kaxiras, and A. C. T. van Duin, "eReaxFF: A pseudoclassical treatment of explicit electrons within reactive force field simulations," J. Chem. Theory Comput. **12**, 3463–3472 (2016).
[499]I. Leven, H. Hao, S. Tan, X. Guan, K. A. Penrod, D. Akbarian, B. Evangelisti, M. J. Hossain, M. M. Islam, J. P. Koski, S. Moore, H. M. Aktulga, A. C. T. van Duin, and T. Head-Gordon, "Recent advances for improving the accuracy, transferability, and efficiency of reactive force fields," J. Chem. Theory Comput. **17**, 3237–3251 (2021).
[500]M. J. Hossain, G. Pawar, and A. C. T. van Duin, "Development and applications of an eReaxFF force field for graphitic anodes of lithium-ion batteries," J. Electrochem. Soc. **169**, 110540 (2022).
[501]J. S. Smith, B. Nebgen, N. Lubbers, O. Isayev, and A. E. Roitberg, "Less is more: Sampling chemical space with active learning," J. Chem. Phys. **148**, 241733 (2018).
[502]J. S. Smith, B. T. Nebgen, R. Zubatyuk, N. Lubbers, C. Devereux, K. Barros, S. Tretiak, O. Isayev, and A. E. Roitberg, "Approaching coupled cluster accuracy with a general-purpose neural network potential through transfer learning," Nat. Commun. **10**, 2903 (2019).
[503]C. Devereux, J. S. Smith, K. K. Huddleston, K. Barros, R. Zubatyuk, O. Isayev, and A. E. Roitberg, "Extending the applicability of the ANI deep learning molecular potential to sulfur and halogens," J. Chem. Theory Comput. **16**, 4192–4202 (2020).
[504]J. Behler and M. Parrinello, "Generalized neural-network representation of high-dimensional potential-energy surfaces," Phys. Rev. Lett. **98**, 146401 (2007).
[505]D. Anstine, R. Zubatyuk, and O. Isayev, "AIMNet2: A neural network potential to meet your neutral, charged, organic, and elemental-organic needs," chemRxiv:10.26434/chemrxiv-2023-296ch-v3 (2024).
[506]C. Chen and S. P. Ong, "A universal graph deep learning interatomic potential for the periodic table," Nat. Comput. Sci. **2**, 718–728 (2022).
[507]A. H. Larsen *et al.*, "The atomic simulation environment—A Python library for working with atoms," J. Phys.: Condens. Matter **29**, 273002 (2017).
[508]B. Deng, P. Zhong, K. Jun, J. Riebesell, K. Han, C. J. Bartel, and G. Ceder, "CHGNet as a pretrained universal neural network potential for charge-informed atomistic modelling," Nat. Mach. Intell. **5**, 1031–1041 (2023).
[509]I. Batatia, D. P. Kovacs, G. Simm, C. Ortner, and G. Csányi, "MACE: Higher order equivariant message passing neural networks for fast and accurate force fields," in *Advances in Neural Information Processing Systems 35* (Curran Associates, Inc., 2022), pp. 11423–11436.
[510]H. Yang *et al.*, "MatterSim: A deep learning atomistic model across elements, temperatures and pressures," arXiv:2405.04967 (2024).
[511]A. Kabylda, J. T. Frank, S. S. Dou, A. Khabibrakhmanov, L. M. Sandonas, O. T. Unke *et al.*, "Molecular simulations with a pretrained neural network and universal pairwise force fields," chemRxiv:10.26434/chemrxiv-2024-bdfr0-v2 (2025).
[512]S. Batzner, A. Musaelian, L. Sun, M. Geiger, J. P. Mailoa, M. Kornbluth, N. Molinari, T. E. Smidt, and B. Kozinsky, "E(3)-equivariant graph neural networks for data-efficient and accurate interatomic potentials," Nat. Commun. **13**, 2453 (2022).
[513]Y. Shao, M. Hellström, P. D. Mitev, L. Knijff, and C. Zhang, "PiNN: A Python library for building atomic neural networks of molecules and materials," J. Chem. Inf. Model. **60**, 1184–1193 (2020).
[514]K. T. Schütt, S. S. P. Hessmann, N. W. A. Gebauer, J. Lederer, and M. Gastegger, "SchNetPack 2.0: A neural network toolbox for atomistic machine learning," J. Chem. Phys. **158**, 144801 (2023).
[515]S. Chmiela, H. E. Sauceda, I. Poltavsky, K.-R. Müller, and A. Tkatchenko, "sGDML: Constructing accurate and data efficient molecular force fields using machine learning," Comput. Phys. Commun. **240**, 38–45 (2019).
[516]H. Wang, L. Zhang, J. Han, and E. Weinan, "DeePMD-kit: A deep learning package for many-body potential energy representation and molecular dynamics," Comput. Phys. Commun. **228**, 178–184 (2018).
[517]L.-P. Wang, A. Titov, R. McGibbon, F. Liu, V. S. Pande, and T. J. Martínez, "Discovering chemistry with an *ab initio* nanoreactor," Nat. Chem. **6**, 1044–1048 (2014).
[518]M. J. Mees, G. Pourtois, E. C. Neyts, B. J. Thijsse, and A. Stesmans, "Uniform-acceptance force-bias Monte Carlo method with time scale to study solid-state diffusion," Phys. Rev. B **85**, 134301 (2012).
[519]K. M. Bal and E. C. Neyts, "Direct observation of realistic-temperature fuel combustion mechanisms in atomistic simulations," Chem. Sci. **7**, 5280–5286 (2016).
[520]SCM ChemTraYzer2 Documentation, https://www.scm.com/doc/AMS/Utilities/ChemTraYzer2.html.

[521]L. C. Kröger, W. A. Kopp, M. Döntgen, and K. Leonhard, "Assessing statistical uncertainties of rare events in reactive molecular dynamics simulations," J. Chem. Theory Comput. **13**, 3955–3960 (2017).
[522]Y. Kim, J. W. Kim, Z. Kim, and W. Y. Kim, "Efficient prediction of reaction paths through molecular graph and reaction network analysis," Chem. Sci. **9**, 825–835 (2018).
[523]A. Pedersen, S. F. Hafstein, and H. Jónsson, "Efficient sampling of saddle points with the minimum-mode following method," SIAM J. Sci. Comput. **33**, 633–652 (2011).
[524]S. T. Chill, M. Welborn, R. Terrell, L. Zhang, J.-C. Berthet, A. Pedersen, H. Jónsson, and G. Henkelman, "EON: Software for long time simulations of atomic scale systems," Modell. Simul. Mater. Sci. Eng. **22**, 055002 (2014).
[525]I. A. W. Filot, R. A. van Santen, and E. J. M. Hensen, "The optimally performing Fischer–Tropsch catalyst," Angew. Chem., Int. Ed. **53**, 12746–12750 (2014).
[526]M. Stamatakis and D. G. Vlachos, "A graph-theoretical kinetic Monte Carlo framework for on-lattice chemical kinetics," J. Chem. Phys. **134**, 214115 (2011).
[527]J. Nielsen, M. d'Avezac, J. Hetherington, and M. Stamatakis, "Parallel kinetic Monte Carlo simulation framework incorporating accurate models of adsorbate lateral interactions," J. Chem. Phys. **139**, 224706 (2013).
[528]H. van Eersel, P. A. Bobbert, R. A. J. Janssen, and R. Coehoorn, "Monte Carlo study of efficiency roll-off of phosphorescent organic light-emitting diodes: Evidence for dominant role of triplet-polaron quenching," Appl. Phys. Lett. **105**, 143303 (2014).
[529]R. Coehoorn, H. van Eersel, P. Bobbert, and R. Janssen, "Kinetic Monte Carlo study of the sensitivity of OLED efficiency and lifetime to materials parameters," Adv. Funct. Mater. **25**, 2024–2037 (2015).
[530]S. Gottardi, M. Barbry, R. Coehoorn, and H. van Eersel, "Efficiency loss processes in hyperfluorescent OLEDs: A kinetic Monte Carlo study," Appl. Phys. Lett. **114**, 073301 (2019).
[531]A. Fredenslund, R. L. Jones, and J. M. Prausnitz, "Group-contribution estimation of activity coefficients in nonideal liquid mixtures," AIChE J. **21**, 1086–1099 (1975).
[532]A. Klamt, "Conductor-like screening model for real solvents: A new approach to the quantitative calculation of solvation phenomena," J. Phys. Chem. **99**, 2224–2235 (1995).
[533]S.-T. Lin and S. I. Sandler, "A priori phase equilibrium prediction from a segment contribution solvation model," Ind. Eng. Chem. Res. **41**, 899–913 (2002).
[534]D. S. Desmond, D. Saltymakova, O. Crabeck, G. Schreckenbach, J. D. Xidos, D. G. Barber, D. Isleifson, and G. A. Stern, "Methods for interpreting the partitioning and fate of petroleum hydrocarbons in a sea ice environment," J. Phys. Chem. A **126**, 772–786 (2022).
[535]A. Klamt, *COSMO-RS: From Quantum Chemistry to Fluid Phase Thermodynamics and Drug Design* (Elsevier, 2005).
[536]R. Xiong, S. I. Sandler, and R. I. Burnett, "An improvement to COSMO-SAC for predicting thermodynamic properties," Ind. Eng. Chem. Res. **53**, 8265–8278 (2014).
[537]W.-L. Chen and S.-T. Lin, "Explicit consideration of spatial hydrogen bonding direction for activity coefficient prediction based on implicit solvation calculations," Phys. Chem. Chem. Phys. **19**, 20367–20376 (2017).
[538]M. Diedenhofen and A. Klamt, "COSMO-RS as a tool for property prediction of IL mixtures—A review," Fluid Phase Equilib. **294**, 31–38 (2010).
[539]H. S. Elbro, A. Fredenslund, and P. Rasmussen, "A new simple equation for the prediction of solvent activities in polymer solutions," Macromolecules **23**, 4707–4714 (1990).
[540]K. S. Pitzer and J. M. Simonson, "Thermodynamics of multicomponent, miscible, ionic systems: Theory and equations," J. Phys. Chem. **90**, 3005–3009 (1986).
[541]N. D. Austin, N. V. Sahinidis, I. A. Konstantinov, and D. W. Trahan, "COSMO-based computer-aided molecular/mixture design: A focus on reaction solvents," AIChE J. **64**, 104–122 (2018).
[542]L. Komissarov, R. Rüger, M. Hellström, and T. Verstraelen, "ParAMS: Parameter optimization for atomistic and molecular simulations," J. Chem. Inf. Model. **61**, 3737 (2021).
[543]M. Pols, A. C. T. van Duin, S. Calero, and S. Tao, "Mixing I and Br in inorganic perovskites: Atomistic insights from reactive molecular dynamics simulations," J. Phys. Chem. C **128**, 4111–4118 (2024).
[544]L. Komissarov and T. Verstraelen, "Improving the silicon interactions of GFN-xTB," J. Chem. Inf. Model. **61**, 5931–5937 (2021).
[545]M. Freitas Gustavo and T. Verstraelen, "GloMPO (globally managed parallel optimization): A tool for expensive, black-box optimizations, application to ReaxFF reparameterizations," J. Cheminform. **14**, 7 (2022).
[546]M. Freitas Gustavo *et al.*, "Sensitivity analysis for ReaxFF reparametrization using the Hilbert–Schmidt independence criterion," J. Chem. Theory Comput. **19**, 2557–2573 (2023).
[547]A. M. Miksch, T. Morawietz, J. Kästner, A. Urban, and N. Artrith, "Strategies for the construction of machine-learning potentials for accurate and efficient atomic-scale simulations," Mach. Learn.: Sci. Technol. **2**, 031001 (2021).
[548]M. Kulichenko, B. Nebgen, N. Lubbers, J. S. Smith, K. Barros, A. E. A. Allen, A. Habib, E. Shinkle, N. Fedik, Y. W. Li, R. A. Messerly, and S. Tretiak, "Data generation for machine learning interatomic potentials and beyond," Chem. Rev. **124**, 13681–13714 (2024).
[549]D. Wu, "Pool-based sequential active learning for regression," IEEE Trans. Neural Networks Learn. Syst. **30**, 1348–1359 (2019).
[550]J. T. Margraf, "Science-driven atomistic machine learning," Angew. Chem., Int. Ed. **62**, e202219170 (2023).
[551]W. Zhang and A. C. T. van Duin, "Second-generation ReaxFF water force field: Improvements in the description of water density and OH-anion diffusion," J. Phys. Chem. B **121**, 6021–6032 (2017).
[552]C. R. Jacob, S. M. Beyhan, R. E. Bulo, A. S. P. Gomes, A. W. Götz, K. Kiewisch, J. Sikkema, and L. Visscher, "PyADF—A scripting framework for multiscale quantum chemistry," J. Comput. Chem. **32**, 2328–2338 (2011).
[553]F. Zapata, L. Ridder, J. Hidding, C. R. Jacob, I. Infante, and L. Visscher, "QMflows: A tool kit for interoperable parallel workflows in quantum chemistry," J. Chem. Inf. Model. **59**, 3191–3197 (2019).